Kseniia Sysoliatina

THE STRUCTURE AND KINEMATICS OF THE MILKY WAY DISK IN VIEW OF A SEMI-ANALYTIC CHEMO-DYNAMIC MODEL

Heidelberg
2018

Cover picture: The night-time sky over southern Australia, photo by Christian Sasse (2017)

Dissertation

submitted to the

Combined Faculties for the Natural Sciences and for Mathematics

of the Ruperto-Carola University of Heidelberg, Germany

for the degree of

Doctor of Natural Sciences

presented by

Kseniia Sysoliatina

born in: Sudak, Ukraine

Oral examination: 21st November 2018

THE STRUCTURE AND KINEMATICS OF THE MILKY WAY DISK
IN VIEW OF A SEMI-ANALYTIC CHEMO-DYNAMIC MODEL

Referees: apl. Prof. Dr. Andreas Just
Prof. Dr. Norbert Christlieb

ZUSAMMENFASSUNG: DIE STRUKTUR UND KINEMATIK DER MILCHSTRAßEN-SCHEIBE IM HINBLICK AUF EIN SEMI-ANALYTISCHES CHEMO-DYNAMISCHES MODELL

In dieser Arbeit untersuchen wir die räumliche Struktur sowie die chemischen und kinematischen Eigenschaften der Milchstraße auf der Grundlage eines semi-analytischen chemo-dynamischen Modells von Just and Jahreiß (2010) (JJ Modell). Unter der Annahme, dass sich die Scheibe von innen nach außen gebildet hat und eine konstante Dicke aufweist, erweitern wir das lokale JJ Modell auf galaktozentrische Entfernungen von R = 4 – 12 kpc. Für jeden Radius nehmen wir eine Sternentstehungsrate (SFR), deren Maximum in der äußeren Scheibe in Richtung jüngerer Alter verschoben ist, und nutzen die anfängliche Massenfunktion (IMF) in Form des Potenzgesetzes mit vier Steigungen (Rybizki and Just, 2015). Die Alter-Geschwindigkeitsdispersion- und Alter-Metallizitätsrelation (AVR und AMR) werden dann selbstkonsistent berechnet; letztere wird mit Metallizitätsverteilungen der Roten Klumpen-Sterne aus dem Apache Point Observatory Galactic Evolution Experiment (APOGEE, Eisenstein et al., 2011) eingeschränkt.

Im Rahmen der Vorwärtsmodellierung validieren wir das lokale JJ Modell im Solarzylinder, indem wir es mithilfe der Proben aus dem Radial Velocity Experiment (RAVE, Steinmetz et al., 2006) und der ersten und zweiten Gaia-Datenveröffentlichung (DR1 und DR2, Lindegren et al., 2016; Gaia Collaboration et al., 2018) gegenprüfen. Wir finden eine Gesamtabweichung in der Anzahl an Sternen von bis zu $\sim 9\%$, mit einer statistisch signifikanten Diskrepanz für die dynamisch kalten Populationen.

Wir entwickeln außerdem ein neues Verfahren für den asymmetrischen Drift und wenden sie in drei Metallizitätsbins auf die lokale RAVE-Probe und G-Zwerge aus der Sloan Extension for Galactic Understanding and Exploration (SEGUE, Yanny et al., 2009) an. Die tangentiale Komponente der solaren Eigengeschwindigkeit, die mit der RAVE-Probe berechnet wird, ist $V_\odot = 4.47 \pm 0.8$ km s^{-1}. Die aus den SEGUE G-Zwergen rekonstruierte Rotationskurve in Entfernungen von R = 7 – 10 kpc hat eine Steigung von nahezu Null und beträgt 0.033 ± 0.034. Die zur dicken Scheibe gehörenden G-Zwerge sind kinematisch homogen mit einer Skalenlänge von 2.05 ± 0.22 kpc, was mit Literaturwerten übereinstimmt.

ABSTRACT: THE STRUCTURE AND KINEMATICS OF THE MILKY WAY DISK IN VIEW OF A SEMI-ANALYTIC CHEMO-DYNAMIC MODEL

In this work we study the spatial structure as well as the chemical and kinematic properties of the Milky Way disk on the basis of a semi-analytic chemo-dynamical model from Just and Jahreiß (2010) (JJ model).

Assuming inside-out formation and a constant thickness of the MW disk, we generalise the local JJ model to Galactocentric distances of R = 4 – 12 kpc. At each radius we assume a star formation rate (SFR) with a peak shifting to younger ages for the outer disk and use the four-slope broken power-law initial mass function (IMF) from Rybizki and Just (2015). The age-velocity dispersion and age-metallicity relations (AVR and AMR) are then obtained self-consistently; the latter is constrained by metallicity distributions of the Red Clump stars from the Apache Point Observatory Galactic Evolution Experiment (APOGEE, Eisenstein et al., 2011).

Within a forward modelling framework, we validate the local JJ model in the solar cylinder by testing it against the samples from the Radial Velocity Experiment (RAVE, Steinmetz et al., 2006) and the first and second Gaia data releases (DR1 and DR2, Lindegren et al., 2016; Gaia

Collaboration et al., 2018). We find an overall mismatch in star counts up to $\sim 9\%$, with a statistically significant discrepancy identified for the dynamically cold populations.

We also develop a new treatment of the asymmetric drift and apply it in three metallicity bins to the RAVE local sample and G-dwarfs from the Sloan Extension for Galactic Understanding and Exploration (SEGUE, Yanny et al., 2009). The tangential component of the solar peculiar motion obtained from the RAVE sample is $V_{\odot} = 4.47 \pm 0.8$ km s^{-1}. The rotation curve reconstructed from the SEGUE G-dwarfs in a range of distances R = 7 – 10 kpc has a near-zero slope of 0.033 ± 0.034. The thick disk G-dwarfs are found to be kinematically homogeneous with a scale length of 2.05 ± 0.22 kpc, which is in agreement with values from the literature.

Contents

List of Figures

List of Tables

Acknowledgements

First of all, I would like to acknowledge the International Max Planck Research School for Astronomy and Cosmic Physics at the University of Heidelberg (IMPRS-HD): this program gave me the support in the search for my PhD position in Germany. I thank my host institute Astronomisches Rechen-Institut (ARI) for providing me with all the requisites required to conduct a good research, and also express my gratitude to the Collaborative Research Center (Sonderforschungsbereich, SFB) 881 "The Milky Way System" at the Heidelberg University for funding my research project.

I would like to acknowledge my supervisor Prof. Dr. Andreas Just. Our regular discussions contributed significantly to my understanding of the field, and his cordiality used to encourage me to continue investigations even of the seemingly confusing questions. And even more importantly, the high level of freedom I was given during my work helped me to develop skills to become an independent researcher at an early stage of my career.

I also thank all my family members who, from the very beginning, supported me wholeheartedly in my intention to enter the scientific community. I highly appreciate the help of my friend Veronika Mitrokhina who always showed a true interest in my scientific development as well as in my emotional state. I thank my friend and former office mate Daniel Haydon who's sociability helped me to adapt quickly to the new environment and with whom I later spent many pleasant weekends.

A significant part of this work has been done in collaboration with my former teacher and now colleague Alex Golubov. Working with him was a real pleasure, I owe him my first experience of being a part of a high-motivated and tireless team. I also thank Prof. Dr. Eva K. Grebel: as a co-author of the two papers which formed the basis two chapters of this thesis she gave me a valuable feedback on several scientific questions. Another former teacher, Dr. Elena Bannikova, has been sharing with me her enthusiasm and optimism, so I want to say many thanks for the support from a more experienced researcher.

I thank the former students of our group, Jan Rybizki, Ioanna Koutsouridou, and Tina Gier, who's results were useful for my study. Working in an active collaboration with Ioanna for about a year was always a fun, and this also motivated me to struggle for a deeper understanding of the field. I also appreciate the help of Matteo Mazzarini who gave me a good overview of the modern numerical tools of galactic astronomy.

I express my deep gratitude to Alex Razim - for all her patience and belief in me, for our interesting discussions on astronomy and biology and, above all, for the warm-heartedness she has been sharing with me for all these years.

Finally, I thank Daniel Haydon, Alex Razim, Katja Reichert and Fabian Klein for reading parts of this thesis and giving comments on my writing style and the scientific content of the work.

Chapter 1

Introduction

1.1 Prologue

The origins of astronomy go back to very ancient ages, and there are several reasons why this field of knowledge has appeared so early. The first factor is rather straightforward: revealing regularities in the motion of celestial bodies served directly to economic and political needs of the early societies. A calendar seems to be an essential component of sedentary life, and that is confirmed by an immense number of examples from the ancient Egypt and Babylon to any modern country. Knowledge of the saros cycle provided the ancient priests a dominance over their peoples, who did not understand the true nature of the solar and lunar eclipses. But, of course, it is much more than just periodic motion patterns what people may wish to learn from the starry darkness sprawling overhead every clear night.

Curiosity is one of the distinctive features of primates to which our biological species *Homo sapiens* relates. For millions of years the human mind has been polishing its skills to solve problems of the different complexity level. However, the ability to overcome difficulties is not yet enough for the survival of the species. The principle of the natural selection strongly favours individuals with a talent to query the world in order to *foresee* the problems, not just deal with their destructive consequences. In other words, curiosity - a quality to ask questions - and creativity - a quality to find good and novel answers - have been and still remain the necessary components of our success. This leads us to the second main factor which has influenced the development of astronomy: a strong desire to understand the essence of the natural world. One may also wonder about the underlying reasons of this desire, and this is a reformulated question about human nature. It is sometimes said that people possess a natural sense of beauty, and therefore the exploration of stars is driven by the aesthetic awareness. A complementary, but much less poetic, explanation involves a basic psychological need to control the surrounding environment in order to assure someone's own safety. The latter might be achieved through a learning process, as nothing scares more than the unknown. And yet the beauty of the night sky might have been a far stronger motivation than the anxiety about its mysteries: one only needs to recall a magnificent view of glimmering constellations with a band of the Milky Way crossing the sky like a strip of scattered sugar...

Another important question worth mentioning here concerns the human way of thinking. Evolution made us curious and creative, but we have not deluded ourselves with believing that these qualities are flawless. The same mechanisms which enhanced human eagerness to ask and

answer questions have simultaneously been constraining it. And the reason is simple: it might be dangerous to raise *too many* questions, especially if you are not skilled enough to resolve them properly. Our world is complicated, the wild nature we all came from is a system with a tremendous number of parameters, and very often it is difficult or impossible to disentangle causes and effects without deep knowledge in the field. That's why evolution also taught us to be cautious and take complicated phenomena as a whole, because mistakes in this case might cost one his life. And this helps to understand why people had to go such a long way from the odd and abstract ideas mixed with myths and brilliant guesses to complicated and verified theories developed in a framework of scientific method. Being rational, exploring a wide range of hypotheses, performing experiments and making conclusions based on the results - all of this is *not* our natural behaviour, but this is what we have had to learn by ourselves.

Eventually, the very principles of questioning the world about its structure have changed over centuries: to be a philosopher in the ancient Greece, a mere assertion of a kind "everything is fire" was enough, while the modern science requires much more efforts from those who want to explore the nature. And even with all the rationality and skepticism, it is easy to make a mistake and choose a wrong way, such that the modern science is not free of such flaws as reproducibility crisis, false positive results, confirmation and publication biases.

In this light, the progress people have done in astronomy since Galelio's first use of the telescope is really encouraging. It might already be difficult to imagine that less than a hundred years ago the relation of the Milky Way to the numerous small nebular objects was yet unclear and according to the common point of view we lived in a vast stellar system in the center of the static infinite Universe.

Study of the Galaxy is, in many respects, a fascinating and exciting work. Countless galaxies fill the space, and though some dreamers believe in remarkable power and ingenuity of the human intelligence which would allow us to reach other stars and even galactic systems, the modern science gives us no sign that we would ever be able to investigate any other galaxy in such details as we can do for the Milky Way. The Galaxy is our laboratory, and though we are not allowed to carry out experiments on our own, we still have an opportunity to collect information of a great value for understanding the morphology, formation and evolution of other galaxies.

This work is a small contribution to the field of galactic astronomy. But just as galaxies consist of a huge number of individual stars, the full understanding of a phenomenon usually originates from the solutions of many simplified problems.

1.2 Historical overview[1]

> "WASHINGTON, Nov. 22, 1924 – Confirmation of the view that the spiral nebulae, which appear in the heavens as whirling clouds, are in reality distant stellar systems, or 'island universes', has been obtained by Dr. Edwin Hubbell of the Carnegie Institution's Mount Wilson observatory, through investigations carried out with the observatory's powerful telescopes." *The New York Times*

The title "Finds Spiral Nebulae Are Stellar Systems: Dr. Hubbell Confirms View That They Are 'Island Universes' Similar to Our Own" might have caught attention of many interested Americans on that day (though, it is very plausible that in reality this note was overshad-

[1] During writing of this Section materials from Whitney (1988) and Berendzen and Hoskin (1971) were used.

owed by more pragmatic topics about economic problems, political news and events from the private life of prominent people). Whatever impact was of this article on public, the announcement of Edwin Hubble (1889 – 1953) officially ended a hot scientific debate of the early 20th century. His presentation of the work in the American Astronomical Society evoked a wide response in astronomical community. Indeed, this was a milestone in the history of galactic astronomy and cosmology: the true picture of our Universe and the place of the Milky Way in it finally started to shape up after about two centuries of dedicated observations.

* * *

At the dawn of civilization the night sky was a far more magnificent spectacle than it appears now to modern man. Thus, there is nothing surprising by the fact that the Milky Way in particular drew the attention of the ancient people and was poetically described in the old myths and legends. The other objects of the same class visible to naked eye are the Andromeda Nebula and the Magellanic Clouds, which were also known to the ancient cultures. But the main problem of studying them in the pre-telescope epoch consisted of the lack of information, as a human eye is not capable of resolving the glow of the nebulae into separate stars. This explains why the early speculations about the nature of the Galaxy, though they included many correct guesses revealing the intuition of philosophers, often led in wrong directions: one cannot understand galaxies without knowing their structure as well as physical laws which govern their evolution.

Starting from the 16th century, after Galileo Galilei (1564 – 1642) used a telescope to reveal the mysteries of the sky for the first time, it was clear that the Milky Way is a huge conglomerate of stars. Galilei also observed a number of small nebular objects and assumed that they consist of stars as well, however with the optical resolution at that time this statement remained a mere speculation.

At the same time another chain of events was preparing the ground for establishing the physical law of interaction between massive bodies. Johannes Kepler (1571 – 1630) collaborated with the Dutch astronomer Tycho Brahe (1546 – 1601) who observed the motions of planets for more then 20 years. After the death of the latter, Kepler inherited and made use of Brahe's data. He derived three elegant empirical laws of planetary motions and suggested that motion of planets along the orbits has something to do with the Sun's rotation. Galileo took another step forward and suggested gravity to be a universal force governing the motion of celestial bodies. Robert Hooke (1635 – 1703) had already written about the inverse proportionality between gravitational force and distance when Isaak Newton (1642 – 1727) published his *Principia Mathematica* in 1687 and established the inverse square law. Starting from this point, the way to understanding nebulae and the Milky Way was charted.

Then the actual study of the Milky Way began: the most prominent minds of the epoch hypothesised about the possible origin scenarios and the present-day structure of the Galaxy. Thomas Wright (1711 – 1786) surmised that the Milky Way has a three-dimensional form of the ring-shaped disk. The line of thought was developed by Immanuel Kant (1724 – 1804) who described the Milky Way as a self-gravitating rotating stellar disk. Almost at the same time Pierre Simon de Laplace (1749 – 1827) proposed a model of planetary systems formation from rotating clouds of gas. This evoked a temptation to draw a parallel between Kant and Laplace ideas and to conclude that we live in a huge flattened stellar system with the small nebulae observed here and there on the sky being gaseous clouds involved in the process of planetary

formation. Thus, in the second part of 18^{th} century two alternative hypothesis came out of all the earlier speculations:

- Kant-Laplacian: Milky Way is the only system of this kind in the Universe; nebulae belong to the Milky Way.
- Wright-Kantian: Milky Way is one of many 'stellar islands' populating the Universe; nebulae are other distant galaxies.

Small nebula patches did not seem too interesting to astronomers at that time. Hunting comets was much more popular, but with the resolutions available both comets and nebula objects looked vaguely the same, and only registering the proper motion could help to distinguish them. Perhaps, more than one astronomer was disappointed to know that yet another candidate for a comet turned out to be some odd nebula. Motivated by a desire to save time in his comet hunting, Charles Messier (1730 – 1817) listed 110 nebulae and published the catalogue in 1774. It contained a variety of objects: open and globular clusters, distant galaxies, planetary and emission nebulae. There is no wonder that astronomers were later confronted with a series of confusions and contradictions as they tried to make a choice between Kant-Laplacian and Wright-Kantian hypothesis with such different objects united under the same term of 'nebula'.

A breakthrough in the galactic astronomy was made by William Herschel (1738 – 1822) who undertook the first systematic survey of the stellar content of the Milky Way and attempted to reconstruct the shape of the Galaxy. He derived distances from the apparent magnitudes (it was the best he could do at the time; the first successful parallax measurements were yet to happen). As a result, the first Milky Way map was drastically distorted and it was still difficult to decide which hypothesis, Wright-Kantian or Kant-Laplacian, was better.

During the following decades several misinterpreted and also false discoveries were persuading the astronomical community to favour the Kant-Laplacian model. With a spectroscopic study of the light from the planetary nebulae in Draco, William Huggins (1824 – 1910) discovered that it consists of hot gas, but not stars. This news strengthened the Kant-Laplacian point of view according to which nebulae are gaseous swirls undergoing planetary formation phase. The second argument came from Harlow Shapley (1885 – 1972) who derived distances to the globular clusters and noticed that their distribution has a spherical geometry. With the Galactic center defined, an estimate of the Galaxy diameter, which was calculated with the distances measured with the eclipsing binaries method, was found to be 300, 000 light years. This left no room for doubts that gaseous nebulae belong to our Galaxy. As to those nebulae which demonstrated the stellar-like spectra, the existence of the systems located outside such an unimaginably distant edge of the Galaxy seemed absolutely ridiculous. Another strong support came from measurements of Adriaan van Maanen (1884 – 1946) who compared photographic plates of spiral nebulae and claimed to detect their rotational motion implying their closeness. Eventually, the fourth reassurance concerned nova star in the Andromeda Nebulae detected on 17^{th} August 1885. Under the assumption that Andromeda is an external stellar system similar to the Milky Way, it seemed impossible to imagine a star with the brightness comparable to the huge galactic system.

In other words, it was extremely difficult to comprehend the spatial scales of the Universe and its stellar systems, as well as the power of stellar explosions. Heber Curtis (1872 – 1942) was one of those who disagreed with Sharpley's picture taking his distances to be overestimated; thus, Curtis assumed the Milky Way to be much smaller with the nebular objects located outside the Galaxy. The culmination came on the 26^{th} of April 1920, when the so-called Great

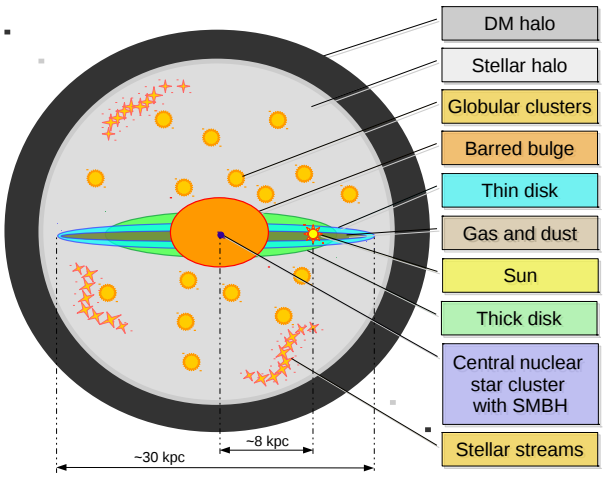

Figure 1.1: Schematic view of the Milky Way. The flattened component consists of the thin and thick disks with the layers of gas and dust also confined to the Galactic plane. The innermost region is occupied by the thicker bulge with the bar and the supermassive black hole (SMBH) sitting in the Galactic center (GC). The Galactic disks and bulge are embedded into the spherical halo consisting of dark matter (DM) and old stars. To the Milky Way halo also belong such substructures as globular clusters and stellar streams from the accreted satellite galaxies.

Debate took place in the Smithsonian Museum of Natural History in Washington. The Debate itself did not give a final answer to the main astronomical question of that time, but shortly after the answers started to come from different and numerous sources. Edwin Hubble discovered variable stars in Andromeda and calculated its distance, that dispelled any doubts as to extragalactic nature of nebulae. Measurements of van Maanen were proved to be incorrect (the phantom shifts of spiral nebula features came from different optical distortions on the image edges). Understanding of the inner structure of stars was improved, and it was realised that the bright star in the Andromeda galaxy was not nova though supernova; a catastrophic explosion destroying the whole star or the most part of it can indeed be as bright as the whole 'island universe'. Eventually, in 1952 Walter Baade (1893-1960) distinguished stellar populations I an II. This led to the recalibration of the distance ladder as Cepheids of different populations follow different period-luminosity relations. The size of the Galaxy was estimated to be of 100, 000 light years which made our Milky Way an ordinary stellar system among others. Both the Sharpley and Curtis models of the Galaxy turned out to be partially wrong and partially right, with the truth lying somewhere in between.

At this point we finish this journey into the history of astronomy and turn our attention to the picture of the Milky Way as we know it now, in the epoch of large-scale surveys and space observatories.

1.3 The modern picture of the Milky Way

The Milky Way is a barred spiral galaxy, that, according to the Hubble classification, belongs to the category of late-type SBbc spirals[2]. Roughly the Galaxy can be described as a superposition of several flattened and spheroidal components. To the flattened part belong the thin and thick disks, as well as gaseous and dust layers. The spheroidal component is represented by the

[2]The Hubble classification of galaxies originally attempted to explain the galactic evolution based on their observed morphological features. The proposed scenario outlined the evolution direction from the early-type elliptical galaxies towards the late-type flattened spiral systems. Although this picture was later proven wrong, referring to ellipticals and spirals as 'early-type' and 'late-type' galaxies respectively, remains widely used. An alternative classification worth mentioning here is the de Vaucouleurs three-dimensional scheme (de Vaucouleurs, 1959). Also significant attempts are being made to develop the classification of galaxies using artificial neural networks, which would allow to minimise the input expectations and the impact of the human visual perception (Goderya and Lolling, 2002; Hocking et al., 2018).

barred bulge and the halo consisting of stars and non-baryonic dark matter (DM) (Fig. 1.1).

Being a part of the Galaxy, we cannot have a look at the Milky Way as a whole, such that the reconstruction of the Galactic spatial structure and kinematics is challenging and requires precise distance and spatial velocity measurements, alongside with an understanding of the solar motion and its position in the Galactic disk. Below we summarise the present-day knowledge of the properties of the Galactic components as derived on the basis of astrometric, spectroscopic and multi-band observations from the last decades[3].

1.3.1 The disk

Being a main reservoir of the stellar content of the Galaxy, the disk component has a complex morphology, chemical composition, and kinematics, which reflect the complexity of the underlying physical processes driving disk evolution. It spans up to Galactocentric distances of 15-20 kpc and, perhaps, even further (López-Corredoira et al., 2018). There is numerous observational evidence implying that the Galactic disk can be separated into two components, the *thin* and *thick* disks, associated with the different mechanisms of formation and/or stages of evolution. However, this separation remains a controversial topic. The most recent studies demonstrate that the thin and thick disks have a significant overlap in space and chemical abundance, and also have comparable ages and kinematics (see below). This may imply that our modern definitions of the two disks is misleading (Hayden et al., 2017), or that an alternative separation into components can better trace the Galactic evolution (e.g., in Haywood et al., 2013 inner and outer disks are proposed to replace the traditional thin and thick disk concepts).

The thin disk. The thin disk consists of α-poor metal-rich populations[4] of different ages including the youngest stars. The thin-disk stars show ordered rotation moving on almost circular orbits around the Galactic center (GC) with a typical circular velocity of ~ 240 km s^{-1} (velocity at the solar radius, $R_0 \approx 8$ kpc) and almost flat rotation curve (see Chapter 4). In a zero-order approximation the thin (and thick) disk(s) can be assumed axisymmetric and resting in a steady state; however, there is a number of features that violate this simplified picture.

The youngest thin-disk populations (e.g., OB stars, which are primarily found in open clusters) trace a well-developed spiral structure. A comprehensive pattern of the Milky Way spiral arms is still not known in full detail, but its main features are already well-established:

[3] We note that this overview is not intended to be exhaustive as the field of galactic astronomy is developing rapidly; also some topics are covered in a biased way and many interesting questions are not discussed, as this would lead us too far from the main topic of this research.

[4] We use a conventional definition of metallicity as the relative iron-to-hydrogen abundance in a given star compared to the solar value: $[\mathrm{Fe/H}] = \log_{10}[(\mathrm{Fe/H})_*/(\mathrm{Fe/H})_\odot]$, where Fe and H correspond to number of iron and hydrogen atoms per unit volume. Sometimes we also use the notation Z, which is defined as the fraction of mass in metals (elements heavier than helium).

The α-elements are chemical elements with even atomic numbers that are produced via the capture of α-particles in the interiors of massive stars (mostly with masses $\gtrsim 8M_\odot$) and include O, Mg, Si, Ca and Ti. The short-lived massive stars produce a certain ratio of the α and iron-peak elements that are subsequently ejected into the interstellar medium (ISM) during the explosions of core-collapse supernovae (SNe Type II). The long-lived low-mass stars, on the other hand, contribute mainly to the production of iron-peak elements, and some of them later explode as SNe Type Ia. Due to the longer evolution of the SNe Type Ia progenitors, the ratio [α/Fe] should decrease with time; the absolute values of this ratio contain information on the Galactic star formation history, and thus can be used to discern different star formation phases. The notation [α/Fe] usually refers to the relative abundance of the iron and a mean over Mg, Si, Ca and Ti, though also combinations of three elements are sometimes used in the literature to represent α-abundance.

there are four long logarithmic spiral arms (Churchwell et al., 2009; Vallée, 2014, 2017) that set up a natural environment for the present-day star formation by producing shock waves and triggering formation of young stars and HII regions via Jeans instability. The observed displacement between the spiral arm density peaks identified with gaseous and stellar tracers (Hou and Han, 2015) supports a quasi-stationary density wave theory (Roberts, 1969; Dobbs and Baba, 2014) as a mechanism responsible for the formation of spirals in the Galaxy.

The disk plane is known to be warped; although, the starting distance of the warp is still debated. The authors of Reylé et al. (2009) conclude that the warp starts outside the solar annular, while other studies find that the disk warp takes its origin at Galactocentric distance of ~ 7 kpc (Drimmel and Spergel, 2001; Schönrich and Dehnen, 2018). Moreover, according to Schönrich and Dehnen (2018) a smooth monotonous warp alone cannot explain the observed variations in kinematics of the high-quality data from the Tycho-Gaia Astrometric Solution catalogue (TGAS, Michalik et al., 2015; Lindegren et al., 2016) and Radial Velocity Experiment survey (RAVE, Steinmetz et al., 2006), but there is an additional wave-like component, that may take origin from the interaction with the Sagittarius dwarf galaxy on a ~ 1 Gyr time scale.

The radial structure of the thin disk can be described well by an exponential law with a scale length of ~ 2.5 kpc, though the value is sensitive to metallicity (Golubov et al., 2013). The vertical structure of the thin disk is often assumed to be exponential as well, but the observed vertical number density profiles have a core near the Galactic plane (Holmberg and Flynn, 2000). The thin disk is characterised by a half-thickness of ~ 400 pc.

The thick disk. It is generally recognised that the thick disk is an old, α-rich and metal-poor population formed on a short time scale. The span of this time scale varies significantly over different studies (4-5 Gyr in Haywood et al., 2013, but less than 2 Gyr with as low as 0.1 Gyr in the two-infall chemical models from Grisoni et al., 2017, 2018).

The fact that the spiral and S0 galaxies have two-component disks was already evident from the photometric studies of edge-on galaxies (Burstein, 1979; Tsikoudi, 1979; van der Kruit and Searle, 1981), though the nature of the thicker and less dense component was still unclear. The early star counts towards the Galactic poles also identified a second disk component in the Milky Way (Gilmore and Reid, 1983, see also more recent results using the Sloan Digital Sky Survey (SDSS) star counts in Jurić et al., 2008). The authors found that the vertical disk density profile cannot be approximated by a single exponential law with a scale height of 300 pc: a second component with a larger scale height of $\sim 1\,350$ pc is needed. The origin of this additional thick component was associated with the Galactic spheroid flattened in response to the disk gravitational potential. The first attempts to separate the thin- and thick-disk stars were based on spatial location and kinematic properties of populations, but these criteria were recently replaced by a more robust set based on the chemical composition of stellar populations as more in-depth studies of the chemical properties of the Galactic disk followed the pioneering star-count papers.

An extensive study of G-dwarfs from the Sloan Extension for Galactic Understanding and Exploration (SEGUE, Yanny et al., 2009) revealed a bimodality in the α-Fe abundance plane (Lee et al., 2011). The stars, when separated into two populations according to their chemistry (α-rich metal-poor and α-poor metal-rich), also demonstrate different kinematics and spatial distribution, which supports the existence of two independent Galactic disks. Although the reported bimodality in the abundance plane was questioned (Bovy et al., 2012b,c), the newer and high-precision spectroscopic data from the SDSS III Apache Point Observatory Galac-

tic Evolution Experiment (SDSS-III/APOGEE, Eisenstein et al., 2011) confidently confirm the existence of two peaks in the α-Fe plane and, in other words, two distinct evolutionary epochs. However, the recent works on the age-metallicity structure of the Galactic disks confirm the complex interrelation between the thin and thick disks of our Galaxy (Bovy et al., 2016b; Mackereth et al., 2017). In particular, though the distribution of stars in the abundance plane is clearly bimodal, when studied in narrow α-Fe bins, the stellar populations show a smooth transition in terms of scale heights from the thin to the thick disk.

The ratio of the thin- and thick-disk scale lengths is a useful clue to the formation scenario of the Galaxy. The photometrically defined thick disks of external galaxies are more extended than their thin disks (Yoachim and Dalcanton, 2006). The same trend is identified for the Milky Way when the geometric criteria are used to separate the disks (Jurić et al., 2008). However, the Milky Way thick disk, defined chemically, is more concentrated than the thin disk; the corresponding scale length is ∼2 kpc (Bensby et al., 2011; Cheng et al., 2012). This apparent contradiction is addressed in Minchev et al. (2015) on the basis of hydrodynamic simulations of several Milky Way-like galaxies. The author shows that at large galactocentric distances a geometrically defined thick disk essentially consists of the flared thin disk populations, such that its scale length appears larger than for a chemically defined thick disk.

The thick disk stellar populations are overall more dynamically heated than those of the thin disk, which can be demonstrated by comparison of their age-velocity dispersion correlations. The authors of Quillen and Garnett (2000) studied F and G stars in the solar neighbourhood and reported an abrupt increase in the vertical velocity dispersion for the stars with ages larger than ~ 9 Gyr. A similar result is found in Casagrande et al. (2011) for the total velocity dispersion of the FG(K) dwarfs from Geneva-Copenhagen survey (GCS, Nordström et al., 2004). This difference in the velocity dispersion of the thin- and thick-disk stars is confirmed by the recent study of the local sample from the Large sky Area Multi-Object Spectroscopic Telescope (LAMOST) General Survey (Luo et al., 2015) and the TGAS data (Yu and Liu, 2018). Among other things, the authors of Lee et al. (2011) investigated the tangential velocity V_ϕ of the thin- and thick-disk stars from SEGUE G-dwarf sample in the extended solar neighbourhood. They found that in general the stars of a chemically defined thick disk rotate around the GC more slowly than the thin-disk stars: the thick-disk population lags from the circular motion by ~ 40 km s^{-1}, while for the thin disk this lag is only ~ 10 km s^{-1} (the values are given for the solar radius, $R_0 \approx 8$ kpc)[5]. Some authors (Haywood et al., 2013; Hayden et al., 2017) reported an increase of the vertical velocity dispersion with the age of the thick-disk populations. On the other hand, within the framework of Jeans analysis developed in Sysoliatina et al. (2018a), the α-rich metal-poor thick disk behaves as a well-mixed kinematically homogeneous population.

There are several formation mechanisms proposed to explain the observed properties of the thick disk:

1. The thick disk is made of the thin disk-stars:
   (a) Some fraction of the early thin disk was heated by the satellite accretion (Freeman, 1987; Villalobos and Helmi, 2009).
   (b) The radial migration started to take effect as the transient structures such as a bar and spiral arms formed during the Galactic evolution (Röser et al., 2008;

[5] The difference between the mean tangential rotation velocity $\overline{V_\phi}$ of a stellar population and the circular velocity V_c at a given Galactocentric distance is the so-called asymmetric drift, V_a. The larger values of the asymmetric drift for the dynamically heated populations relates to the fact that dynamically heated stars move on perturbed orbits and need in general more time to complete a revolution around the GC (see Chapter 4 for more details).

Schönrich and Binney, 2009b; Minchev et al., 2015).

2. The thick-disk stars were born outside the Milky Way: this Galactic component is a debris of the accreted Milky Way satellites disrupted in its gravitational potential (Abadi et al., 2003).
3. The thick disk formed *in situ* as a result of gas-rich mergers (Brook et al., 2004) or the evolution of a clumpy young disk (Bournaud et al., 2009).

The plausibility of the thick disk formation scenarios can be tested with modelling of stellar orbital parameters, that can also be reconstructed from the observed kinematics given a plausible Milky Way gravitational potential. The recent studies of the distribution of orbital eccentricities are more likely to support the gas-rich merger scenario (Sales et al., 2009; Lee et al., 2011).

Gas and dust. The Galactic disk consists not only of stars, but also of gas from which these stars form and which they eject back to the interstellar medium (ISM) during their life cycles, as well as of dust produced in the atmospheres of the late-type giants or during nova and supernova explosions.

The gas found in the ISM consists primarily of hydrogen and exists in two main phases:

1. *Cold molecular gas.* It has low temperatures of T≈ 10-70 K and high densities of $\rho \approx 10^8$ m^{-3} and forms molecular clouds: the environment in which stars born. Molecular gas is strongly concentrated close to the Galactic plane and traces the spiral structure. Being a symmetric molecule, H_2 does not radiate strongly. For tracing the molecular hydrogen an emission lines of carbon monoxide CO is used, which is then converted to the density of H_2 assuming an X-factor, a universal ratio between CO and H_2 (Dame et al., 2001; Dame and Thaddeus, 2004; Heyer and Dame, 2015).
2. *Warm atomic gas.* This phase is characterised by a variety of temperatures (up to a few 10^3 K) and densities (can be as low as $\sim 10^5$ m^{-3}). Atomic hydrogen has a hotter diffuse component, but also forms HI clouds. The spatial distribution of the atomic hydrogen can be traced with the 21-cm hydrogen emission line, that originates from a transition between two ground states of the hydrogen atom differing by nucleus-electron spins orientations. Atomic gas also traces a spiral structure (Levine et al., 2006a) and, similarly to the stellar disk, is warped (Levine et al., 2006b).

Dust makes up only ∼1% of the ISM mass, but it nevertheless plays an important role in Galactic star formation and has an impact on the observed properties of stellar light. Dust particles provide the necessary conditions for the formation of H_2 molecules and their subsequent condensation into molecular clouds: molecular hydrogen forms primarily on the surface of dust grains (Gould and Salpeter, 1963; Hollenbach and Salpeter, 1971), which then effectively shield H_2 from the high-energetic interstellar radiation and allow its cooling through particle collisions.

The stellar light that penetrates through the dusty ISM appears dimmer and redder as the dust scatters and absorbs the radiation. The average extinction in Milky Way plane outside of dark clouds is ~ 1 mag kpc^{-1}. Dust grains re-radiate the absorbed energy in the mid- and far-infrared (MIR and FIR) wavelength range, such that the distribution of dust can be studied with the IR satellites and surveys (Schlegel et al., 1998; Drimmel et al., 2003). The most recent dust maps covering large distance range is based on the Pan-STARRS data (Green et al., 2015, 2018); a new dust map of the solar neighbourhood is presented in Capitanio et al. (2017).

The broad interstellar absorption bands are used for studying the composition of dust grains, and corresponding models suggest that the majority of interstellar dust particles are graphites, silicates and polycyclic aromatic hydrocarbons. As the dust grains also polarise the stellar light, they have non-spherical shapes and are characterised by anisotropic orientation following the Galactic magnetic field lines. Thus, the polarised radio emission from the dust particles can probe the complex structure of the Milky Way magnetic field (Landecker, 2012).

1.3.2 The bulge

The inner region of the Milky Way, within ~ 3 kpc, is occupied by the bulge. Due to extremely high extinction in the optical wavelength range in bulge direction[6], systematic studies of the bulge region became possible only after the development of radio and IR astronomy. IR observations with the Cosmic Background Explorer (COBE) satellite as well as the Two Micron All Sky Survey (2MASS, Skrutskie et al., 2006) and the VISTA Variables in the Via Lactea survey (VVV, Minniti et al., 2010) contributed greatly to our current understanding of the bulge structure and its stellar content. Another important tool for bulge studies is gravitational microlensing. Microlensing events are systematically explored in the framework of such surveys as Massive Compact Halo Object survey (MACHO, Bennett et al., 1995), Optical Gravitational Lensing Experiment (OGLE, Udalski et al., 2015), and Microlensing Observations in Astrophysics project (MOA, Bond et al., 2001). Due to a significant (up to a factor of $\sim$100) amplification of stellar brightness during the lensing event, it is possible to obtain high signal-to-noise stellar spectrum during relatively short exposure, and by these means we can study the chemical composition and kinematics of the bulge region.

The Milky Way bulge is now recognised as a boxy peanut-shaped (Dwek et al., 1995; Wegg et al., 2015) pseudo bulge (Kormendy and Kennicutt, 2004) which formed primarily from the thin and thick disks material via secular evolution. There is a bar residing in the bulge oriented at $\sim 27 \pm 2^\circ$ with respect to the line of sight connecting the Sun with the GC (Wegg et al., 2015). The dynamical model of the bar region presented in Portail et al. (2017) points to a bar pattern speed of $\Omega_b = 39 \pm 3.5$ km s^{-1} kpc^{-1}. The vertical heating of the bulge is attributed to the effect of the dynamical vertical instability triggered by the bar at some point in the past (so-called buckling, Combes and Sanders, 1981). This implies that the bulge is not a distinct Galactic component but essentially the bar seen edge-on and made of disk stars. This also means that the bulge as a structure is younger than its stars.

Though the pseudo bulge component dominates the Milky Way bulge, a less dominant classical bulge, that forms via mergers of gas-rich galaxies or coalescence of giant disk clumps (Elmegreen et al., 2008; Bournaud et al., 2009), might also be present. This possibility was tested in Shen et al. (2010) by studying the vertical velocity dispersion of the bulge with the data from Bulge Radial Velocity Assay spectroscopic survey (BRAVA, Rich et al., 2007). The authors found that the contribution of the classical bulge component must be less than 8% of the disk mass and is not necessary to explain the data: the model with a pseudo bulge alone confidently fits the observed kinematics (see also Di Matteo et al., 2014). Together with the cylindrical rotation of the bulge (Howard et al., 2009), this sets a strong constrain on the presence of the classical component in the Milky Way bulge.

A recent study that made use of the ages of 90 microlensed bulge dwarfs, turn-off, and

[6] In the direction of the GC, extinction is as high as $A_V \approx 28$ mag, and only in select directions like Baade's Window are observations in optical range possible.

subgiant stars shows that the bulge stars are not exclusively old: $\sim 20\%$ of stars with metallicities between [Fe/H] ≈ -0.5 dex and solar as well as about one-third of stars with super-solar metallicity are younger than 8 Gyr (Bensby et al., 2017). In terms of chemical abundances the bulge stars are very similar to the inner disk (Bensby et al., 2017), being somewhat enriched in different elements. The bulge metallicity distribution is very wide and has multiple (up to five) peaks (Ness et al., 2013) which are associated with the different components originating from the different regions of the thin and thick disks, as well as halo and/or classical bulge component as discussed in Di Matteo et al. (2014) on the basis of dissipationless N-body simulations. The same study implies that the the bulge/bar stars of a Milky Way-like galaxy originate from the distances up to the outer Linbland resonance (OLR)[7].

Even though our understanding of the bulge morphology, its stellar population properties and origin has improved greatly during the last decade, there are still questions to be answered. What is the age of the bar structure (not the stars it is made of)? Did the bulge have a gas accretion history different from that of the disk? What was the rate of bar growth at different epochs?

1.3.3 The Galactic center

The innermost ~10 pc of the Galaxy harbors the central engine of the Milky Way with a supermassive black hole (SMBH) residing in its core. Due to a small physical size and remoteness, the GC is even more difficult to study than the bulge, and is achievable only in X-ray, IR and radio wavelength ranges.

Within a range of distances of about 2-10 pc from the GC a circumnuclear disk (CND) is located, a torus-shaped warped disk of warm molecular gas inclined by about 20° with respect to the midplane. It has a mass of $2\text{-}5 \cdot 10^4\ M_\odot$ (Mezger et al., 1996) and is supposedly fed by the mass infall from molecular clouds located further out at ~ 20 pc and connected to the CND with several dense gas streamers (Hsieh et al., 2017; Tsuboi et al., 2018). The CND has complex kinematics: its outermost parts are not in a steady state and fall in to the GC at a speed of ~ 50 km s^{-1} (Oka et al., 2011), while the submillimeter observations in different molecular emission lines of the innermost ~ 4 pc show that the inner region of the CND predominantly rotates at a speed of ~ 100 km s^{-1} (Martín et al., 2012). The CND has a sharp inner edge at ~ 1.7 pc, where a spiral-like structure of ionized gas known as the Galactic Center Mini-Spiral (GCMS) takes its origin (see Fig. 1.2).

Alongside the gas, a massive stellar agglomerate is located in the GC region. This nuclear star cluster (NSC) has an effective radius of a few parsecs and a mass of $\sim 10^7\ M_\odot$ (Launhardt et al., 2002). The bulk of the NSC stars has ages larger than 5 Gyr, but also young OB and Wolf-Rayet (WR) stars are observed within the inner 0.5 pc from the GC. The origin of these stars is still a matter of debate. The thin stellar disk of O and WR stars is thought to be formed *in situ* as a result of a collision between the gas clumps falling into the GC (Sanders, 1998). The presence of B stars, which have eccentric and randomly inclined orbits, is often explained in terms of the binary disruption scenario (Hills, 1988; Bromley et al., 2012; Madigan et al., 2014).

[7] Together with corotation and inner Linbland resonances the OLR is one of the fundamental resonances that are triggered by a bi-symmetric bar. (Binney and Tremaine, 2008; Dehnen, 2000). The OLR occurs when $\Omega_b - \Omega(R) = -\kappa(R)$, where Ω_b is a steady pattern speed of the bar, $\Omega(R)$ is a circular frequency and $\kappa(R)$ corresponds to the epicycle frequency. The OLR of the Galactic bar is located at $\sim 6-9$ kpc.

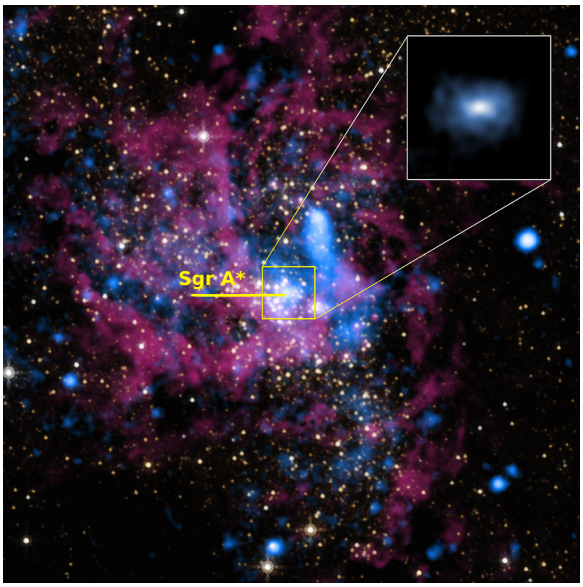

Figure 1.2: Composite image of the innermost ~ 2.3 pc combining X-ray emission from Chandra X-ray Observatory (blue) with NIR and MIR emission from the Hubble Space Telescope (shown in yellow and red, respectively). The GCMS structure is clearly traced in the MIR wavelength range; the close-up shows a diffuse X-ray emission from the most massive stars of the NSC. Credit: X-ray: NASA/UMass/D.Wang et al., IR: NASA/STScI.

A few tens of B stars, typically at distances of 0.01 pc from the GC, form a so-called S-star cluster. The enclosed mass determined from the observed dynamics of S stars is $\sim 4.3\ 10^6\ M_\odot$, which implies the presence of a SMBH (Gillessen et al., 2017). A radio source Sagittarius A* (Sgr A*) detected with the Very Long Baseline Interferometry (VLBI) is associated with the SMBH and a dynamic center of the Milky Way.

Sgr A* shows very low level of activity in comparison to other galaxies, which is probably related to a low mass infall rate towards the SMBH. However, such recently detected structures as radiolobes and Fermi bubbles indicate that the activity of the central engine of the Milky Way might have been significantly higher in the past and varies with time.

1.3.4 The halo

A spherical component of the Galaxy, which embeds the bulge and the disk, is known as the halo. The Milky Way halo, similar to the halos of other galaxies, is dominated by DM, but also includes gas and stars.

Baryonic halo. The stellar halo consists of metal-poor ([Fe/H] $\lesssim -0.8$) old stars, the majority of which do not show ordered rotation, but move around the GC on highly eccentric, randomly inclined orbits. The density profile of the stellar halo is usually parametrised with a two-component power law with power indices of -2.5 ± 0.3 and $-(3.7\text{-}5)$ for the inner and outer halo, respectively, and a break radius of 25 ± 10 kpc (Bland-Hawthorn and Gerhard, 2016). The shape of the stellar halo is found to be not perfectly spherical, but flattened with the value of flattening parameter being in the range of 0.6-0.8 according to most studies (Deason et al., 2011; Pila-Díez et al., 2015). The two halo components are believed to have different formation histories: the inner halo is a result of accretion of few Milky Way satellite galaxies about 10 Gyr ago; the outer halo was formed more recently via accretion events and, perhaps partly, *in situ* via disk heating and star formation from the gas stripped off from the disrupted satellites.

The mass distribution in the halo is not homogeneous. There are numerous chemical abundance and density substructures in the form of stellar streams as well as ~ 200 globular

clusters distributed almost spherically around the GC. The halo is the perfect place to search for the oldest stars and to study the Milky Way accretion history, as well as to probe its gravitational potential.

The halo also contains a massive gas reservoir in the form of a hot ionized corona. At near-plane distances of about 2-15 kpc from the Galactic disk, the infalling hypervelocity clouds of molecular gas are detected. They are associated with the cooled gas previously ejected into the halo from the disk during supernova explosions (galactic fountains).

DM halo. About 95% of the total Milky Way mass is made up of DM. This means that we do not know what the dominant fraction of the Galaxy is made of. In comparison to the other Galactic components, the DM is definitely much poorly studied as we do not know its nature, cannot trace its motion or study its spatial distribution by direct methods. We infer its properties by reconstructing the gravitational potential of the Galaxy via probing kinematics of the baryonic matter (Chapter 4). The shape of DM halo is still not fully constrained, both spherical and oblate models are used. Usually the DM halo is characterised by the Navarro-Frenk-White (NFW) profile (Navarro et al., 1995). However, as it was shown by Binney and Piffl (2015) on the base of a self-consistent dynamical model of the Galaxy and a sample of RAVE giants, the NFW profile might be inconsistent with the distribution of DM in the Milky Way. Further analysis of the RAVE data showed that the DM halo has a centrally heated cored profile (Cole and Binney, 2017). A strong constrain on the DM halo shape comes from the analysis of a stellar stream related to the Sagittarius (Sgr) dwarf galaxy. In order to explain the observed shape of Sgr stream, the triaxial model of the DM halo is proposed, that is flattened towards the Galactic disk (Vera-Ciro and Helmi, 2013).

1.4 Galaxies in a cosmological context

The age of the Milky Way and other galaxies in the present-day Universe can be estimated from the ages of their oldest individual stars (i.e., members of the old halo population, long-lived white dwarfs or turn-off stars), as well as by means of nuclear cosmochronology[8]. Being in agreement with each other, different methods imply that the oldest stars in the Milky Way and the Local Group have ages of $\gtrsim 13$ Gyr (Pasquini et al., 2004; Chen et al., 2016; Wagner-Kaiser et al., 2017; Aguado et al., 2018); this is only slightly lower than the age of the Universe of ~ 13.8 Gyr as obtained in the framework of the standard cosmological model with the cold DM and a nonzero cosmological constant (ΛCDM model) (Planck Collaboration et al., 2018). In this respect, the structure formation processes, which eventually led to the formation of the present-day cosmic web with galaxies as its essential ingredient, take their origin in the very early epoch of the Universe existence; this implies that the full understanding of the evolution of galaxies can be achieved only with the cosmological context taken into account.

[8]The method of cosmochoronology uses the observed abundances of radioactive elements to set a limit to ages of cosmic bodies. A common approach implies that the observed abundances of long-lived radioactive elements with considerably different half-life periods are extrapolated back in time, under the assumption about their initial ratios and production rate during galactic evolution.

1.4.1 The early Universe

According to the present-day cosmological paradigm, which is supported by the numerous independent observations, the Universe originates from an extremely hot, dense, and compact state, which is a product of the Big Bang (BB) event dating back to ~ 13.8 Gyr ago. The earliest cosmic time which can be addressed in the framework of the modern physics is the Planck time corresponding to $\sim 10^{-43}$ s after the BB. During the earlier evolutionary stage, also known as the Planck epoch, all four physical interactions remain merged: they have the same strength and are indistinguishable, such that the theory of quantum gravity would be required to characterise the state of matter under these conditions. As it is commonly believed, the Universe underwent a stage of inflation which started around the Plank time, when the gravitational interaction separated from the merged strong and electroweak forces, and lasted until 10^{-32}-10^{-33} s after the BB. During the inflation epoch, our Universe has experienced a violent expansion; as a result, its size increased by a factor of $\sim e^{60}$. Thus, a part of the Universe which is now available for observations originates from a casually connected region; this naturally explains the observed large-scale isotropy and homogeneity of matter distribution, as well as flatness of space (according to the latest results of the Planck satellite, the space curvature is zero to a 1σ accuracy of 0.2%, Planck Collaboration et al., 2018). The driving force of the inflation is attributed to a scalar field which in the end of inflation stage decays to transfer its energy into the form of the baryonic and DM particles, as well as radiation. The existence of matter in our Universe is a result of a slight asymmetry in the number of produced protons, electrons and neutrons over their antiparticles, such that after annihilation of matter and antimatter a small fraction of particles remained to form stars, galaxies, and large-scale cosmic structures. The origin and severity of this asymmetry is fossilised in the baryon-to-photon ratio of $\sim 10^{-10}$, and has not yet been explained within the framework of particle physics.

After all the four interactions had separated from each other and the annihilation of matter and antimatter occurred, the BB nucleosynthesis (BBN) led to the formation of several types of light nuclei which finally defined the chemical composition of the primordial raw material of the first stars. A basis of the BBN theory was established in the pioneering works by Lemaître (1931), where the Universe was assumed to take its origin from a hot explosion, and Gamov (1942, 1946), where the processes of element synthesis in the early Universe were addressed; the theory was further developed in Wagoner et al. (1967). The BBN theory predicts the primordial synthesis of such light elements as H, D, ^{3}He, ^{4}He, and ^{7}Li. The abundances of these elements measured in regions with a minimal pollution by the products of stellar nucleosynthesis (such as the oldest stars in the Local Group or gas in distant quasars) are consistent with the BBN predictions within $\sim$10%. In overall, the BBN phase results in a primordial hot gas composed by 75% of H and 25% of ^{4}He, with only negligible traces of other light atoms.

The earliest cosmic epoch which can be observed directly dates back to $\sim 380,000$ yr after the BB. At that point the temperature of the medium decreased to $\sim 3\,000$ K, and the recombination of hydrogen atoms became possible. From that moment on, the Universe became transparent for light, as matter and radiation departed from the thermodynamic equilibrium. The radiation emitted from the surface of last scattering cooled down as the Universe continued to expand, and the present-day temperature of this cosmic microwave background (CMB) is only ~ 2.7 K with the almost perfect black body spectrum. The CMB radiation provides us an extremely valuable information on the matter distribution in the early Universe, and since its discovery described in Penzias and Wilson (1965) and interpretation presented by Dicke et al. (1965), the CMB has been closely studied, both with the help of ground-based interferometry

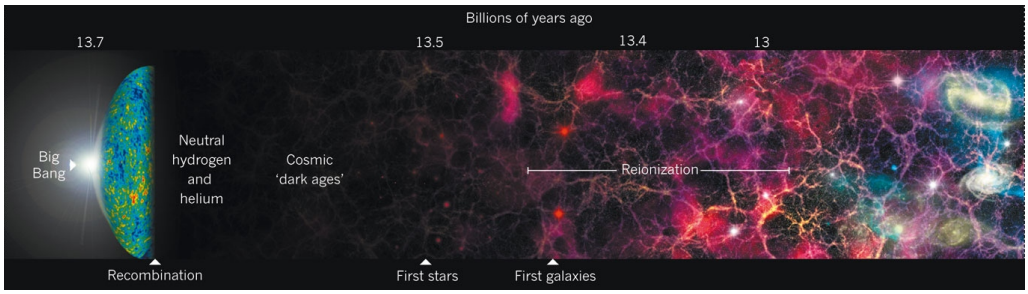

Figure 1.3: Cosmic evolution from the BB to the present day. The key evolutionary epochs are shown: the inflation stage at the end of which radiation and particles were formed, the recombination which gave rise to the CMB, the dark ages preceding formation of the first stars, the reionization of the IGM and, finally, the development of the cosmic web with galaxies as its essential component. Credit: NASA/WMAP Science Team; R. Ellis (Caltech).

and space observatories such as COBE, Wilkinson Microwave Anisotropy Probe (WMAP) and Planck satellites. The angular variations of the CMB temperature reflect the spatial distribution of density inhomogeneities at the moment of the last scattering; the relative variations of the CMB temperature with respect to the mean value are as low as $\sim 10^{-5}$ implying the same order for the relative density fluctuations which became the seeds for the subsequent structure growth.

The temperature of the primordial gas continued to decrease due to collisional processes, ionization, free-free emission and cooling by the molecular hydrogen. Finally, driven by the Jeans instability, the gas fragmented and collapsed to form the first stars (so-called Population III), most of which are hypothesised to be extremely luminous, massive, and short-lived. The intense radiation of these first stars triggered the reionization of the intergalactic medium (IGM) resulting in intergalactic light absorption which is now observed in the spectra of quasars. The Population III stars also enriched the IGM with heavy elements allowing much more effective gas cooling; thus, the conditions required for the rapid star formation and build-up of the first galaxies were set up (see Fig. 1.3).

1.4.2 High-redshift galaxies

Due to the fact that the light propagates with the final speed c, we can 'see' the past of our Universe by observing distant galaxies. From the systematic studies of the galaxies at different redshifts z[9], a general picture of the galactic evolution over cosmic time can be shaped up.

The recent progress in the high-redshift observations is strongly associated with the deep fields of the Hubble Space Telescope (HST). Several fields of a few acrseconds across were observed with the effective exposures of the order of tens of hours or days; among those are Hubble Deep Field (HDF), Hubble Ultra Deep Field (HUDF) and Hubble eXtreme Deep Field (HXDF, Fig. 1.4) taken in several optical filters and reaching a limiting brightness of $\sim$ 29-30 mag. As a result, tens of thousands of distant galaxies were identified, many lying at redshifts $z \gtrsim 5$. The spectroscopic surveys with limiting redshifts of $z \sim$ 1-1.4 such as the Wigglez Dark Energy Survey (Parkinson et al., 2012), the DEEP2 Survey (Newman et al., 2013) and the

[9] The redshift is defined through the observed reddening of a given spectral line which occurs due to the cosmic expansion, $z = \lambda_0/\lambda - 1$. Here λ and λ_0 are the measured and rest-frame line wavelengths. As the relations between redshift, cosmic time and distance are model-dependent, the redshift, being a directly measured quantity, is often used to refer to the distant objects.

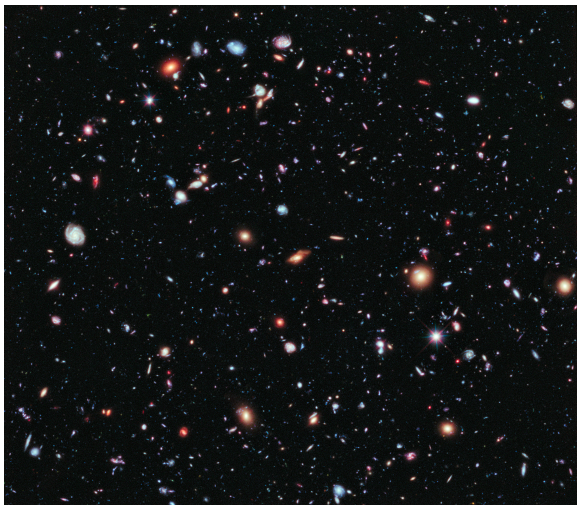

Figure 1.4: HXDF with a side of $\sim 3.4'$ shows a patch of the southern sky in the Fornax constellation. The total exposure time is $\sim 2 \cdot 10^6$ s, or about 22 days. The HXDF is composed from a series of images obtained with HST during 10 years of observations in nine photometric bands in optical and NIR. There are more than 5 500 galaxies identified at the HXDF. Credit: NASA, ESA, G. Illingworth, D. Magee, and P. Oesch (University of California, Santa Cruz), R. Bouwens (Leiden University), and the HUDF09 Team.

VIMOS Public Extragalactic Redshift Survey (VIPERS, Garilli et al., 2014) unravel the evolution of the cosmic web structure starting from an epoch when the Universe was about half of its present-day age. These results also constitute a training set for the SDSS all-sky multiband data, which give a systematic overview of $\sim 10^6$ galaxies at redshifts $z \lesssim 0.8$. Additionally, the low-resolution spectroscopic extension of the Cosmic Evolution Survey (zCOSMOS, Lilly et al., 2009) contains $\sim 10,000$ of galaxies up to redshift $z \sim 3$, and the relatively high-resolution spectroscopy performed by the Multi Unit Spectroscopic Explorer (MUSE, Bacon et al., 2010) allows to peer into the distant Universe up to redshift $z \sim 6$. Our knowledge of the more distant Universe remains fragmentary; the strong gravitational lensing effects prove to be highly useful in this distance regime as clusters of galaxies may serve as natural telescopes to widen our knowledge of the distant quasars and galaxies. The most distant galactic object with a confirmed redshift known to date is GN-z11 at $z = 11.09$ (Oesch et al., 2016), which in a framework of the ΛCDM model corresponds to the first few Myr after the BB.

All this variety of the observational data show that the morphological properties of galaxies change with redshift, i.e., with cosmic time. High-redshift galaxies do not fit into the Hubble classification any more. The fraction of irregular galaxies increase steadily with redshift, and at the same time the galactic disks become more clumpy and overall smaller. The signs of high activity, intense star formation and intergalactic interactions are also common for the distant galactic populations. Using light distribution from ultraviolet (UV) to NIR as a proxy of the galactic star formation, we can explore the cosmic star formation history (Madau and Dickinson, 2014) which is found to have a peak at $z \approx 2$ with the star formation primarily taking place in progressively lower-mass galaxies as the cosmic time increases (so-called cosmic downsizing).

Basing on the inferences from the observations of the high-redshift Universe, as well as on the recent results of hydrodynamic simulations of the galaxies and the large-scale structure (see Section 1.5.1), the following picture of the overall galactic evolution has crystallised. After the Population III stars had enriched IGM with heavy elements, such that effective gas cooling became possible, the first galaxies began to appear. Governed by the gravitational instability, DM fragmented to form massive halos, where the cold gas then settled. This gas collapsed into the flattened systems by gaining angular momentum from the tidal torques (Peebles, 1969), and the rotationally supported disks were formed. These early galaxies continued to grow due to the infall of intergalactic gas, with the overall disk formation proceeding upside-down

and inside-out in the vertical and horizontal directions, respectively (see also simulations by Bird et al., 2013). The increase of the cosmic star formation with time and its subsequent quenching after $z \approx 2$ is induced by an interplay between the overall density decrease due to cosmic expansion, the gravitational attraction, and the fact that the amount of raw material for the star formation is finite. The intergalactic interactions, which were even more common in the past when the intergalactic distances were smaller, led to a hierarchical structure growth meaning that the most massive galaxies, such as ellipticals, and the large-scale conglomerates, such as groups and clusters of galaxies, formed later as a result of merging of smaller systems. During all this time different feedback processes such as explosions of core-collapse SNe and SNe Type Ia, stellar winds and reionization of environment by the active galactic nuclei (AGN) played an important role in the evolution of cosmic structures by influencing the dynamical development of the systems, time-scale of their chemical evolution, or sometimes preventing star formation, e.g., in the low-mass DM halos (so-called missing satellites problem). So it is clear, that for comprehensive and successive modelling of the observed galactic properties, a complex treatment of the cosmological factors and stellar evolution is needed.

1.5 The Galaxy: modelling techniques

In the previous sections we outlined the evolutionary path of the cosmic structures from the early Universe to the present day. From now on we focus our discussion on the Milky Way as it is our laboratory for understanding the galactic evolution and testing different aspects of galactic models in great details.

During the last two decades the amount of data collected on the Milky Way's stellar content increased by several orders of magnitude. A typical present-day large-scale survey contains measurements for millions of objects, and with the European astrometric mission Gaia (Gaia Collaboration et al., 2016a,b) this number has already increased by another factor of ten. The core of the best dataset available so far for the Galactic studies includes the 2MASS photometry and Gaia (G, G_{BP}, G_{RP})-bands (Jordi et al., 2010; Carrasco et al., 2016; van Leeuwen et al., 2017), proper motions of the PPM-Extended catalogue (PPMX, Röser et al., 2008) and the fifth US Naval Observatory CCD Astrograph Catalogue (UCAC5, Zacharias et al., 2017), as well as astrometric parameters of the TGAS catalogue, which are already improved in the second Gaia data release (DR2, Gaia Collaboration et al., 2018). An extensive information on the stellar chemical abundances are now available from such spectroscopic surveys as GALactic Archaeology with HERMES (GALAH, Martell et al., 2017), the Gaia-ESO (Gilmore et al., 2012) as well as LAMOST, APOGEE, and RAVE surveys. Thus, we are entering an era when observational data available for Galactic stellar populations will be not only various and abundant but also precise enough to make possible the detailed study of the Galactic components and unraveling their evolution. To achieve these goals, developed and robust methods are required for a comprehensive analysis of observational data.

The construction of a fully consistent chemo-dynamical model of the Milky Way belongs to open problems of modern astronomy and is far from its closing. The formation and evolution of the Milky Way, as well as of any other galaxy, is a result of superposition and interplay of many physical processes, such that the Galaxy itself can be considered as extremely complex and composite long-going process. Each individual physical process contributing the galactic evolution has characteristic time and spatial scales. The main problem that makes galactic simulations so challenging is not the large number of physical processes to be described, as much

as the vastness of the distance range covered by their spatial scales. For example, to achieve the detailed understanding of molecular hydrogen formation on the surface of dust particles or of the nuclear fusion reactions in stellar interiors, one has to go down to molecular or even nuclear scales. In order to represent in a model the correct fraction of binary and multiple stars in a given galaxy, the understanding of matter fragmentation at molecular cloud scale is required. The secular evolution processes such as stellar radial migration, disk heating or formation of pseudo-bulge with a bar instability can influence the properties of a considerable fraction of the galactic disk, which is a kilo-parsec scale. Finally, galaxies do not exist in isolation, but interact with each other and with the intergalactic environment: major mergers have impact on the whole galaxy and can completely modify its morphology, kinematics and star formation activity.

It is not possible for a galactic model to include the detailed treatment of the full range of scales spanning from angstroms to mega-parsecs, as this would require a tremendous calculation time and a deep understanding of the underlying physics, which in many cases in not achieved yet. Instead, models use compromise medium spatial and time resolutions, while the physics on the largest and smallest scales is either modelled in a simplified parametric way or even ignored when it is justified. The overall aim of the present-day Galactic modelling is to construct such a model of the Milky Way which would be simple enough to allow a quick generation of mock samples and, at the same time, would describe all the key properties of the Galactic populations, treat them self-consistently, and reproduce the observables with a high level of accuracy. And though no existing model of the Milky Way fulfills all the aforementioned criteria, a considerable progress has been made in this direction during the last decades. Below we review the common approaches of the galactic modelling and discuss them in application to the Milky Way.

1.5.1 Numerical simulations

Due to the significant improvement of computing facilities during the last several decades, the numerical tools became one of the most powerful theoretic instruments of the modern astrophysics. By solving N-body problem numerically, we can trace the dynamic evolution of systems of very different scales such as planetary systems, stellar clusters, central regions of the galaxies and their DM haloes, clusters of galaxies and the overall large-scale structure. For the modelling of the self-gravitating collisional systems such as star- and galactic clusters, which are characterised by the lifetimes longer than their relaxation time due to two- and many-body encounters, precise direct N-body simulations are required. In the direct N-body algorythms no special simplifications are made to intergrate the equations of motion, though one-to-one particle resolution is not always possible to achieve. Usually, due to a large number of system members and a long integration times, a mass scaling is required, such that one particle in the model corresponds to a group of particles (stars) of the real system. As an example of the direct N-body simulation applied to the Galaxy, a recent high-resolution modelling of the GC region preformed with the direct N-body code NBODY6++GPU (Wang et al., 2015) can be mentioned (Panamarev et al., 2018).

In order to use N-body modelling for the large systems, special approaches are developed to allow simplification of calculation of the gravitational forces. Tree algorythm implemented in the code GADGET (Springel et al., 2001; Springel, 2005) allows to reduce the number of particle interactions by building a hierarchical space grid for the force calculation, such that the

forces from distant particles are averaged over the increasingly larger volumes. The particle-mesh (PM) code SUPERBOX uses grids of different resolution depending on the region density and is successively used for the modelling of satellite acretion (Bien et al., 2013).

The pure N-body codes do not account for the gas dynamics which has to be added separately in the framework of a hydrodynamic treatment. The most sophisticated numerical tools are now able to model the gravitational forces, gas dynamics, stellar evolution with different feedback processes, as well as to account for the magnetic fields. The simulations performed with such (magneto)hydrodynamic codes, though they are very computationally expensive and produce not fully consistent predictions depending on the calculation techniques and assumed physics, give us the most complete insight into formation and evolution of the galaxies. The large cosmological volumes has been recently modelled in the framework of several projects such as GADGET-based Millenium simulation (Springel et al., 2005), the Aquarius project (Springel et al., 2008; Scannapieco et al., 2009), and the Evolution and Assembly of GaLaxies and their Environments (EAGLE) project (Schaye et al., 2015), as well as the Illustris simulations (Vogelsberger et al., 2014; Sijacki et al., 2015) performed with the moving mesh code AREPO (Springel, 2010). All of them can successfully reproduce the overall properties of the large-scale structure and individual galaxies in the present-day Universe, including the flattened Milky Way-like systems.

1.5.2 Semi-analytic models

Unlike numerical and hydrodynamic simulations, which are time-consuming and need powerful computing resources, semi-analytic models (SAMs) can be used for the efficient exploration of the parameter space. The analytic models are handy tools for predicting quantities of interest such as star counts, chemical abundances, or spatial motions of stars. And more importantly, the model input functions such as star formation rate (SFR), age-velocity dispersion relation (AVR), age-metallicity relation (AMR), and initial mass function (IMF), give us an insight into the underlying physical processes governing the Galactic evolution.

Many semi-analytic Galactic models rest on the concept of dynamical equilibrium which implies a stationarity at dynamical time scales. When considering a galaxy as a slowly evolving system approaching relaxation, we can describe the behavior of such a system with the Jeans equations and collisionless Boltzmann equation. Using this idea, the first attempt to model evolution of the Galactic stellar content based on the classical Jeans analysis was made in the early 80$^{\text{th}}$ in Bahcall (1984a,b): the authors studied a vertical structure of the disk constructed from the several isothermal populations in the presence of a stellar halo. In order to describe the vertical disk structure they derived a combined solution of the Poisson's equation and a vertical moment of collisionless Boltzmann equation. This approach is proved to be extremely useful and gave rise to a variety of more sophisticated Galactic SAMs.

The most complete and well-developed SAM of the Milky Way is the Besançon Galaxy model (BGM, Robin et al., 2003, 2012, 2017; Czekaj et al., 2014) which accounts for the stellar, gaseous, and non-baryonic content of the Galaxy, includes non-axisymmetry of the disk in the form of the bar and the spiral arms, as well as the disk warp. The BGM treats the density-potential pair self-consistently by solving the Poisson's equation, such that the spatial distribution of the Galactic components is governed by the Galactic gravitational potential produced by these components. Its first version presented in Robin et al. (2003) is implemented in

the tool *Galaxia*[10] (Sharma et al., 2011) which allows to construct synthetic catalogues of the Milky Way and to account for the selection effects of different surveys.

Another example of the Milky Way SAM is the TRIdimensional modeL of thE GALaxy (TRILEGAL, Girardi et al., 2005; Girardi, 2016). The model is designed specifically for star-count simulations and is able to include into the mock catalogues, besides the Milky Way stars, also the field galaxies[11]. The TRILEGAL code does not attempt to reconstruct the Galactic potential, but generates star counts according to the assumed density profiles of the Galactic components, as well as the input SFR, AMR, and IMF functions.

Alongside with these chemo-dynamical models, there are also more specific ones focused explicitly on either Galactic dynamics or chemical evolution.

The Galactic dynamics can be explored in a framework of distribution functions and integrals of motion[12]. In this case the modelling approach implies two main phases: firstly, the Galaxy is assumed to be statistically steady in time and axisymmetric, such that relatively simple analytic models can be built to study the stellar orbits in a phase-space (Binney, 2012; Binney et al., 2014); secondly, the derived orbits are perturbed in order to reproduce non-axisymmetric features (Famaey et al., 2016).

The SAMs are also very useful for investigating the Galactic chemical evolution as, fortunately, chemical enrichment across the disk can be well-described analytically. Such models usually rest on several simplifying assumptions such as instantaneous recycling approximation (IRA), instantaneous and homogeneous mixing of gas, and independency of the different disk rings. However, the most recent chemical models also include infall and outflow of the gas, as well as the radial gas flows (Schönrich and Binney, 2009a,b; Kubryk et al., 2015; Grisoni et al., 2017).

As every simplified approach, SAMs have their limitations. The axisymmetric Galactic models cannot simulate spiral arms and bar, as well as such small-scale overdensities as open clusters. But what is more important, some causal relationships may be lost in SAMs as they only allow to constrain the shapes of the input functions, but not to identify the corresponding causes (e.g., in order to quantify a relative impact of the secular evolution and satellite accretion on the disk heating function, full N-body simulations are needed). Nevertheless, SAMs are useful physically-motivated models which provide us with flexible tools to describe the dynamical and chemical evolution of the Galaxy, as well as to simulate its present-day stellar content.

[10] http://galaxia.sourceforge.net

[11] http://stev.oapd.inaf.it/cgi-bin/trilegal

[12] An integral of motion is a function of the phase-space coordinates x, v which is conserved along the orbit and constrains the motion of a body. In case of axisymmetric potential one of the integrals of motion is L_z, a vertical component of the angular momentum. Two others are action integrals, J_r and J_z, characterising the radial and vertical oscillations of a given orbit (Binney and Tremaine, 2008).

Chapter 2

The semi-analytic Milky Way disk model

2.1 Local Just-Jahreiß disk model

The semi-analytic chemo-dynamic Just-Jahreiß model (hereafter JJ model) is another instance of the SAMs' class; the structure, predictions and development of the JJ model are the main subject of this work.

As we showed in Section 1.5.2, each Galactic model has its own focus. The main purpose of the JJ model is to enable a detailed study of the thin-disk vertical structure (Just and Jahreiß, 2010, hereafter Paper I). The JJ model describes an axisymmetric thin disk in a steady state consisting of a set of isothermal stellar populations moving in the total gravitational potential. The thick and gaseous disks, as well as the DM component, are added to the total local mass budget in order to treat the pair of density-potential fully self-consistently. The input functions describing the thin disk evolution are SFR, AVR, IMF, and AMR. Below we give the essential details about our treatment of each Galactic component in the JJ model of the solar neighbourhood.

- *Thin disk.* The thin disk is constructed from a set of $N_s = 480$ isothermal mono-age subpopulations[13] with ages in a range of τ = 0-12 Gyr with a fine time-resolution of $t_r = 25$ Myr[14]. The dynamical heating of the subpopulations is given by the AVR function which describes an increase of the vertical velocity dispersion $\sigma_{W,s}$ with stellar age as a result of response to the small perturbations in the gravitational potential. As it is shown in Binney and Tremaine (2008), the effect of stellar 'collisions' in galactic disks is essentially negligible, but other processes such as scattering by spiral arms or encounters with molecular clouds can lead to the dynamical heating of orbits. We model the thin-disk AVR as a power law with the vertical velocity dispersion starting at ~ 5 km s^{-1} for the newly born stars and increasing up to 25 km s^{-1} for the oldest subpopulation in the solar neighbourhood. Another input function of interest is the SFR implemented as a two-parametric analytic function. When combined with the AVR and IMF, the SFR function is a powerful tool to change the predicted star counts and age distributions. A local chemical enrichment in terms of the AMR law, prescribing a monotonous decrease

[13] Here and elsewhere the subscripts s, t, g, h refer to the thin and thick disks, gas, and the DM halo, respectively. An additional subscript b is used for the bulge later on in Section 4.3.2

[14] The relation between the Galactic time and age is simply $\tau = t_{p,s} - t$, where $t_{p,s}$ is the present-day time or age of the Galactic disk assumed to be 12 Gyr. Thus, time and age are fully interchangeable, and throughout the text we may refer to the same function in both age and time notations meaning by that a substitution of variables. In case of the gas age is given by $\tau = t_{p,g} - t$ with $t_{p,g} = 4.5$ Gyr.

of the iron abundance with age, is added to the model in order to reproduce the observed metallicity distributions.

- *Gas.* By analogy with the thin disk, the gas is formally modelled as a set of $N_g = 180$ isothermal populations that cover age range of 0-4.5 Gyr and are characterised by a scaled AVR: $\sigma_{W,g}(\tau) = s_g \sigma_{W,s}(\tau)$ with a scale parameter s_g set to 0.65. A constant 'gas formation rate' (GFR) is assumed; its value is chosen to match the observed local present-day gas surface density of $\Sigma_{g0} = 10.4\ M_\odot\ \mathrm{pc}^{-2}$.
- *Thick disk.* The thick disk is included as a single-birth population of the age of 12 Gyr with a velocity dispersion of $\sigma_{W,t} = 45.4$ km s^{-1} and a local surface density of $\Sigma_{t0} = 5.6\ M_\odot\ \mathrm{pc}^{-2}$.
- *DM component.* The spherical isothermal DM halo in a simple thin-disk approximation is added in a form of another single isothermal component with $\sigma_{W,h} = 140$ km s^{-1} and $\Sigma_{h0} = 59.9\ M_\odot\ \mathrm{pc}^{-2}$.

All described subpopulations are assumed to be in dynamic equilibrium in the total gravitational potential generated by the stellar, gaseous, and DM components of the Galaxy. In order to obtain a self-consistent potential-density pair, we iteratively solve the Poisson's equation written in the thin-disk approximation:

$$\zeta(\phi) = \int_0^\phi \frac{d\phi_1}{\sqrt{\sum_i \rho_i'(\phi_1)}}. \tag{2.1}$$

Here ζ and ϕ are dimensionless distance from the Galactic plane and the vertical gravitational potential, respectively:

$$\phi = \Phi/\sigma_e^2 \quad ; \quad \zeta = \frac{z}{z_n}, \tag{2.2}$$

with σ_e being the local vertical velocity dispersion of the oldest thin-disk stellar population and z_n playing a role of a 'natural scale height' given by $z_n^2 = \sigma_e^2/8\pi G\rho_{s0}$, where G is the gravitational constant and ρ_{s0} is the local density of the thin-disk component. Index i in Eq. 2.1 corresponds to summation over the Galactic components, and the radicands ρ_i' are given by the following expressions:

$$\begin{aligned}
\rho_s'(\phi) &= \sum_j^{N_s} \frac{SFR_j g_j}{2h_{s,j}} \frac{t_r}{\rho_{s0}} \frac{\sigma_{W,s,j}^2}{\sigma_e^2} \left[1 - \exp\left(-\phi \frac{\sigma_e^2}{\sigma_{W,s,j}^2}\right)\right] \\
\rho_g'(\phi) &= \sum_j^{N_g} \frac{GFR_j}{2h_{g,j}} \frac{t_r}{\rho_{s0}} \frac{\sigma_{W,g,j}^2}{\sigma_e^2} \left[1 - \exp\left(-\phi \frac{\sigma_e^2}{\sigma_{W,g,j}^2}\right)\right] \\
\rho_t'(\phi) &= \frac{\Sigma_{t0}}{2h_t\rho_{s0}} \frac{\sigma_t^2}{\sigma_e^2} \left[1 - \exp\left(-\phi \frac{\sigma_e^2}{\sigma_t^2}\right)\right] \\
\rho_h'(\phi) &= \frac{\Sigma_{h0}}{2h_h\rho_{s0}} \frac{\sigma_h^2}{\sigma_e^2} \left[1 - \exp\left(-\phi \frac{\sigma_e^2}{\sigma_h^2}\right)\right].
\end{aligned} \tag{2.3}$$

Values of the scale heights h_i are constrained self-consistently during the iteration procedure. The index j is introduced for shortness and corresponds to a summation over the thin-disk and gas mono-age populations. The value of $\rho_{s,0}$ is used only for normalisation and does not influence the results. Function g describes a mass loss due to stellar evolution: for each time t it

gives the relative mass fraction of a simple stellar population (SSP)[15] still existing in a form of stars (also including remnants). The mass loss function for the SSP with an initial metallicity Z is an integral:

$$g(Z,t) = 1 - \int_0^{t_p} \int_{m(t)}^{\infty} \Delta m(Z,m) \frac{dn}{dm}\, dm\, dt. \tag{2.4}$$

Here $\Delta m(Z,m)$ is a fraction of stellar mass returned to the ISM in a form of processed material as a function of metallicity and stellar mass, dn/dm is the IMF, and $m(t)$ corresponds to a limiting stellar mass, such that only stars with masses higher than $m(t)$ contribute to the stellar feedback at a given time t. The evaluation of the mass loss function is done with the code Chempy[16] (Rybizki et al., 2017). In this code the asymptotic giant branch (AGB) stars and SNe Type II are assumed to return their processed material in the end of their life; the corresponding yield tables, prescribing the fractions of the chemical elements returned to the ISM during stellar evolution, are adopted from Karakas (2010) and Nomoto et al. (2013). The ISM enrichment due to SNe Type Ia explosions is described by the yields from Seitenzahl et al. (2013) and delay time distribution (DTD) taken from Maoz et al. (2010). For the stellar lifetimes the values from Argast et al. (2000) are used. The model IMF is a four-slope broken power-law from (Rybizki, 2018, see Table 2.1). Though being sensitive to the assumed stellar feedback and lifetimes, as well as the IMF, mass loss function does not vary strongly with a variation of its input, i.e., this model element is constrained fairly well. In our model, we implement the mass loss function in several ways:

- A mass loss function of the SSP with a solar-like metallicity, Z = 0.0134, is assumed for our composite thin-disk component; this simplified treatment is used for analysis in Chapter 3.
- A composed mass loss function is constructed from $g(Z,t)$ corresponding to 480 SSPs with metallicities prescribed by the local AMR; no variation with Galactocentric distance is assumed in this case.
- The same composed mass loss function is allowed to change with Galactocentric distance, in consistency with the radial variation of the AMR law (see Section 2.5.3 and Fig. 2.7).

In Paper I the thin-disk AVR parameters were calibrated against the kinematics of main sequence (MS) stars from the *Hipparcos* catalogue (van Leeuwen, 2007) combined at the faint end with the Fourth Catalogue of Nearby Stars (CNS4, Jahreiß and Wielen, 1997). To constrain the AMR, the local metallicity distribution of the GCS F and G stars was used. The thin-disk vertical profile is found to be essentially non-exponential close to the plane, with the size of the core increasing with age and the overall half-thickness h_d = 400 pc. However, kinematic data alone do not help to disentangle SFR and IMF. Further comparison of the model to the SDSS star counts towards the north Galactic pole allowed to constrain the SFR (Just et al., 2011, Paper II). Our best local SFR has a peak at $\tau \approx 10$ Gyr and can be characterised by the mean and present-day star formation rate of 3.75 $M_\odot$ pc^{-2}Gyr^{-1} and 1.4 $M_\odot$ pc^{-2}Gyr^{-1}, correspondingly. The IMF parameters were also pinned down with the sample of *Hipparcos* data combined with the CNS5 (Rybizki and Just, 2015, Paper III, also Rybizki, 2018). At this stage, the thick-

[15] A simple stellar population is an assembly of stars born at the same time and in the same environment. The SSP can be characterised by the IMF, initial chemical composition of its material and age.

[16] https://github.com/jan-rybizki/Chempy

Thin disk
$\mathrm{SFR}(t) = \langle \mathrm{SFR} \rangle \cdot \frac{(t+t_0)t_n^3}{(t^2+t_1^2)^2}; \quad t_0 = 5.6\ \mathrm{Gyr},\ t_1 = 8.2\ \mathrm{Gyr},$ t_n and $\langle \mathrm{SFR} \rangle$ are constrained by the two normalisations : $\int_0^{t_{p,s}} \mathrm{SFR}(t)dt \equiv \langle \mathrm{SFR} \rangle t_{p,s}; \quad \int_0^{t_{p,s}} \mathrm{SFR}(t)g(t)dt \equiv \Sigma_{s0}$ with $t_{p,s} = 12\ \mathrm{Gyr},\ \Sigma_{s0} = 29.4\ \mathrm{M_\odot\,pc^{-2}}$
$\sigma_{W,s}(\tau) = \sigma_e \cdot \left(\frac{\tau+\tau_0}{t_p+\tau_0}\right)^\alpha$ with $\sigma_e = 25\ \mathrm{km\ s^{-1}},\ \tau_0 = 0.17\ \mathrm{Gyr},\ \alpha = 0.374$
$\frac{dn}{dm} = \begin{cases} k_0 m^{-1.26}, & m_{\mathrm{low}} < m < 0.5\ \mathrm{M_\odot} \\ k_1 m^{-1.49}, & 0.5\ \mathrm{M_\odot} < m < 1.39\ \mathrm{M_\odot} \\ k_2 m^{-3.02}, & 1.39\ \mathrm{M_\odot} < m < 6\ \mathrm{M_\odot} \\ k_3 m^{-2.28}, & 6\ \mathrm{M_\odot} < m < m_{\mathrm{up}} \end{cases}$ $(m_{\mathrm{low}}, m_{\mathrm{up}}) = (0.08, 100)\ \mathrm{M_\odot}$ and the coefficients $k_0 - k_3$ are constrained by $\int_{m_{\mathrm{low}}}^{m_{\mathrm{up}}} \frac{dn}{dm}\, m\, dm \equiv 1$
$[\mathrm{Fe/H}](t) = A \cdot \log Z_{\mathrm{oxy}}(t), \quad Z_{\mathrm{oxy}}(t) = Z_{\mathrm{oxy},0} + (Z_{\mathrm{oxy,p}} - Z_{\mathrm{oxy},0}) \frac{\log(1+q(t/t_p)^r)}{\log(1+q)},$ with A = 2.67, $[\mathrm{Fe/H}]_0 = -0.6$, $[\mathrm{Fe/H}]_p = 0.02$, $r = 0.55$, $q = 2$
Gas
$\mathrm{GFR}(t) = \frac{\Sigma_{g,0}}{t_{p,g}}, \quad$ where $\Sigma_{g,0} = 10.4\ \mathrm{M_\odot\,pc^{-2}}$ and $t_{p,g} = 4.5\ \mathrm{Gyr}$ $\sigma_{W,g}(\tau) = s_g \sigma_{W,s}(\tau), \quad s_g = 0.65$
Thick disk
$\Sigma_{t,0} = 5.6\ \mathrm{M_\odot\,pc^{-2}}, \quad \sigma_{t,0} = 45.4\ \mathrm{km\,s^{-1}}$
DM halo
$\Sigma_{h,0} = 59.9\ \mathrm{M_\odot\,pc^{-2}}, \quad \sigma_{h,0} = 140\ \mathrm{km\,s^{-1}}$

Table 2.1: Input functions and parameters of the local JJ model.

disk parameters were also improved. Its local surface density was fixed to 18% of the surface density of the thin disk, and its scale height was found to be $h_t = 800$ pc.

We note that though numerous recent studies indicate that the thick disk might be more complex than we assume here (see Section 1.3.1), the topic is still under debate and our simple treatment of the thick disk remains in agreement with observational constrains (thick disk is old, dynamically heated, and metal-poor). We are also consistent with the two-infall chemical models from Grisoni et al. (2017, 2018) who report a short, ~ 0.1 Gyr, time scale of the thick

disk formation. In order to disentangle the thin and thick disks in a robust way, we need to test our model against the extended data sample after the model will be generalised to the Galactocentric distances other than solar. For now we only allow thick disk to have a scatter in metallicity (as we did for testing the model against the Gaia DR2 data, see Section 3.5). The further possible improvements are postponed to the stage of the full extension of the model, which will also include the detailed chemical evolution allowing to study different Galactic populations in the chemical abundance plane.

Thus, by studying the solar neighbourhood we arrived at the monotonous AVR and AMR, the decreasing SFR with a peak at old ages, and a four-slope broken power-law IMF for the thin disk, as well as the thick disk of single age, scale height and vertical velocity dispersion. Following the convention established in Paper I-Paper III, we address this best set of parameters as our fiducial model and use it to study the local stellar populations (Chapter 3).

As discussed in Gao et al. (2013), the median model-to-data deviations over the Hess diagrams constructed with the SDSS apparent magnitudes and colours towards the north Galactic pole are 5.6% for the JJ model, but 26% for TRILEGAL and 20-53% for the old Besançon model (Robin et al., 2003). In view of this result, the JJ model looks as a promising tool to study the thin disk populations even when compared to such sophisticated Galactic models as BGM; the JJ model has a narrower range of free parameters, which then can be pinned down easier, and allows a detailed description of the thin-disk populations (for comparison, in the BGM thin disk is represented by only six isothermal components).

In the long term, the development of the JJ model is focused on its robust extension to the Galactocentric distances beyond solar. The above-mentioned code Chempy is a useful tool developed for testing chemical evolution scenarios of the Galaxy. Constraining Chempy parameters with high-quality spectroscopic data and combining it with the radially dependent SFR and AVR will be the road to build a global Milky Way disk model.

The first steps to the radial extension of the JJ model were already presented in Just and Rybizki (2016) and Just et al. (2018), while in Koutsouridou (2017) the topic has been discussed more extensively. In this chapter we discuss the key aspects of the present-day version of the extended JJ model and describe their practical implementation in the Python code. Finally, we investigate the predicted properties of the Galactic disk and put our findings in context of the most recent knowledge of the disk structure.

2.2 Generalisation of the JJ model

For a start, we set a range of Galactocentric distances to be considered in this chapter. The outer boundary is set to 12 kpc, and this choice is governed by several reasons. First, the stellar density drops quickly towards the outskirts of the disk; together with increase of heliocentric distance to these regions, this leads to much less abundant data available for the stellar populations in the outer disk in comparison to the solar neighbourhood. This implies that the parameters of the model derived from the calibration against such data may suffer from biases. Second, the outer disk rests in the gravitational potential well which is shallower in comparison to the inner Galaxy, and therefore the outer disk is more sensitive to external perturbations from encounters with satellites. Thus, our assumption about axisymmetery and dynamic equilibrium may be violated in this region. Taking this into account, we choose to remain within the moderate Galactocentric distances. The inner boundary is set to 4 kpc as at smaller Galactocentric

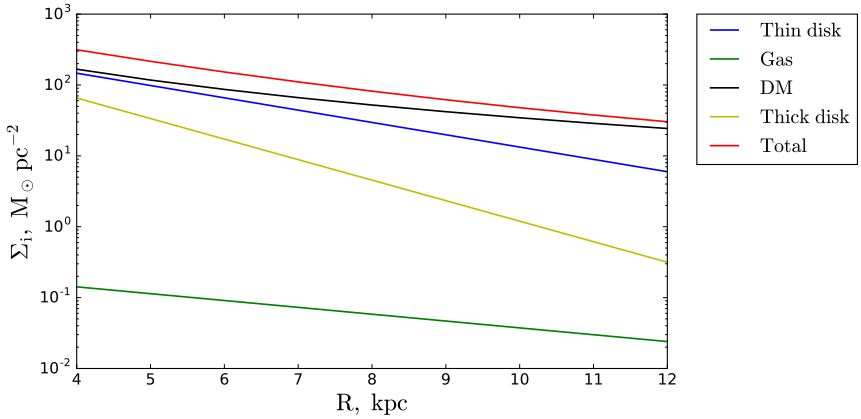

Figure 2.1: Assumed radial surface density profiles of the Galactic components as given by Eqs. 2.5-2.6.

distances kinematics of stars changes significantly being under the influence of the bar, such that the model assumptions about disk axisymmetry and the dynamic equilibrium are not valid here as well. So our further discussion of the extended JJ model will refer to the Galactocentric distances from 4 to 12 kpc and use a step of 1 kpc.

In order to generalise the local JJ model, we make several assumptions about the structure and properties of the Galaxy:

- We allow three of four input functions which govern the thin-disk evolution to vary with Galacticentric distance, so they read: SFR(R,t), AVR(R,t), AMR(R,t). The IMF is assumed to be universal, i.e., not changing with time or from place to place, which is consistent with the reported constancy of the Galactic IMF (Offner et al., 2014; Krumholz, 2014).
- The radial surface density profiles of the gas, thin and thick disks are taken to be exponential given by

$$\Sigma_i(R) = \Sigma_{i,0} \exp \frac{R - R_0}{R_{d,i}}, \tag{2.5}$$

  where the assumed distance to GC is $R_0 = 8$ kpc and the radial scale lengths $R_{d,i}$ are 2.5 kpc, 1.5 kpc, and 4.5 kpc, respectively. The DM halo in a form of isothermal sphere corresponds to a power-law radial density profile when taken in a thin-disk approximation:

$$\Sigma_h(R,z) = \Sigma_{h,0} \frac{R_0^2}{R^2 + z^2} \approx \Sigma_{h,0} \frac{R_0^2}{R^2}. \tag{2.6}$$

  The corresponding radial surface density profiles of the Galactic components are shown in Fig. 2.1.
- The thicknesses of both thin and thick disks are assumed to be constant; this is supported by studies on light distribution of edge-on galaxies (van der Kruit and Searle, 1981; Bizyaev and Mitronova, 2002).
- Different radial annuli are treated as independent, the radial gas flows and stellar migration are not allowed in the model. This is most shaky assumption, as the intensity of the radial migration across the disk remains poorly understood.

2.3 Structure of the code

In order to implement the assumptions listed above, a new Python code has been developed. Its structure is illustrated by a scheme in Fig. 2.2. Roughly the calculation process can be split in two steps: a pre-run, which builds the local model, and a main run, during which the local model parameters are extrapolated to other distances. Both of the runs include an optimisation of the integration limit ϕ_{max} as a first step, we therefore start the review of the code from this routine.

Optimisation of the integration limit ϕ_{max}. In our model the normalised vertical potential $\phi(\zeta)$ is obtained by numerical integration of Eq. 2.1 with a subsequent inversion of the function $\zeta(\phi)$. As we work in the thin-disk approximation, we do not attempt to go further than 2 kpc away from the Galactic plane, or $\zeta_{max} \approx 5$. Correspondingly, there is a maximum value of the normalised gravitational potential ϕ_{max} matching this maximum height. In order to make the code efficient and not to perform integration for the heights we are not interested in, we need to set a realistic value of ϕ_{max} before solving the Poisson's equation. Obviously, ϕ_{max} is a function of Galactocentric distance, so we optimise this limit of integration at each R.

In the beginning, a large initial value of ϕ_{max} is assumed, usually set to 15. Then Poisson's equation is solved with the input parameters for a given Galactocentric distance under several crude assumptions. The surface densities $\Sigma_i(R)$ are prescribed by the assumed radial profiles from Eqs. 2.5-2.6; in case of the gas and thin disk they enter in a form of constant

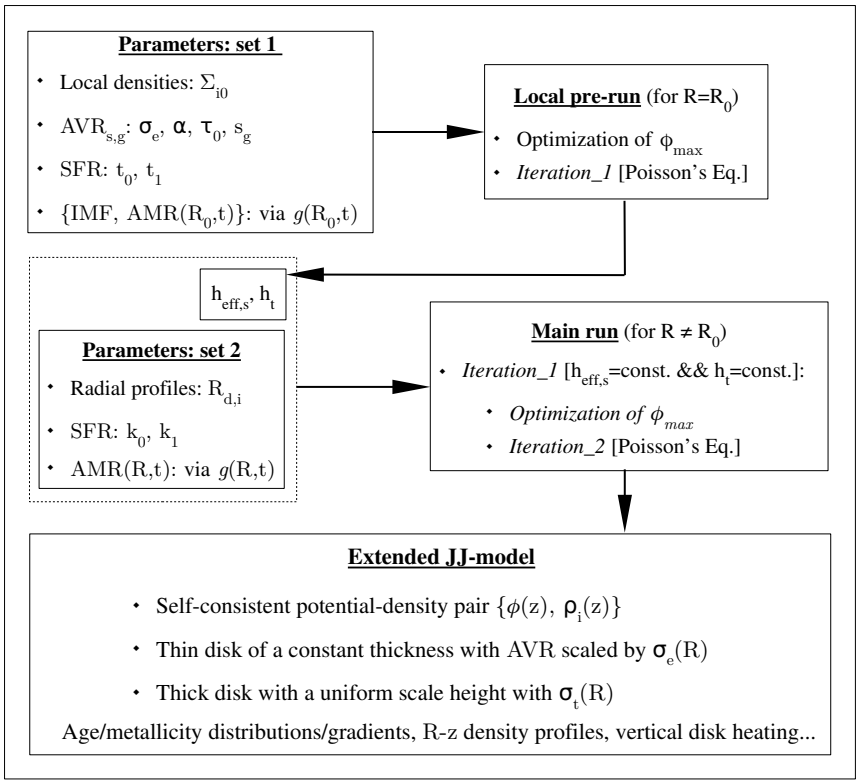

Figure 2.2: Structure of the code developed for extending the local JJ model to the Galactocentric distances R = 4-12 kpc.

GFR and SFR of the prescribed shape (see Eq. 2.3 and also below). The scale heights of the thin-disk and gas subpopulations are roughly assumed to be 400 pc and 100 pc for all ages. For the velocity dispersions and scale heights of the thick disk and the DM halo the local values are used. Additionally, in order to roughly imitate vertical heating of the thin disk and gas, the AVR is scaled with σ_e factor according to an empirical formula:

$$\sigma_e(R) = \sigma_e(R_0) + 3.125(R_0 - R).$$

When the Poisson's equation is solved with this setup, the value ζ'_{max} corresponding to a chosen ϕ_{max} is derived which is then used to re-define ϕ_{max}. After several iterations this procedure converges to give a reasonable value of the integration limit for Eq. 2.1.

Local pre-run of the code. This run of the code is only preparative; it builds the local disk model with parameters and input functions as given in Table 2.1. After ϕ_{max} is optimised, Eq. 2.1 is solved iteratively with the given input parameters (parameter *set_1* in Fig. 2.2). Among the output values are the effective thickness of the thin disk and the thick-disk scale height, which are then used as input parameters for the main run of the code.

Main run of the code. In order to extend the model to the distances of 4-12 kpc, the input functions SFR(R,t), AVR(R,t) and AMR(R,t) must be specified (parameter *set_2* in Fig. 2.2). Our recipe for the SFR(R,t) is to allow its parameters t_0 and t_1 to be power laws of Galactocentric distance:

$$t_0(R) = t_0(R_0) + (R/R_0)^{k_0}; \quad t_1(R) = t_1(R_0) + (R/R_0)^{k_1}. \tag{2.7}$$

Two new parameters k_0 and k_1 control the radial change of the SFR shape. We choose their values in such a way that SFR is peaked at older ages for the inner disk which mimics the inside-out disk growth process. The SFR and GFR functions are then calibrated with the prescribed surface densities $\Sigma_s(R)$ and $\Sigma_g(R)$ (Eq. 2.5, also see Table 2.1).

The AVR(R,t) function is assumed to have a constant shape over the range of Galactocentric distances under consideration, but is allowed to be scaled by the parameter $\sigma_e(R)$. The value of $\sigma_e(R)$ is constrained iteratively: it is optimised to fulfill the assumption about the constancy of the thin-disk thickness. The scaling factor s_g that determines the vertical heating of the gas is kept constant and equal to its local value (Table 2.1). By analogy, the vertical velocity dispersion of the thick disk is also iterated, such that its scale height remains constant at all R. The velocity dispersion of the DM halo is assumed to be independent of Galactocentric distance and equal to the value adopted in the fiducial local model.

The third input function, an enrichment law AMR(R,t), is not so easily determined. As we show in Section 2.5, one can derive it from the observed metallicity distribution function of the disk, though this analysis is itself model-dependent. On the other hand, the dynamical and chemical disk evolutions are only loosely linked to each other: the AMR function, as well as the IMF, enters our calculation only through the mass loss function $g(R,t)$ and, as a result, it has much weaker influence on the predicted disk structure than the SFR and AVR functions. On the other hand, we are highly interested in the radial dependence of the AMR law as this function can be used to translate the properties of our mono-age disk populations to the space of metallicity which is, unlike ages, is a directly measured quantity. Thus, in order to solve the problem, we run the full simulation two times. Firstly, we assume the local enrichment history, AMR(R_0,t), at all distances; this also corresponds to the mass loss independent on R. Then,

basing on the extended disk model and metallicity distributions of the red clump (RC) stars from the APOGEE survey (Section 2.5.1), we define the distance-dependent enrichment law. After this we rerun our code to improve the extended disk model by accounting for the mass loss function distance dependence.

2.4 Model predictions

In order to demonstrate the sensitivity of our model to the input parameters of the SFR function, we investigate the predicted disk structure as inferred with the two sets of (k_0, k_1) values: $(0.5, 1)$ and $(0, 2)$. At this stage, we use the mass loss function constructed in accordance with the AMR at the solar radius and ignore its variation with Galactocentric distance due to the radial dependence of the chemical enrichment speed and intensity. In order to refer to these two models we use short notations "k-0.5-1" and "k-0-2", respectively. Two sets of normalised SFR functions are shown at the top row of Fig. 2.3 with a colour coding corresponding to different Galactocentric distances and the vertical dashed lines marking positions of the SFR peaks. The models differ by the variation of the time scale and intensity of star formation across the disk. Both models have almost flat SFR for the outer disk, while the shapes of the functions are significantly different for the inner disk region. The middle panel of Fig. 2.3 shows the vertical heating of the thin disk as obtained for two models. As expected, the vertical heating increases with decrease of distance, which is a consequence of the assumed constancy of the disk effective thickness. The model "k-0.5-1" predicts in general stronger variation of the vertical heating with Galactocentric distance. The bottom row of Fig. 2.3 shows thin-disk age distributions calculated for the near-plane mass at $|z| < 400$ pc with the use of derived vertical gravitational potential, thin-disk scale heights, the AVR and SFR. The shape of the age distributions is heavily influenced by the assumed SFR, though it is also sensitive to the distance from the midplane. The mean age at each distance corresponds to a vertical dashed line illustrating a non-linear age variation across the disk; in case of the model "k-0-2" the age gradient is more pronounced. Before proceeding to more detailed investigation of the disk structure, we constrain the AMR basing on the inferences from this first code run.

2.5 AMR as constrained by the APOGEE data

Tracing the overall increase of metallicity with stellar age is not a trivial task. Firstly, high-quality spectroscopic data with the known distances are required. Secondly, the reconstructed AMR is intrinsically sensitive to such underlying assumptions as the SFR, IMF and stellar radial migration. The approach we use here has been presented in Gier (2016) and applied to the same APOGEE RC sample (see below) in Koutsouridou (2017). Here we use an improved methodology which allows us to constrain the radial variation of the AMR in a more robust way.

2.5.1 Data sample

We use the RC catalogue consisting of 29, 502 stars built on the basis of the fourteenth data release (DR14) of the APOGEE survey. APOGEE is a high-resolution (R$\sim$ 22, 500) NIR spectroscopic survey probing the structure of the Galactic disk and bulge. The construction of the

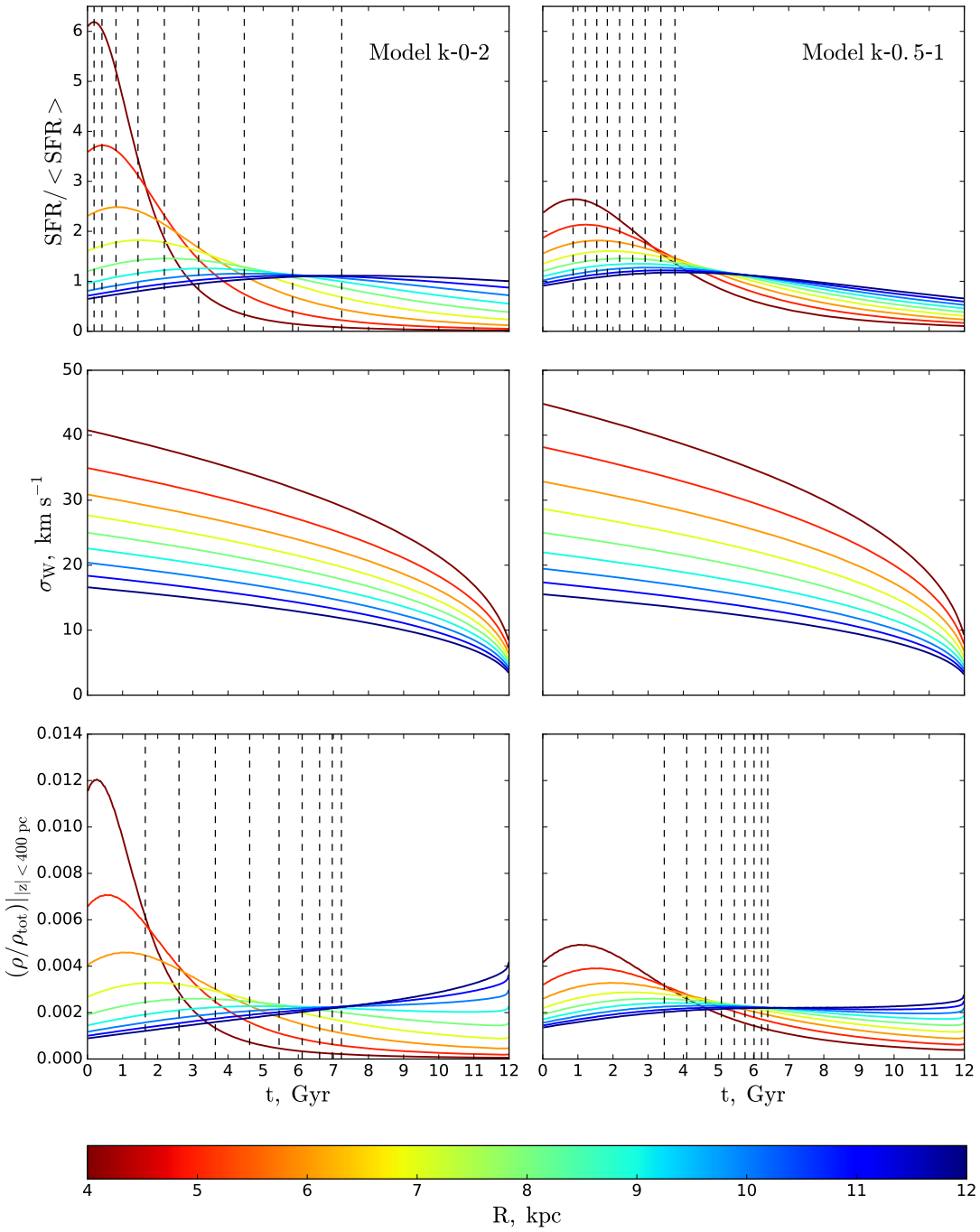

Figure 2.3: Input and predictions of the extended JJ model. Two columns correspond to different choices of the SFR parameters k_0 and k_1. *Top.* Assumed normalised SFR as functions of Galactocentric distance. The vertical dashed lines show positions of the SFR peaks. *Middle.* Thin disk AVR as predicted by the extended JJ model with the assumed SFR and ander the assumption of the constant thin disk thickness. *Bottom.* Thin disk age distributions for $|z| < 400$ pc. Vertical dashed lines correspond to the mean age at a given Galactocentric distance.

RC subsample from the APOGEE data was presented in Bovy et al. (2014), and since then the RC catalogue was regularly updated. Being bright standard candles, the RC stars allow accurate distance determination: the typical systematic and random errors reported in Bovy et al. (2014) are less than $\sim 2\%$ and $\sim 5\%$, respectively. According to Nidever et al. (2014), possible biases

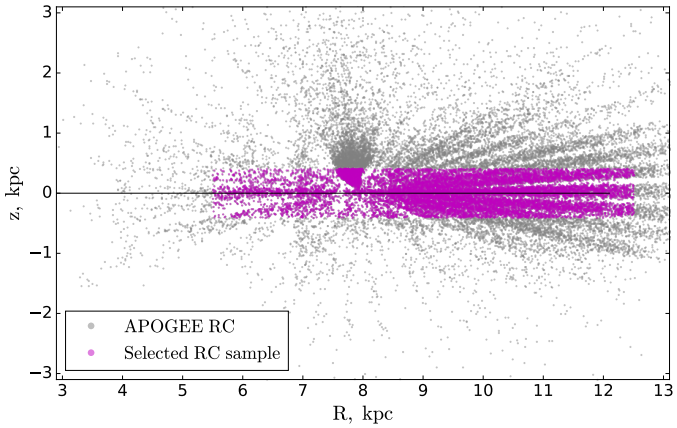

Figure 2.4: Spatial distribution in the R-z plane of the full APOGEE RC data set (shown in grey) and our selected RC sample (magenta markers).

introduced by the incompleteness of the RC catalogue are effectively removed when the abundance information is used in combination with distance, or within small spatial zones. This implies that we can avoid complication of our analysis and ignore the sample selection function, as for our purposes we bin the data into equal-width Galactic annuli. We select our sample by applying cuts in Galactocentric distances, $5.5\,\mathrm{kpc} < R < 12.5\,\mathrm{kpc}$, and distance from the midplane, $|z| < 400$ pc. By the first criteria we avoid the inner- and outermost disk regions, where the data are not abundant enough, while the second cut allows to minimise contamination from the thick disk. The final RC sample contains 15, 560 stars. Fig. 2.4 shows the full APOGEE DR14 RC data set (grey) and our RC sample (magenta) in the Galactic cylindrical coordinates R and z.

2.5.2 Methodology

The approach we use here is based on a direct linking of the observed metallicity distributions to the modelled ages; this allows us to reconstruct the enrichment history at each given Galactocentric radius R.

Observed cumulative metallicity distributions. We bin our data sample in seven distance bins of 1 kpc width in the range of Galactocentric distances 5.5-12.5 kpc. The cumulative metallicity distributions for these bins are plotted at the left panel of Fig. 2.5 (solid colour-coded curves). As it was shown in Gier (2016), the shape of cumulative metallicity distribution at the metal-rich end can be described well in terms of the convolution of a true physical component with a Gaussian core with a dispersion of ~ 0.1 dex; this Gaussian core represents observational and systematic errors. In this respect, the most metal-rich parts of the cumulative distributions at each distance bin do not fit into the framework of our analysis for two reasons: on one hand, high values of metallicity, $[\mathrm{Fe/H}] \gtrsim 0.4$, may suffer from systematic biases, while on the other hand, the most metal-rich stars in at a given distance are associated with the stellar populations migrated inside-out. The error model, as well as the radial migration, are not included into this analysis, so we remove the metal-rich parts of the cumulative metallicity distributions by extrapolating their linear parts to higher metallicities (dashed lines on the left panel of Fig. 2.5).

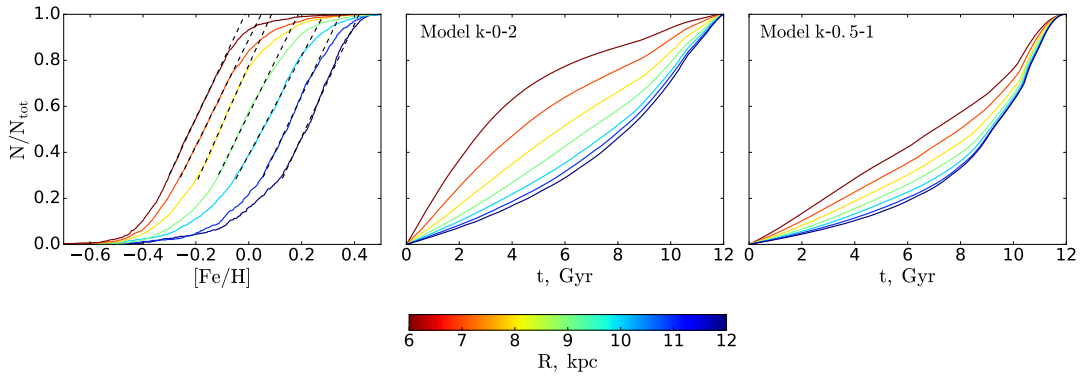

Figure 2.5: *Left.* Normalised cumulative metallicity distributions for the APOGEE RC sample as calculated in seven distance bins. The overplotted dashed lines show the extrapolation of linear parts of the distributions used in order to clean the data from the stars potentially affected by the radial migration. *Middle and right.* Normalised cumulative age distributions of the modelled RC populations as predicted by the two tested disk models.

Simulated cumulative age distributions. From the other side, we simulate the RC sample using our extended JJ model and a set of isochrones from the PAdova and TRieste Stellar Evolution Code (PARSEC, Bressan et al., 2012, Marigo et al., 2017). We use 56 isochrones covering metallicity range of $Z = 0.0015$-0.04 with a step of

$$\Delta Z = \begin{cases} 0.0005, & 0.0015 \leq Z \leq 0.018 \\ 0.001, & 0.018 < Z \leq 0.04 \end{cases}$$

which corresponds to [Fe/H] ≈ -1-0.47. The ages of isochrones are given in logarithmic range $\log(\tau/\mathrm{yr}) = 7$-$10.08$ with a step of 0.02. The range of stellar masses covered by PARSEC isochrones is 0.06-120 $M_\odot$, from which we select the range of 0.08-100 $M_\odot$ as prescribed by the model IMF (see Table 2.1).

Assuming the local AMR for all distances as a zero-order approximation, to each age-metallicity pair from the model[17] we assign a closest isochrone. The resulting number of the stellar assemblies generated for each R and characterised by the same ages, metallicities, and initial stellar masses is $\sim 1.6 \cdot 10^5$. For each stellar assembly j a surface number density N^Σ is calculated by weighting the SFR(R,t) with the IMF. At this step, we have a set of tables where the mock stellar assemblies are listed, with their surface densities known. In order to separate the RC sample, we apply the cuts corresponding to the selection criteria used for construction of the APOGEE RC catalogue and presented in Bovy et al. (2014):

$$4250 \text{ K} < T_{\rm eff} < 5250 \text{ K};$$
$$\log g < 2.9 \ \& \ \log g < 0.018(T_{\rm eff} + 382.5[\mathrm{Fe/H}] - 4607) + 2.5.$$

[17] At this point, it is useful to define a new notation in order to avoid confusion in the future. From here on we keep the term 'subpopulation' to refer to the thin-disk mono-age isothermal subpopulations. For the additional splitting in metallicity-mass parameter space we introduce the term 'stellar assembly'.

Table 2.2: Coefficients of the linear fit of the AMR parameters: $\{[\mathrm{Fe/H}]_\mathrm{p}, r\} = a_0 + a_1 R[\mathrm{kpc}]$.

	Model k-0.5-1		Model k-0-2	
	a_0	a_1	a_0	a_1
$[\mathrm{Fe/H}]_p$	0.08	-0.02	0.07	-0.09
r	-0.09	0.92	-0.11	1.05

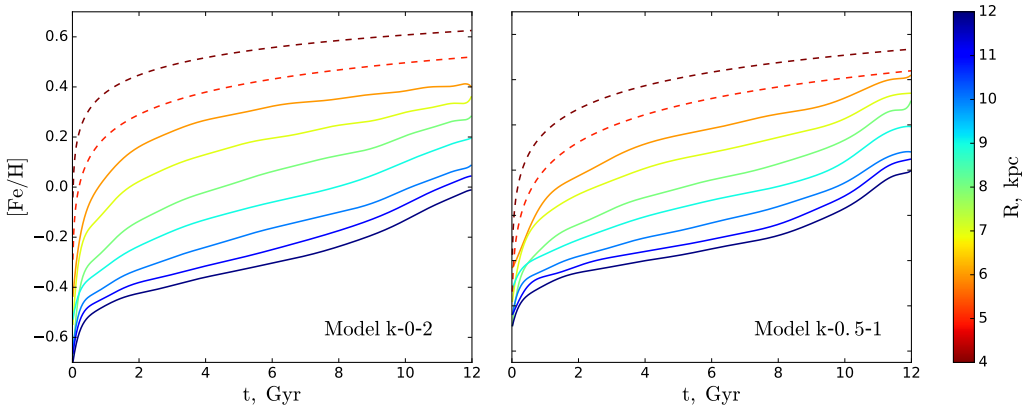

Figure 2.6: Reconstructed AMR(R,t) function as obtained in consistency with the APOGEE RC sample and the extended JJ model (solid curves). The dashed curves show the enrichment law as extrapolated to Galactocentric distances of 4-5 kpc.

Then for a fixed R the predicted number of RC stars of each age is expressed by the equation:

$$N(\tau) = \sum_{j}^{N_\tau} \left[\frac{N_j^\Sigma(\tau)}{2h_s(\tau)} \sum_{0}^{z_{max}} \exp\left\{ -\Phi(z)/\sigma^2_{W,s}(\tau) \right\} \right], \tag{2.8}$$

where index j corresponds to different stellar assemblies of the same age and $z_{max} = 400$ pc.

Reconstruction of the AMR(R,t) law. In order to reconstruct the AMR(R,t) function, we assume that the chemical enrichment at each radius proceeded in the form of a monotonous increase of iron abundance with age. Then we compare the relative stellar numbers N/N_{tot} in the observed cumulative metallicity distributions and the modelled age distributions, such that we read out from them the corresponding values of [Fe/H] and τ. As a result, the radially dependent chemical enrichment law is obtained. This derivation of the AMR(R,t) function is done in an iterative way, such that a newly constrained AMR(R,t) law is used to simulate more robust age distributions during the next iteration. The procedure converges after two or three runs. The resulting cumulative age distributions as predicted by the two versions of the extended JJ model are shown at the middle and right panels of Fig. 2.5. Two model-based sets of AMR(R,t) are plotted in Fig. 2.6 (solid curves). In order to extrapolate our findings to Galactocentric distances of 4-5 kpc, we fit the obtained curves with a functional form of the local AMR from Table 2.1 assuming $[\mathrm{Fe/H}]_p$ and r as free parameters and setting the $[\mathrm{Fe/H}]_0$ value changing linearly from -0.8 to -0.55 from the inner to the outer disk. By linear extrapolation of the parameters $([\mathrm{Fe/H}]_\mathrm{p}, r)$ to the inner disk, we calculate the enrichment laws for the two innermost distance bins (parameters of the linear fit of $[\mathrm{Fe/H}]_p$(R) and r(R) are given in Table 2.2). However, we note that the chosen fit function cannot reproduce a non-linear increase of metallicity at young ages (see the right panel of Fig. 2.6); thus, the enrichment laws of the inner disk might be biased.

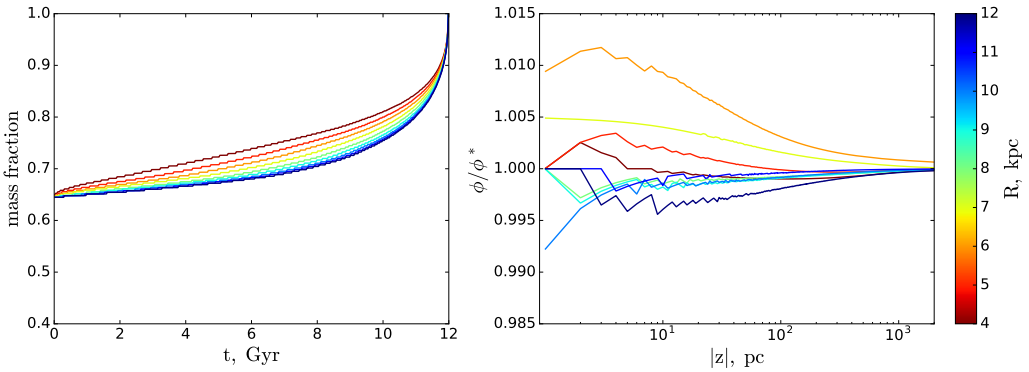

Figure 2.7: *Left.* Radially dependent mass loss function as calculated with the code Chempy for the AMR(R,t) based on the model "k-0.5-1". *Right.* Ratio of the vertical gravitational potentials calculated with the constant and radially dependent mass loss functions for the same model.

2.5.3 Mono-age and mono-abundance stellar populations

With the AMR function is now known for different distances, we derive the mass loss function for all R and then perform an additional run of the code to bring our modelled gravitational potential in consistency with the chemical evolution of the disk. The new mass loss function based on our broken power-law IMF and the AMR derived on basis of the model "k-0.5-1" is shown at the left panel of Fig. 2.7. The right panel of this figure shows the ratio of the vertical gravitational potentials obtained in the runs with the constant (Section 2.4) and variable mass loss function. The largest changes are seen near the Galactic plane, but the absolute value of this difference is only $\sim 1\%$.

At this point, we can characterise matter distribution across the disk by looking at individual mono-age and mono-abundance populations (MAPs). The top panel of Fig. 2.8 displays scale height as a function of Galactocentric distance for both mono-age populations and MAPs. The colour-coded curves show every 20^{th} of our 480 isothermal mono-age thin disk subpopulations; this corresponds to age step of 0.5 Gyr. Both models predict flaring of the mono-age populations increasing with stellar age. The rate of this flaring is essentially zero for the youngest subpopulations and is 20 pc kpc^{-1} and 26 pc kpc^{-1} for the oldest stars as predicted by the models "k-0.5-1" and "k-0-2", respectively. The effect of flaring is also predicted by the numerical simulations and can be attributed to many different factors including radial migration caused by the spiral pattern, impart of mergers, or misaligned gas infall (Minchev et al., 2015). However, stellar ages are not derived easily, so mono-age populations are not very instrumental in studying the structure of the disk, instead the chemical abundances can be used to construct MAPs. The black dashed lines overplotted on top of the colour-coded mono-age populations mark contours of constant metallicity and illustrate the radial change in scale heights of four MAPs with metallicities of $[\text{Fe/H}] = -0.4, -0.2, 0, +0.2$. Due to the fact that the same metallicity may correspond to different ages at different R, the scale height profiles of MAPs demonstrate different behaviour in comparison to the mono-age populations. As one can read out from Figs. 2.8 and 2.6, the metal-poor MAPs are also very close to being mono-age populations. On the other hand, the metal-rich MAPs are composed from a mixture of different ages. The mean age (weighted with surface density) for the MAP at [Fe/H] = −0.4 is $\sim$ 11.6 Gyr or 11.8 Gyr for the "k-0.5-1" and "k-0-2" models, respectively. At the metal-rich end, [Fe/H] = +0.2, the mean MAP age decreases to $\sim$ 6.9 Gyr and $\sim$ 7.3 Gyr, depending

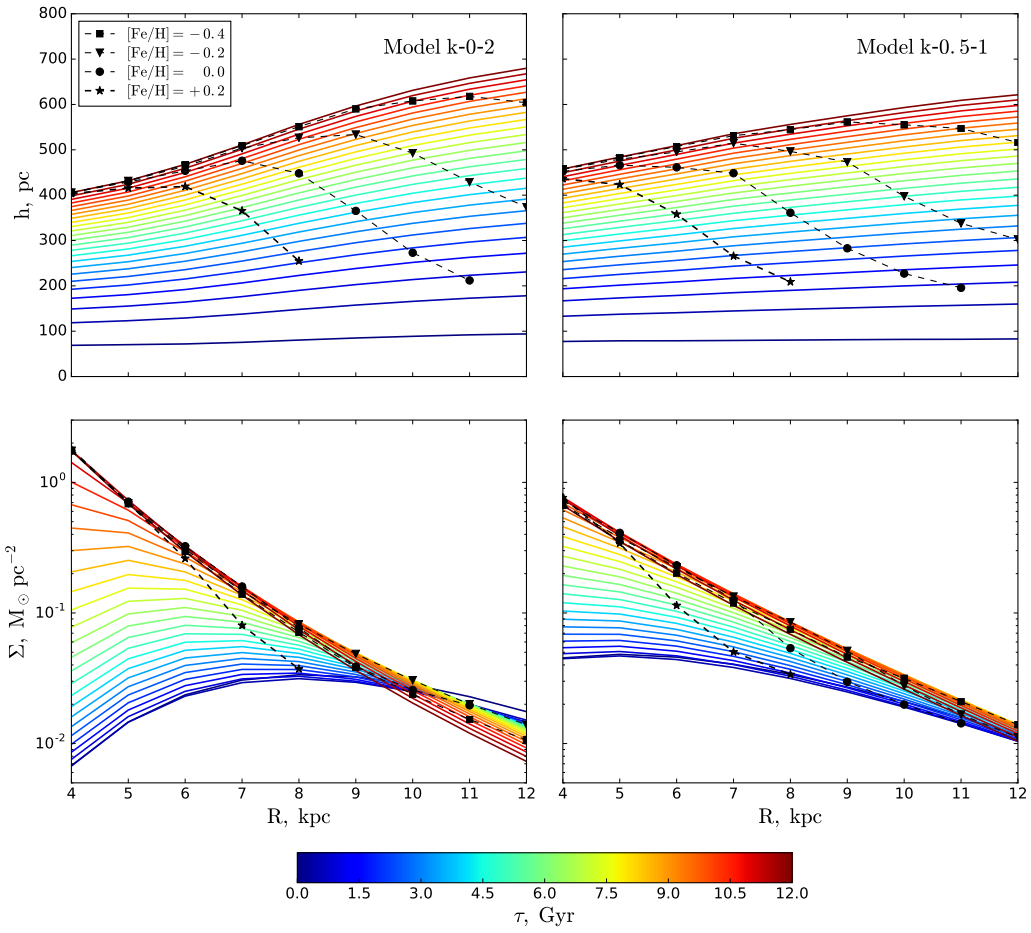

Figure 2.8: *Top row.* Radial variation of the 24 mono-age populations as predicted by the models "k-0.5-1" and "k-0-2" (colour-coded curves). The dashed lines with different markers correspond to the four MAPs with metallicities of $-0.4, -0.2, 0., +0.2$. *Bottom row.* Radial surface density profiles of the same mono-age populations and MAPs.

on the model. The corresponding values of age dispersion are ~ 0.6 Gyr and ~ 0.24 Gyr for [Fe/H] = −0.4 which increases to ~ 1.85 Gyr and ~ 1.6 Gyr at [Fe/H] = +0.2. The MAPs have negative radial age gradient; the value of this gradient ranges from ~ 0.48 Gyr kpc^{-1} or ~ 0.33 Gyr kpc^{-1} at [Fe/H] = −0.4 to as large as ~ 1.97 Gyr kpc^{-1} or ~ 1.9 Gyr kpc^{-1} for the MAP with metallicity [Fe/H] = +0.2. The subject of the relationship between the mono-age populations and MAPs was deeply investigated in Minchev et al. (2017) on basis of a chemo-dynamic model of the Milky Way-like galaxy with inside-out growing disk. For the MAP of [Fe/H] = −0.3 and [α/Fe] = +0.1, the authors found negative age gradient of ~ 0.45 Gyr kpc^{-1} with an increase of its absolute value for higher metallicities and lower [α/Fe]; they also report an inversion to a positive age slope which we do not observe in our model. The described complexity of MAPs in terms of age composition leads to a suppression of flaring starting from some R_{peak} which increases with metallicity decrease.

The bottom row of Fig. 2.8 shows the radial surface densities for the same set of mono-age populations and the four MAPs. The radial surface density profiles of mono-age populations predicted by the model "k-0-2" can be characterised by a peak distance and a roughly

exponential decrease in both directions from the peak. The peak position moves outwards for smaller ages, which is a natural outcome of the input SFR with a maximum of star formation shifting to younger ages with increase of Galactocentric distance. In case of the model "k-0.5-1", which suggests less prominent inside-out growth of the disk, the surface density profiles can be well-described by a single exponential. The surface density of MAPs is also exponential for both models. In case of low metallicities, when MAP is also a mono-age population, it follows the surface density profile of a corresponding age. For [Fe/H] $\gtrsim -0.1$ the slope of MAPs becomes larger than the steepest slope of the oldest population, which is caused by the discussed negative age gradient along each MAP. As a result, MAPs of near-solar and super-solar metallicities are strongly centrally concentrated with radial scale length changing from ~ 2.1 kpc or ~ 1.6 kpc for [Fe/H] = -0.4 to 1.2 kpc or 1 kpc for [Fe/H] = $+0.2$ for the models "k-0.5-1" and "k-0-2", respectively. However, if we account for the width of metallicity bins, the corresponding scale lengths increase to fall into a better agreement with observations.

The left panel of Fig. 2.9 displays the surface density profiles of four metallicity bins of 0.1 dex width. The dashed and solid lines correspond to the models "k-0.5-1" and "k-0-2", respectively. An extensive study of the observed spatial distribution of MAPs based on the APOGEE RC sample has been recently presented in Bovy et al. (2016b). A qualitative comparison between MAPs properties reported by the authors and our predictions allows us to conclude that our model, characterised by a prescribed inside-out disk formation and a constant disk thickness, is able to match most of the observational trends of the thin-disk MAPs. The low-α APOGEE MAPs have double-exponential surface density profiles characterised by the peak distance shifting inwards with increase in metallicity. Though the radial resolution of our surface density profiles in Fig. 2.9 is quite rough, the presence of peaks is clearly visible; they move to smaller Galactocentric distances for higher metallicities. Their positions in case of model "k-0-2" are comparable to the observed values: for metallicity bins centered at [Fe/H] = $[-0.4, -0.2, 0, +0.2]$ the peak positions lie at $R_{\rm peak} \approx [> 12, 10, 8, 5]$ kpc (the corresponding values from Bovy et al. (2016b) are $R_{\rm peak} \approx [10.5, 10, 8, 6]$ kpc). Our outer scale length of the MAP with [Fe/H] = $+0.2$ is ~ 1.7 kpc, which is similar to the corresponding value of ~ 1.5 kpc for the APOGEE RC surface density profile. The inner scale length of the metal-poor MAP of [Fe/H] = -0.4 is, however, shallower in our model being ~ 4.7 kpc in comparison to ~ 2.5 kpc in Bovy et al. (2016b). The predicted scale heights for these metallicity bins behave somewhat similar to the scale heights of individual MAPs in Fig. 2.8. The stars in metallicity bins are dynamically colder in the outer disk, though the model "k-0-2" predicts an increase of dynamical heating up to break distance, and similar behaviour is also reported in (Bovy et al., 2016b). However, MAPs in our models have a much more prominent tendency for thinning with increase of Galactocentric distance than it is observed according to the APOGEE data. As our model is intrinsically highly sensitive to the choice of the SFR, there is a possibility that these discrepancies can be overcame by the appropriate choice of input parameters. On the other side, lack of radial migration in our model may lead to an underestimation of flaring as inward migrators are known to settle closer to the midplane, while the stars migrating outwards vertically expand. However, according to some recent studies, the role of radial migration may be not very important in inducing the disk populations flaring (Vera-Ciro et al., 2016). In either case, with the extended model now built, we can actively explore the parameter space, calibrate the model across the disk with the high-quality astrometric and spectroscopic data, as well as complement it with the code Chempy in order to add a multi-elemental chemical evolution (see also Chapter 6 for the outlook).

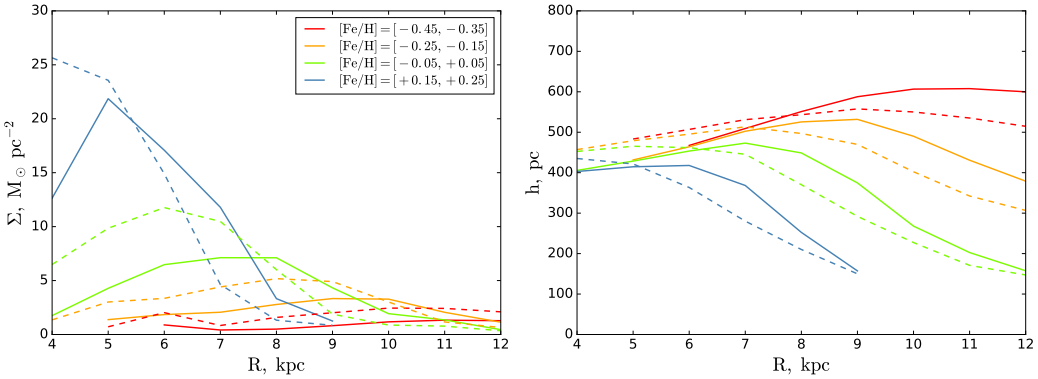

Figure 2.9: Radial variation of the surface density (left) and scale height (right) for the four metallicity bins of 0.1 dex width. The solid and dashed lines correspond to the models "k-0-2" and "k-0.5-1", respectively.

2.6 Summary

In this chapter we presented the JJ model of the Milky Way disk, generalised it for the medium Galactocentric distances and discussed the predictions of the two model instances with the alternative SFR parameters. Here we summarise our results.

- We build the disk model in a range of Galactocentric distances of 4-12 kpc with a 1 kpc step. We assume the radially dependent SFR with a peak of star formation shifting towards younger ages with increase of Galactocentric distance in order to mimic the effect of inside-out disk growth. We also assume a constant thickness of the thin and thick disks, which allows a self-consistent determination of the AVR at all radii.
- Basing on the assumed disk model constructed with a constant mass loss function, we reconstruct the enrichment history of the thin disk in a range of Galactocentric distances 6-12 kpc from the APOGEE RC sample. This observationally constrained AMR is then used to allow a radial variation of the mass loss function in order to bring the chemical and dynamical parts of the model into the full consistency.
- The spatial disk structure is studied via mono-age populations and MAPs. The flaring of mono-age populations, also predicted by many numerical simulations, is reproduced as a natural outcome of the assumed inside-out disk growth scenario and a constancy of the disk thickness. We also show that the relation between mono-age populations and MAPs is not straightforward, such that only metal-poor MAPs may be also assumed as mono-age populations, while with the increase of metallicity the age range of MAPs grows. The model is able to reproduce general trends in the radial dependence of the surface density profiles and scale heights of the metallicity bins of 0.1 dex width.
- The next step, after this first insight into the properties of a global disk model, will include in-depth investigation of the model parameter space, as well as its calibration against photometric and spectroscopic data.

Chapter 3

Testing the local JJ model with the Gaia data[18]

3.1 Introduction

In this chapter we test the JJ model locally with the high-quality astrometric data from the TGAS sub-catalogue of the Gaia DR1 and the radial velocities from the fifth data release of the RAVE survey (DR5, Kunder et al., 2017). As more than one billion stars with high-precision astrometry of the Gaia DR2 have recently become available (published on 25 April, 2018; Gaia Collaboration et al., 2018), the impact of Gaia DR2 on our results is also discussed.

Though the JJ model has already been tested and validated, up to now only the MS populations were studied in details (Paper I; Paper II). In Paper III the full stellar evolution was included for the first time; the mock sample was constructed with seven embedded magnitude-complete spheres with radii up to 200 pc. In this chapter we take another step forward and test the model predictions in the solar cylinder with a radius of 300 pc and going up to 1 kpc away from the Galactic plane, with the full stellar evolution included. In this extended volume we study the vertical gradients in the stellar population densities, investigate Hess diagrams, and also the vertical kinematics of the sample.

The ideal way to test a Galactic model would be to take a complete sample and compare the distributions of the observed and modelled stars in parameter space. Of course, this case never occurs as every Galactic survey has its limitations in magnitudes and/or distances, and this is quite often accompanied by rather special criteria for target selection. However, one may construct a sample that is close to being complete within some volume or range of magnitudes and simulate these data by applying simple selection criteria to the model. This simple approach was used in Paper III. Unfortunately, the thin-disk TGAS×RAVE sample as defined later in Section 3.2.1 is characterised by a complicated selection function (Section 3.3.5). For this reason, we choose a forward-modelling technique. In order to motivate our choice of this approach additionally, we refer to the problem of distance derivation.

One of the main uncertainties that blur our picture of the Milky Way is associated with the distance determination: for the present-day vast samples the distance estimates are usually derived from photometry and spectroscopy which results in relatively high uncertainties

[18]This chapter is based on the paper Sysoliatina et al. (2018b) (accepted for publication in *A&A*).

(e.g., see Zwitter et al., 2010; Binney et al., 2014). The astrometric parallaxes measured by Gaia improve the situation significantly. However, the derivation of robust distances from the astrometric parallaxes, even as precise as given by Gaia, is still a non-trivial task. One way is to use the Bayesian method in order to assign each star a probability density function (PDF) that contains the full information on its distance from the Sun. A caveat of this approach is that it depends on a prior expressing our independent knowledge on the distribution of stars in space or with respect to other parameters such as colours or chemical abundances. The derived PDF is quite sensitive to the form of the prior when the parallax errors become large. A reasonable choice of the prior may vary for each individual case depending on measured quantites which are taken into account and the survey selection function (Bailer-Jones, 2015). The Bayesian distances were recently determined for the TGAS stars (Astraatmadja and Bailer-Jones, 2016) and for the stars in common between TGAS and RAVE DR5 (McMillan et al., 2018). The alternative and more straightforward way, which we also follow in this chapter, is to compare the data and model directly in parallax space, with the parallax errors properly modelled.

In the framework of the JJ model, we construct the thin-disk stellar populations in the local solar cylinder with the full stellar evolution included. For the sample of mock stellar populations we predict parallaxes as observed in the TGAS×RAVE cross-match, although for the purposes of illustration, the results are presented as a function of a simple distance estimate calculated both in the data and model as the inverse observed parallax. We also account for the reddening with a realistic three-dimensional (3D) extinction model based on the map from Green et al. (2015) and simulate the complicated selection effects.

3.2 Data

3.2.1 TGAS×RAVE thin-disk sample

To study kinematics and spatial distribution of the thin-disk stellar populations, the full six-dimensional (6D) information in the dynamic phase space has to be known for individual stars. The most recent and accurate five astrometric parameters, i.e., positions, proper motions, and parallaxes, are provided in the TGAS catalogue. The astrometric solution was found by combining Gaia measurements of the first 14 months of the mission and information on positions from the *Tycho-2* Catalogue (Høg et al., 2000). Typical errors for the parallaxes and proper motions are ~ 0.3 mas and ~ 0.3 mas yr^{-1}, respectively. TGAS covers the whole sky and contains ~ 2 million stars. However, this data sample alone cannot serve for our purposes as it lacks the radial velocities, which prevents deriving 3D stellar space velocity vectors. This motivated us to complement TGAS with the information from RAVE DR5, where not only accurate radial velocities are provided (typical errors are 1-2 km s^{-1}), but also chemical abundances of six elements as well as photometry from other surveys such as 2MASS and The AAVSO Photometric All-Sky Survey (APASS, Henden et al., 2009; Munari et al., 2014). The total cross-match between TGAS and RAVE contains 257, 288 stars[19]. For these stars we calculate the estimate of heliocentric distance by inverting the TGAS parallaxes, $\tilde{d} = 1/\varpi$[20]. We also transform it to the distance from the Galactic plane $\tilde{z}$. Using the TGAS proper motions and parallaxes as well as

[19]The cross-match between catalogues was performed by the RAVE Collaboration, see https://www.rave-survey.org/downloads

[20] Here and elsewhere in this chapter notations with tilde are used to emphasise that a given quantity is related to the observed distance derived through this simple inversion.

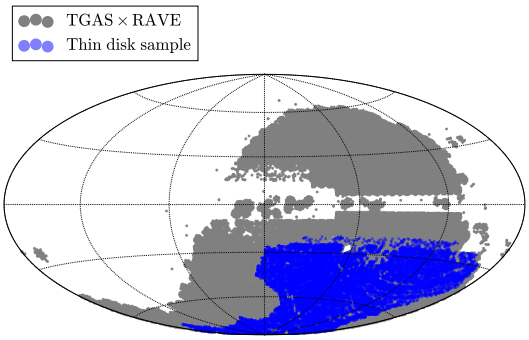

Figure 3.1: Sky coverage of the data in the Galactic coordinates. The full TGAS×RAVE cross-match is shown in grey. The selected thin-disk sample (blue) lies below the Galactic plane; its special shape at $b < -50°$ reflects the Gaia scanning law pattern.

the RAVE radial velocities, we calculate for each star a 3D velocity in Cartesian coordinates (U, V, W). The components of the peculiar velocity of the Sun are chosen as $U_\odot = 11.1$ km s^{-1}, $W_\odot = 7.25$ km s^{-1} (Schönrich et al., 2010), $V_\odot = 4.47$ km s^{-1} (Sysoliatina et al., 2018a). Currently, only the vertical motion of stars is included in the JJ model, such that only the W component of the spatial velocities is used in practice. We also calculate the observational errors $(\Delta U, \Delta V, \Delta W)$ with the help of the TGAS error covariance matrix.

The present-day version of the JJ model contains a detailed recipe for constructing the individual populations of the Galactic thin disk while the other components are added in a simple way (Section 2.1). Thus, to perform a detailed model-to-data comparison, we need to construct a clean thin-disk sample from the data. To do so, we apply the following selection criteria to the TGAS×RAVE cross-match.

1. *Geometry cut.* We select stars with $|b| > 20°$ as the RAVE survey avoids the Galactic plane and the number of observed stars drops quickly at low Galactic latitudes. As later we account for the incompleteness of the selected sample, we consider only a special region on the sky where the selection function of the TGAS catalogue is defined (Bovy, 2017a). We further select only stars below the Galactic plane, $\tilde{z} < 0$, as after all the cuts listed in this Section the fraction of stars left above the midplane is only 6.6% of the total final sample, which can be safely neglected in order to reduce the modelled volume and thus speed up the calculations. We also restrict ourselves to the local cylinder by applying $\tilde{d} \cos b < 300$ pc and $|\tilde{z}| < 1$ kpc. Hereafter we drop modulus in our notation of height and keep in mind that our model is plane-symmetric and we work in the region below the midplane. The number of stars left is 51, 234.
2. *Parallax cut.* About 1.3% of the stars in the TGAS×RAVE cross-match have negative parallaxes because of the impact of large observational errors on astrometric solutions for faint and/or distant stars. As a straightforward conversion $1/\varpi$ is not applicable in this case, we further include only stars with positive parallaxes, $\varpi > 0$. Next we select stars with a relative parallax error smaller than 30%, $\sigma_\varpi/\varpi < 0.3$. After this cut, 50,491 stars remain.
3. *Photometric cut.* We select stars with known (B-V) APASS colour and belonging to the range of visual magnitudes and colours prescribed by the observation windows of the RAVE and Gaia surveys: $7 < I_{\rm DENIS}/{\rm mag} < 13$, $0 < (J - K_s)_{\rm 2MASS}/{\rm mag} < 1$, and $0 < J_{\rm 2MASS}/{\rm mag} < 14$. The remaining sample contains 45, 478 stars.

4. *Quality cut.* We set a lower limit to the signal-to noise ratio (S/N) of the RAVE spectra, $S/N > 30$. We also select only stars with *algo_conv* $\neq 1$, which corresponds to the robust stellar parameters derived from the RAVE spectra. Additionally, we ensure that only stars with reliable values of TGAS astrometric parameters enter our sample. For this we apply the cuts to astrometric excess noise, $\epsilon_i < 1$, and its significance, $D[\epsilon_i] > 2$. At this stage, 34, 501 stars are left.
5. *Abundance cut.* To select the stars that can be identified as thin-disk members in chemical abundance plane, we first apply the cut $4000 < T_{\rm eff}/K < 7000$ as only for this range of effective temperatures the chemical abundances were determined in RAVE (Kunder et al., 2017). Then the cuts [Fe/H] > -0.6, [Mg/Fe] < 0.2 are added. As discussed in Wojno et al. (2016), this is a reasonable criterion for the separation of the thin and thick disks in the RAVE data.

After applying all the selection criteria, we end up with a sample of 19, 746 stars (Fig. 3.1, blue). The numbers of stars given for each stage of the data cleaning should not be interpreted straightforwardly in terms of strictness of the applied criteria. Because of the strong correlations between some of the criteria (e.g., cuts 1 and 2), these values are very sensitive to the order of applying the cuts. Alternatively, all the criteria might be sorted according to the origin of the quantities and the fractions of stars might be estimated that were removed from the initial sample due to the problems with TGAS or RAVE or even entries from TGAS and RAVE together. The corresponding fractions removed from the sample after a simple geometric pre-selection (300-pc radius, $-1000\,{\rm pc} < \tilde{z} < 0\,{\rm pc}$) are 38%, 14.5%, and 22%, respectively.

3.2.2 Data incompleteness

By reducing the TGAS×RAVE cross-match with criteria 1-5, we select a clean thin-disk sample in the local solar cylinder with high quality of the measured quantities. This final sample is not representative for the direct study of the vertical disk structure, however: the TGAS and RAVE catalogues are both incomplete, and the applied cuts make this incompleteness even more severe. To account for this, we thoroughly examine the sources of possible biases in our sample and construct its selection function for further practical use.

The final thin-disk sample clearly contains imprints of the selection functions from both of its parent catalogues. The selection function of the RAVE DR5 depends in general on I-band photometry, $J-K_s$ colour, and position on the sky, $S_{\rm RAVE}(\alpha,\delta,I,J-K_s)$. However, the dependence on colour is relevant only for the low latitudes, $5^\circ < |b| < 25^\circ$ (Kordopatis et al., 2013; Wojno et al., 2017) and is not of primary importance. The selection function of RAVE DR5, which was derived recently in Wojno et al. (2017) and is used in this work, ignores the colour dependence, $S_{\rm RAVE}(\alpha,\delta,I)$. The completeness factor of the RAVE data varies strongly with the line of sight and visual I-band magnitude. The TGAS selection function was investigated in Bovy (2017a) and was found to be quite homogeneous over a large part of the sky. It is defined in terms of 2MASS magnitudes and colours, $S_{\rm TGAS}(\alpha,\delta,J-K_s,J)$. Because of the properties of the Gaia scanning law, the number of observations per star in Gaia DR1 is lowest near the ecliptic, i.e., the measured quantities in the near-ecliptic regions are characterised by high uncertainties and are expected to be most biased by systematic errors. For this reason, near-ecliptic 'bad' regions were excluded from the analysis in Bovy (2017a), such that the TGAS selection function is not defined for the whole sky. We consider only the region where the TGAS selection function is known (cut 1).

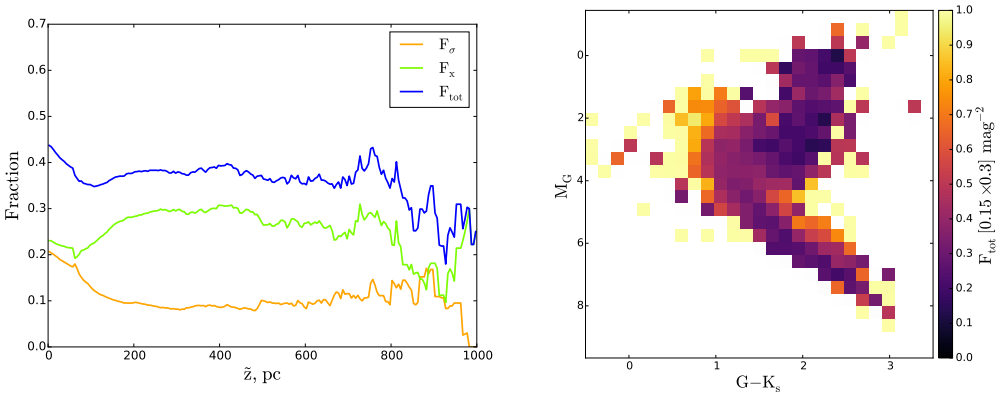

Figure 3.2: *Left*. Fraction of stars missing in the solar cylinder of 300 pc radius and 1 kpc height below the midplane. The orange line corresponds to the contribution from the low-quality stars, and the green curve gives an upper limit on the fraction of stars that did not enter the final sample because of the missing chemical abundances. Total fraction of missing stars is shown in blue. *Right.* The total fraction of the missing stars as a function of absolute G magnitude and $G-K_s$ colour.

Our selection criteria listed in Section 3.2.1 also add to the total incompleteness of the final sample. The first cut specifies the geometry of the modelled volume and is of no interest here. The parallax cut is modelled as described in Section 3.3.4. We also lose stars when applying the high-quality criteria (cut 4) together with the selection of stars with available APASS colour (part of cut 3). Finally, not all of the stars in the volume have measurements of Fe and Mg, even within the safe effective temperature range given. As a result, by applying cut 5, we also remove a part of the upper main sequence (UMS) and lose thin-disk stars. To quantify the fraction of the thin-disk stars missing in our final sample, we construct two additional data sets. The first contains stars with known chemical abundances that are classified as thin-disk populations but have low-quality or incomplete records (if any condition from cut 4 is not fulfilled or the APASS (B-V) colour is missing). The second data set contains stars that are unclassified as a results of missing chemical abundances, regardless of the quality of their spectra and astrometric solution or available photometry. At this point, we can derive a reliable estimate of the missing star fraction. To find the total number of the thin-disk stars in some vertical bin that also pass our parallax cut, we sum all the three samples in the following manner:

$$N_{tot} = N_f + N_\sigma + N_x \cdot \frac{\sum_{\tilde{z}_{min}}^{\tilde{z}_{max}} \rho_d}{\sum_{\tilde{z}_{min}}^{\tilde{z}_{max}} (\rho_d + \rho_t)}, \tag{3.1}$$

where N_f, N_σ, and N_x are the number of stars in the final, low-quality, and unclassified samples. The densities ρ_d and ρ_t are the local vertical density profiles of the thin and thick disks as inferred in Paper I and Paper II, respectively (and also the output of the local run from Section 2.3 with parameters from Table 2.1). The two limits $\tilde{z}_{min}$ and $\tilde{z}_{max}$ are the boundaries of the corresponding vertical bin. In order to simplify the expression, we drop the dependence on $\tilde{z}$ of all quantities in this equation. With this estimate we calculate the total fraction of the missing

stars F_{tot} as a function of height:

$$\begin{aligned} F_\sigma &= N_\sigma/N_{tot}; \quad F_x = N_x/N_{tot} \\ F_{tot} &= (N_\sigma + N_x)/N_{tot} \end{aligned} \tag{3.2}$$

Here F_σ and F_x are the fractions of stars that are missing in our final clean thin-disk sample because of the high noise and the absence of chemical abundances, respectively. The fractions given by Eq. 3.2 are shown in the left panel of Fig. 3.2. All three curves are smoothed with a window of 10 pc width. After summation over all vertical bins, we find that ~37% of the total expected number N_{tot} are missing in our final sample.

We also examine the fraction of missing stars in the Hess diagram. The right panel of Fig. 3.2 with the F_{tot} ratio calculated in colour-magnitude bins for the whole cylinder shows that the unclassified stars mostly influence the UMS; the LMS and red giant branch (RGB) regions are affected to a somewhat smaller extent. As it is not fully clear which of the unclassified stars really belong to the thin disk (the ratio of the thin- and thick-disk densities presented in Eq. 3.1 is used only to estimate the number of stars, it gives us no clue which population an individual star belongs to), we do not attempt to use the derived weights of the Hess diagram as an additional selection function during the modelling procedure. We rather keep it as a key for understanding the nature of the discrepancies between the data and model when they arise (see Section 3.5).

Now, treating all the described selection effects as independent, we define a completeness factor for the TGAS×RAVE thin-disk sample as follows:

$$S = S_Q(\tilde{z}) \times S_\varpi(\tilde{z}) \times S_{\rm RAVE}(\alpha, \delta, I) \times S_{\rm TGAS}(\alpha, \delta, J, J-K_s). \tag{3.3}$$

Here $S_\varpi(\tilde{z})$ corresponds to the selection effect arising from the parallax cut (practical realisation described in Section 3.3.4). $S_Q(\tilde{z}) = 1 - F_{tot}(\tilde{z})$ is the additional completeness factor related to the missing stars problem. All the factors of the selection function except for S_Q were applied at the creating of the stellar populations and calculating of the quantities of interest such as Hess diagrams or velocity distribution functions, whereas S_Q was taken into account at the post-processing of the results (Section 3.3).

3.3 Model and simulations

3.3.1 Modelling procedure

Before going into the details, we sketch a general overview of the modelling procedure summarising all steps discussed below in Sections 3.3.2-3.3.6.

We start with discretisation of the age-metallicity space and assigning an isochrone to each age-metallicity pair (Section 3.3.2). After this, we create a cylindrical grid (Section 3.3.3) and populate each of its space volumes with the predicted types of stars (characterised by age, metallicity, and mass from the isochrone) and take into account the parallax cut (Section 3.3.4), reddening, the TGAS×RAVE selection function (Section 3.3.5), and the corresponding abundance and photometric cuts. Then we account for the vertical effect of the distance error (Section 3.3.6) and investigate the properties of the mock sample as a function of distance from the midplane (Section 3.4).

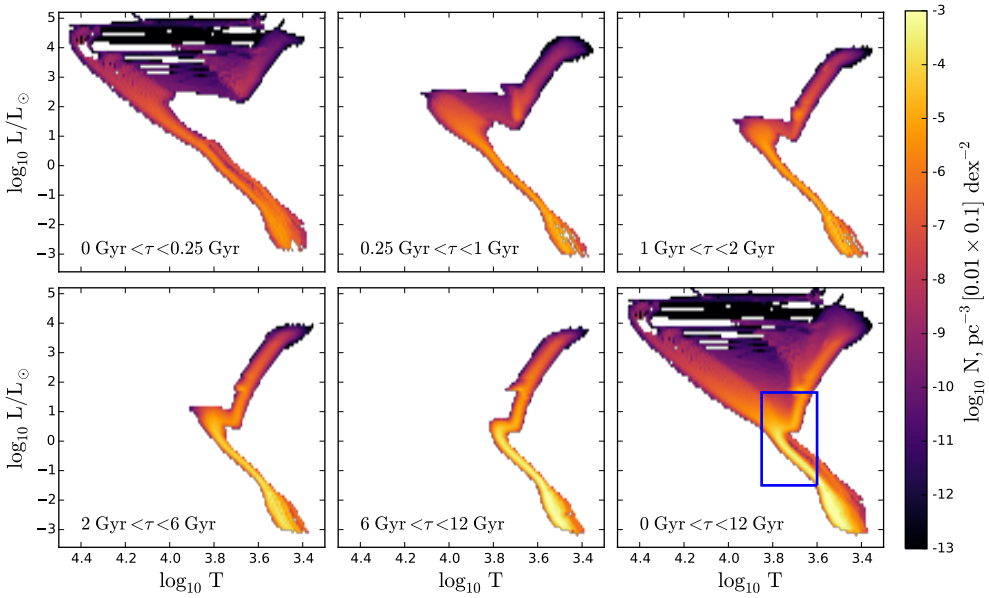

Figure 3.3: Theoretical HR diagrams for the thin disk as predicted by the local JJ model with the use of MIST isochrones. Five age bins illustrate the contributions from the different thin-disk populations to the total HR diagram (lower right). The blue box roughly corresponds to the region studied in this work.

3.3.2 Creation of the stellar assemblies

We start our modelling with thin-disk mono-age subpopulations. Each age corresponds to a unique value of metallicity as prescribed by the AMR law. We add a Gaussian scatter in metallicity $\sigma_{[Fe/H]} = 0.15$ dex. Each age τ_i is then associated with seven metallicities representing a Gaussian with a mean AMR(τ) and a dispersion $\sigma_{[Fe/H]}$. Each metallicity subpopulation is given an appropriate weight w_k, such that $\sum_{k=1}^{7} w_k = 1$. In Paper I a similar scatter in metallicity was modelled to reproduce the observed metallicity distributions of Geneva-Copenhagen F and G stars, which can be interpreted either in terms of observational errors or in terms of real physical scatter in metallicity of mono-age populations. In the present study the added dispersion $\sigma_{[Fe/H]}$ corresponds to a physical scatter in metallicity as the age-metallicity grid is then used to select isochrones. This complexity roughly accounts for the effect of radial migration, which is not explicitly introduced in our model.

The next step is to include the full stellar evolution, which we do by analogy to the procedure described in Section 2.5.2. We use of the Modules and Experiments in Stellar Astrophysics (MESA, Paxton et al., 2011, 2013, 2015) Isochrones and Stellar Tracks (MIST, Dotter, 2016; Choi et al., 2016)[21]. We take a set of 67 isochrone tables that safely cover the whole range of the modelled metallicities, [Fe/H] = −0.6-0.47. The logarythmic age range of isochrones belongs to a range of $\log(\tau/\mathrm{yr})$ = 7-10.08, step is 0.02. Each of the 3 360 stellar assemblies constructed earlier is associated with the isochrone that has the closest age and metallicity to the modelled ones. The MIST isochrones cover a range of initial masses 0.1-300 $M_\odot$ and we work in the range of 0.1-100 $M_\odot$ according to the limiting masses of our IMF. The total number

[21] http://waps.cfa.harvard.edu/MIST

of the stellar assemblies is $\sim 5 \cdot 10^6$. As previously, each stellar assembly j is assigned with a surface number density N_j^{Σ}, which is calculated by weighting the SFR with the IMF and accounting for the weights w_k. Isochrones also provide us with the present-day stellar masses, stellar parameters $\log L$, $\log T_{\rm eff}$, $\log g$, and absolute magnitudes in the standard $UBVRI$ system, 2MASS JHK_s, and Gaia G band. The resulting table of the mock stellar assemblies with the stellar parameters, multi-band photometry, and surface densities for the solar neighbourhood is a basis of the following modelling. The remaining modelling procedure may be briefly described as checking which of these types of stars were actually observed in the TGAS×RAVE cross-match and then were selected by us for the thin-disk sample as well as for further distributing them in the local cylinder.

The volume number density is calculated by:

$$N_j^V(z) = \frac{N_j^{\Sigma}}{2h(\tau_j)} \exp\left\{-\Phi(z)/\sigma_{W,s}^2(\tau_j)\right\}, \tag{3.4}$$

where N_j^{Σ} is the surface number density of a given stellar assembly, $h(\tau_j)$ and $\sigma_{W,s}(\tau_j)$ are the half-thickness and the vertical velocity dispersion defined by the AMR for the corresponding age τ_j, respectively, and $\Phi(z)$ is the total vertical potential at a height z, as predicted by the fiducial local model. As an example outcome of the local model, we calculated the volume densities N_V at $z = 0$ kpc for all modelled stellar assemblies and constructed a Hertzsprung-Russel (HR) diagram for the thin disk in the solar neighbourhood (Fig. 3.3).

Before proceeding to the next steps of the modelling, we pre-select stellar assemblies with the effective temperatures belonging to the RAVE range (cut 5). An additional pre-selection is based on the expectations for the range of absolute G magnitudes in the sample, which we set to −2-10 mag (see right panel of Fig.3.2). The reduced subset of the stellar assemblies used further during the simulations falls into the blue frame on the bottom right plot in Fig. 3.3.

3.3.3 Sample geometry

To model the geometry of the thin-disk sample, we create a 3D grid in cylindrical coordinates (r, θ, z). To adequately account for the parallax cut (see below), we set the initial radius of the cylinder to $r_{in} = 500$ pc. This is larger than we used for the data (cut 1 in Section 3.2.1). The modelled cylinder extends vertically up to $z_{max} = 1$ kpc below the midplane. The region above the Galactic plane is not included. We bin this cylindrical volume (1) in height z with a step of $\Delta z = 5$ pc, (2) in angle θ, which is measured from the cylinder axis, with a step of $\Delta\theta = 3°$, and (3) in radial direction r by binning the space in 20 intervals in logarithmic scale. This gives $4.8 \cdot 10^5$ space volumes, but only those of them that correspond to the directions of observations are used in the actual modelling.

3.3.4 Parallax cut

The distances r and z defining the model grid are not directly comparable to the distance estimates derived for the data sample through the inversion of observed parallaxes. In order to get around the problem, we translate the model true distances into the space of observed parallaxes. This allows us to include in the model the same parallax cut as was applied to the data, and also to account for the distance error effects.

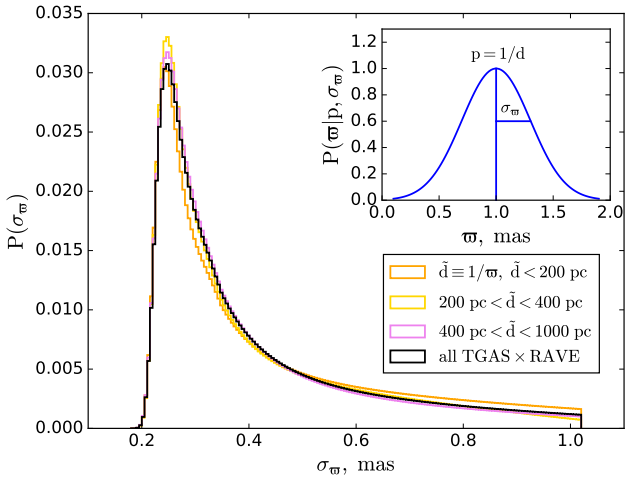

Figure 3.4: Normalised parallax error PDF as taken from the full TGAS×RAVE cross-match (black). The orange, yellow, and violet histograms correspond to the PDFs of the subsamples with different distance ranges. The similarity of their shapes demonstrates an independence of the parallax error from the parallax itself (i.e., the distance). In the inset an example normalised Gaussian PDF for the observed parallax is plotted. The true parallax and its observational error are set to 1 and 0.3 mas, respectively.

We split the procedure into two independent steps. First, we apply Eq. 3.5 at fixed z and translate the model distances to the observed parallaxes. This allows us to reduce the number of the stellar assemblies left for the modelling at a given height by applying a parallax cut identical to the one we introduced in Section 3.2.1. Then we reduce the radius of the modelled cylinder to 300 pc using the distances calculated from the mock observed parallaxes. At this stage, we treat different z-slices as independent, i.e., the modelled stellar assemblies remain at their initial height. The fact that a given star is observed at $\tilde{z}$ different from its true distance from the midplane z is taken into account at the second stage during a post-processing of the quantities calculated in the different z-slices. This strategy was chosen in order to simplify the modelling process and speed up the calculations, as it allows us to include the effect of the distance error in vertical direction at the post-processing stage of the simulations. We now consider the first step with the parallax cut more closely; the second step is described in Section 3.3.6.

We start with the usual assumption that the observed parallax ϖ is distributed normally about the true parallax $p = 1/d$ with a standard deviation σ_ϖ depending on the stellar brightness, exposure time, and number of observations per star. This is a good approximation of the real shape of the TGAS parallax error distribution which is known to deviate slightly from normality only beyond $\sim 2\sigma$ (Lindegren et al., 2016). Under this assumption, the normalised probability of the observed parallax ϖ is given by the Gaussian PDF:

$$P(\varpi|\sigma_\varpi, p) = \frac{1}{A}\exp\left[-\frac{(\varpi - p)^2}{2\sigma_\varpi^2}\right] \qquad \text{with } A = \sqrt{2\pi}\sigma_\varpi. \tag{3.5}$$

An example PDF of the observed parallax is shown in the inset of Fig. 3.4.

At each fixed height z, we have 2 400 volume spaces, as implied by the model grid. We assume that the parallax error PDF as derived from the TGAS×RAVE cross-match (Fig. 3.4, black histogram) does not depend on parallax or direction of observation (see coloured PDFs in Fig. 3.4). After this, we can easily assign parallax errors to our stellar assemblies when modelling the stellar content in each volume space. Then the observed parallaxes can be derived from the Gaussian distribution in accordance with Eq. 3.5. We perform this separately for each radial bin in a given z-slice. In summary, at each fixed z, we select a pie of 20 space

volumes corresponding to the same angle θ and different distances from the cylinder axis, and in each of them, we reduce the table of stellar assemblies in the following way:

- A random true heliocentric distance d within the given space volume is assigned to each stellar assembly and then converted into the true parallax $p = 1/d$.
- Parallax errors σ_ϖ are drawn randomly from the parallax error PDF.
- The corresponding observed parallaxes ϖ are derived as random values from the Gaussian PDF $P(\varpi|\sigma_\varpi, p)$.
- The observed parallaxes ϖ are converted into observed distances $\tilde{d} = 1/\varpi$.
- Cuts identical to those used for the data sample are applied: $\varpi > 0$, $\sigma_\varpi/\varpi < 0.3$.
- Only stellar assemblies with $\tilde{d}\cos b < 300$ pc are selected. This allows us to account for the fact that the parallax errors cause some stars that lie outside the modelled cylinder to be observed within it (alternatively, stars that actually belong to the cylinder of 300 pc radius may appear at larger distance and be excluded from the sample).
- We also remove the stellar assemblies located at $|b| < 20^\circ$ to reproduce the spatial geometry of the modelled sample.

The resulting set of tables of the stellar assemblies are then subjected to the TGAS×RAVE incompleteness factor.

3.3.5 TGAS×RAVE selection function

After the parallax cut is applied, in each space volume at a given z we calculate the visual magnitudes in the I and J bands as well as colour $(J-K_s)$ for all the stellar assemblies left. Apparent or absolute magnitudes in other photometric bands such as B, V, or G are also added when necessary. Visual magnitudes are calculated with the true model distances d.

The recent progress in mapping the dust content of the Milky Way allowed us to use a fully realistic 3D extinction model instead of the two-dimensional (2D) map of Schlegel et al. (1998) (Paper II) or the simple analytic extinction model from Vergely et al. (1998) (Paper III). We implement the 3D dust map from Bovy et al. (2016a)[22], which is a combination of 3D extinction models from Drimmel et al. (2003), Marshall et al. (2006), and Green et al. (2015).

The photometric cuts $7 < I/\mathrm{mag} < 13$, $0 < (J-K_s)/\mathrm{mag} < 1$, and $0 < J/\mathrm{mag} < 14$ are then applied to the stellar assemblies, in full analogy with the corresponding data selection criterion (cut 3, Section 3.2.1). The surface number densities of the remaining stellar assemblies are weighted with the completeness factor $S_{\mathrm{RAVE}} \times S_{\mathrm{TGAS}}$. For this we bin the stellar assemblies in I and J magnitudes with the corresponding steps of $\Delta I = 0.5$ mag and $\Delta J = 0.1$ mag as well as in colour $(J-K_s)$ with a $\Delta(J-K_s) = 0.14$ mag step. After this, we calculate the resulting stellar number in a given grid cell by converting the surface stellar densities N_j^Σ into N_j^V in accordance with Eq. 3.4 and multiplying the volume density by the volume of the cell. With the known number of stars as well as their multi-band photometry, ages, and metallicities we can predict the vertical density laws for different populations, calculate vertical kinematics with the AVR, and study the modelled sample in the colour-magnitude plane.

[22] https://github.com/jobovy/mwdust

3.3.6 Vertical distance error

At the stage of post-processing the results, when the quantities of interest are calculated for different z, we also account for the effects of the distance errors in the vertical direction. To do so, we introduce a probability $P(\tilde{z}|\sigma_z, z)$, which defines a likelihood for a quantity Q calculated at its true z to be observed at another height $\tilde{z}$ given a corresponding vertical error σ_z. In order to derive the $P(\tilde{z}|\sigma_z, z)$ expression, we rewrite Eq. 3.5 in terms of heliocentric distance:

$$P(\tilde{d}|\sigma_d, d) = \frac{1}{B}\exp\left[-\frac{d^4}{\sigma_d^2}(1/\tilde{d} - 1/d)^2\right] \qquad \text{with } B = \int_0^\infty P(\tilde{d}|\sigma_d, d)d\tilde{d}, \tag{3.6}$$

where $\tilde{d}$ and d are the observed and true heliocentric distances and σ_d is the distance error. At this point, we need to know how both distances as well as the distance error correspond to the true and observed heights, i.e., the functions of interest are $\tilde{d}(\tilde{z})$, $d(z)$ and $\sigma_d(z)$. The first can be easily derived from the thin disk sample itself (blue curve in Fig. 3.5). Its behaviour is ruled by the sample geometry. Owing to the cut $|b| > 20°$, close to the midplane the radius of the cylinder grows linearly with $\tilde{z}$ until it reaches 300 pc, so that the mean distance $\tilde{d}$ increases almost linearly with height. At large $\tilde{z}$, the mean distance asymptotically approaches $\tilde{z}$. The function $d(z)$ can be calculated within the model framework, but for our accuracy, it is sufficient to use an approximation $\tilde{d}(\tilde{z}) \approx d(z)$. Then the distance error is estimated as $\sigma_d(z) = 1/d^2(z) \cdot \sigma_\varpi$ with a constant $\sigma_\varpi = 0.3$ mas, which is a typical parallax error of the TGAS catalogue (magenta curve in Fig. 3.5).

The vertical effect of the distance error is illustrated in Fig. 3.6. The colour-coding represents the normalised probability $P(\tilde{z} - \Delta z/2 < \tilde{z} < \tilde{z} + \Delta z/2|\sigma_z, z)$. The two projections of this diagram are of special interest. The vertical projection, calculated for a true height $z = 500$ pc, gives a skewed PDF that describes a likelihood for a star located at z to be observed at other heights $\tilde{z}$, $P(\tilde{z}|\sigma_z, z)$. The horizontal projection shown for the same but observed height $\tilde{z} = 500$ pc describes the impact from the different vertical bins on a given $\tilde{z}$, which is expressed with the PDF $P(z|\sigma_z, \tilde{z})$. While the maximum of the probability density $P(\tilde{z}|\sigma_z, z)$ belongs to a

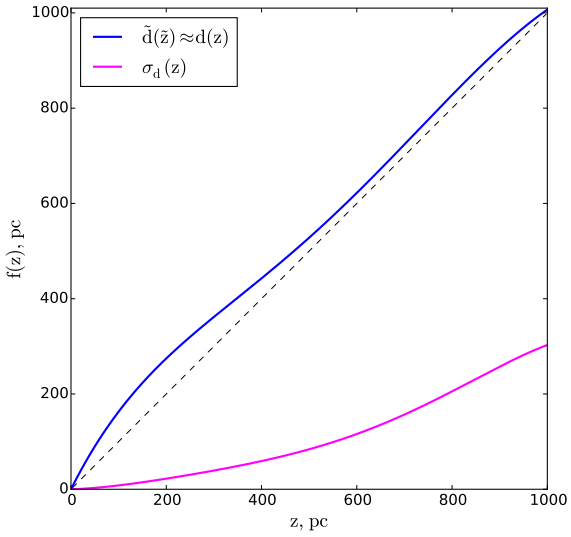

Figure 3.5: Mean observed heliocentric distance $\tilde{d}$ versus height $\tilde{z}$ as derived from the data (blue curve). The thin-disk sample was binned in $\tilde{z}$, and at each height, the mean heliocentric distance was calculated. The observed dependence was fitted with a polynom of the fifth order to obtain a smooth function. The distance error as a function of height was then derived with the derived mean distance (magenta curve).

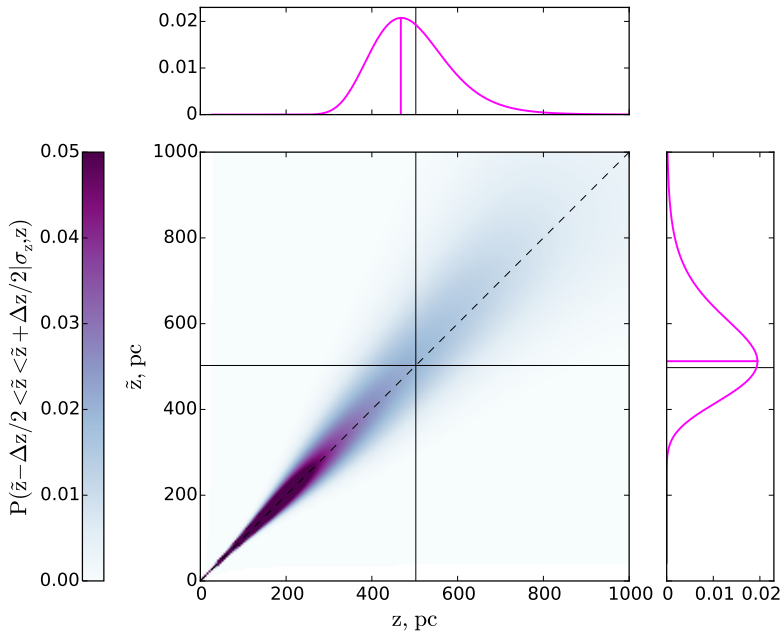

Figure 3.6: Diagram showing the vertical effect of the distance error. The normalised probability for a true height z to be associated with the observed distance from the midplane $\tilde{z}$ given the thin-disk sample geometry and the typical distance errors from Fig. 3.5 is colour-coded. The horizontal and vertical projections are example PDFs $P(\tilde{z}|\sigma_z, z)$ and $P(z|\sigma_z, \tilde{z})$ for the true and observed heights of 0.5 kpc. The skewness of the two distributions results in two effects: (1) an individual star is more likely to be observed at a height larger than its true distance from the midplane, and (2) the observations at some $\tilde{z}$ are more likely to be affected by smaller heights. The magenta lines in the projection subplots show distribution maxima.

slightly larger height than the corresponding true z, the shift is opposite in case of $P(z|\sigma_z, \tilde{z})$: a star observed at a given $\tilde{z}$ most probably belongs in reality to a smaller height. It is also clear that the vertical effect of the distance error is negligible close to the midplane, where the distance errors are small, and has the largest impact on the location of the most distant stars. We also have to consider heights larger than $z_{max} = 1$ kpc in order to allow the stars to not just leave the cylinder, but also to enter it from the larger heights (in full analogy with the radial direction, when we first consider a cylinder of a larger radius and then cut it to 300 pc after allowing stars to migrate horizontally due to the distance error effect). However, as the stellar density decreases approximately exponentially with increasing height, we expect the effect of not including $z > z_{max}$ to be very small except in the most distant parts of the cylinder, so we do not model it.

Finally, we write

$$P(\tilde{z}|\sigma_z, z) = P(\tilde{d}(\tilde{z})|\sigma_d(z), d(z)). \tag{3.7}$$

With Eq. 3.7 we calculate the quantities of interest as functions of observed height $\tilde{z}$:

$$Q_{\tilde{z}} = S_Q(\tilde{z}) \cdot \sum_{z=0}^{z_{max}} Q_z P(\tilde{z}|\sigma_z, z) \tag{3.8}$$

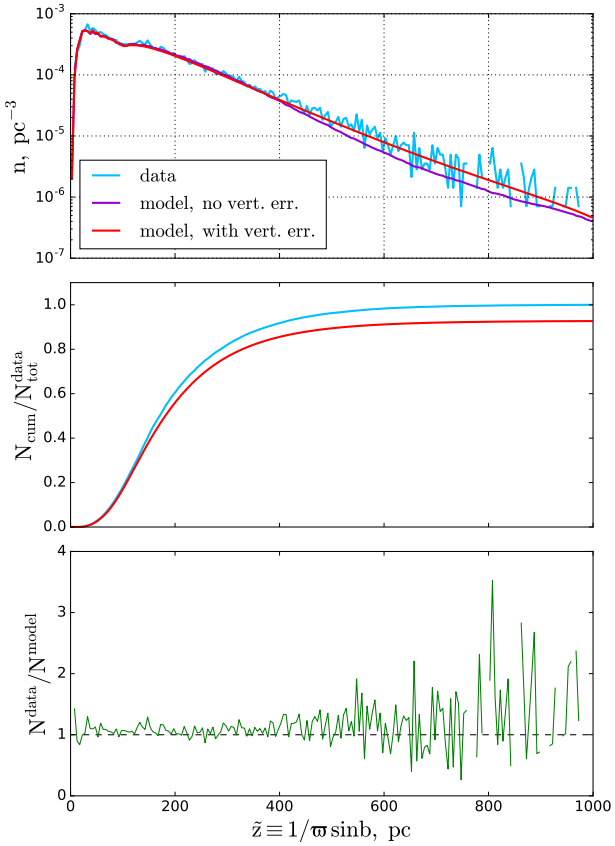

Figure 3.7: *Top.* Volume number density of stars in the modelled cylinder. The blue line represents the data, and violet and red curves are the model predictions before and after the vertical error effect is taken into account. *Middle.* Cumulative number of stars in the cylinder as a function of observed height $\tilde{z}$. The values are normalised to the total number of stars in the TGAS×RAVE thin-disk sample. *Bottom.* Ratio of the observed to predicted number of stars in the vertical bins.

Here an additional and final correction is included in the form of the $S_Q(\tilde{z})$ factor discussed in Section 3.2.2. Alternatively, when we wish to derive the model predictions in the horizontal slice of a thickness of $|\tilde{z}_2 - \tilde{z}_1|$, we write

$$Q_{\tilde{z}_1 < \tilde{z} < \tilde{z}_2} = \sum_{\tilde{z}=\tilde{z}_1}^{\tilde{z}=\tilde{z}_2} Q_{\tilde{z}}. \tag{3.9}$$

Eq. 3.8 and 3.9 are used to account for the vertical effects of the distance error for the modelling of the stellar density laws and vertical kinematics. An alternative procedure for the Hess diagrams is presented in Section 3.4.3.

3.4 Results

3.4.1 Vertical density law

The first and most straightforward test that can be conducted with the JJ model is a comparison of the observed and predicted vertical density profiles because the primary focus of the model is the vertical structure of the stellar populations in the disk. By following the steps described in Sections 3.3.2-3.3.6, we calculate the vertical stellar density law for all stars in the cylinder, $n(\tilde{z}) = N_{\tilde{z}}^V / V_{\tilde{z}}$ with $V_{\tilde{z}}$ being the volume of the corresponding vertical bin. The top panel of Fig. 3.7 shows the stellar number density as calculated from the data (blue line) and as predicted

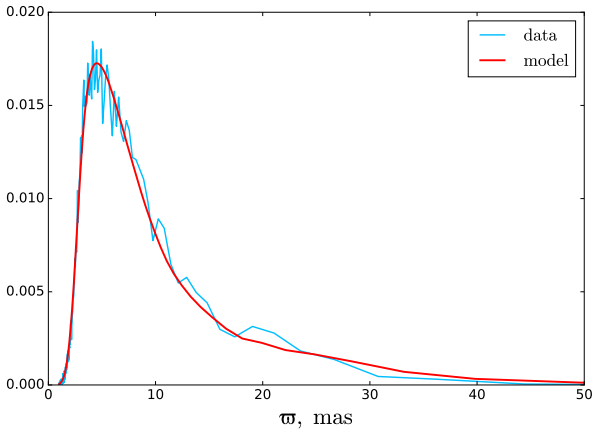

Figure 3.8: Normalised parallax distributions as derived from the TGAS×RAVE thin-disk sample and as predicted by the JJ model.

by the model (violet and red curves). The final model prediction is plotted in red, while the violet curve is given for comparison to show the number density law as predicted without the impact of the vertical distance error taken into account. The procedure of weighting the model output with the PDF $P(\tilde{z}|\sigma_z, z)$ results in migration of stars to larger observed heights $\tilde{z}$, which in turn leads to a better consistency with the data far from the midplane. On the other hand, the effect is very small close to the Galactic plane, predictably in view of the negligible distance error in close vicinity to the Sun (Fig. 3.5, top panel). The observed and modelled density profiles agree well at all heights, which also implies a good agreement in the local region close to the Galactic plane where the model is well calibrated and is therefore expected to produce robust predictions. By analogy to the vertical profiles, we derive a distribution of stars over the observed heliocentric distances, that allows us to quantify the model-to-data agreement in spherical volumes as well. The error in the predicted stellar number within a 25 pc local sphere (considered for the model calibration in Paper III) is ∼6%. However, we note that the actual number of observed stars in this volume is smaller than ten, such that the statistics is strongly influenced by Poisson noise.

When investigated in terms of the cumulative number of stars as a function of observed height, the model and data demonstrate 7.8% disagreement at $\tilde{z} = 1$ kpc (Fig. 3.7, middle panel). The ratio of the observed to the modelled stellar number in individual vertical bins as shown in the bottom panel of Fig. 3.7 helps to understand the systematic trends in the model-to-data differences. The ratio is close to unity over a wide range of heights, which means that the robustness of the modelled vertical profile and our treatment of the stars that are missing in the volume as a results of the lack of chemical abundances and low quality of other parameters are reliable (Fig. 3.2). It is also clear that starting from ∼ 600 pc, the Poisson noise begins to dominate star count statistics in the bins. From a height of approximately 800 pc, the number of stars is systematically under-represented in the model. Consistently, we expect this region to be biased in our simulation as we do not model stars at heights larger than 1 kpc and thus do not account for their possible presence in our sample owing to the large distance errors.

It is also interesting to perform a comparison in the space of observed parallaxes in order to validate our two-step treatment of the parallax uncertainties and the vertical distance errors. Following our standard steps, we calculate the parallax distributions at individual model heights z and then weight the results with the corresponding probabilities $P(\tilde{z}|\sigma_z, z)$ and completeness factors $S_Q(\tilde{z})$. The final distribution is shown in Fig. 3.8. Both data and model are normalised to

the total number of observed and predicted stars, such that the shapes of the distributions can be clearly compared. We find a very good agreement between the two curves which demonstrates the reliability of our forward-modelling approach.

3.4.2 Vertical kinematics

It is illustrative to test the model performance in terms of the vertical kinematics that was originally used to calibrate the model parameters (Paper I). Again, following the routine described in Sections 3.3.2-3.3.6, we evaluate for each observed height $\tilde{z}$ the velocity distribution function $f(|W|)$ as a superposition of Gaussians with the standard deviations given by the AVR. We consider the absolute W-velocities in a range of 0-60 km s^{-1} with a step of $\Delta|W| = 2$ km s^{-1}. The width of the step was selected such that it allows tracing the shape of the velocity distribution function but at the same time is larger than the typical observational error in the velocity bin. Following Eq. 3.9, we model $f(|W|)$ in six horizontal slices probing the dynamical heating of the disk as a function of distance from the midplane. The observed and predicted normalised velocity distribution functions calculated for the different ranges in $\tilde{z}$ as well as for the whole cylinder are shown in Fig. 3.9. Green points represent the data with the error bars calculated as standard deviation of the Poisson distribution. The red curves are the model predictions. In general, there is a very good agreement between the observed and modelled vertical kinematics of the sample. The total predicted $f(|W|)$ (Fig. 3.9, right plot) is consistent with the data within 1σ at almost all $|W|$. This is also true for the velocity distribution functions compared to the data at different heights (Fig. 3.9, three left columns). A noticeable discrepancy appears in the two lowest bins, for 0 pc $< \tilde{z} <$ 100 pc and 100 pc $< \tilde{z} <$ 200 pc, where the fraction of the dynamically cold populations is underestimated in our model. In general, a trend with the height is clearly evident: with the increase of the distance to the midplane, the shape of $f(|W|)$ becomes less peaked at small $|W|$. This is a natural and straightforward result as more dynamically heated populations reach larger distances from the Galactic plane because their velocities are higher.

We also compare $f(|W|)$ in four magnitude bins, for which we select different parts of the MS (CMD in Fig. 3.10). The bin ranges are the same as used in our previous work (compare to Fig. 3 in Paper I). The CMD shows the whole TGAS×RAVE thin-disk sample colour-coded with the RAVE metallicity. One can see that there is a metallicity gradient across the MS is visible such that each of the defined magnitude bins contains a mixture of stars with different metallicities and ages. To model $f(|W|)$ for the selected magnitude bins we add the same colour-magnitude cuts to the calculation procedure and remove the stars that do not fall under the given criteria after adding the reddening, at the stage of applying the TGAS×RAVE selection function (Section 3.3.5). The remaining calculation procedure is the same. The velocity distribution functions for the MS also show a good consistency with the data (Fig. 3.10, left), though the model slightly underestimates the role of the dynamically cold populations for the bin 3.5 mag $< M_V <$ 4.5 mag.

3.4.3 Hess diagrams

In order to achieve a deeper insight into the space distribution of the thin-disk populations, we also investigate the modelled cylindric volume in the 2D colour-magnitude space, i.e., by building Hess diagrams. We use the Gaia G and 2MASS K_s filters and construct the Hess

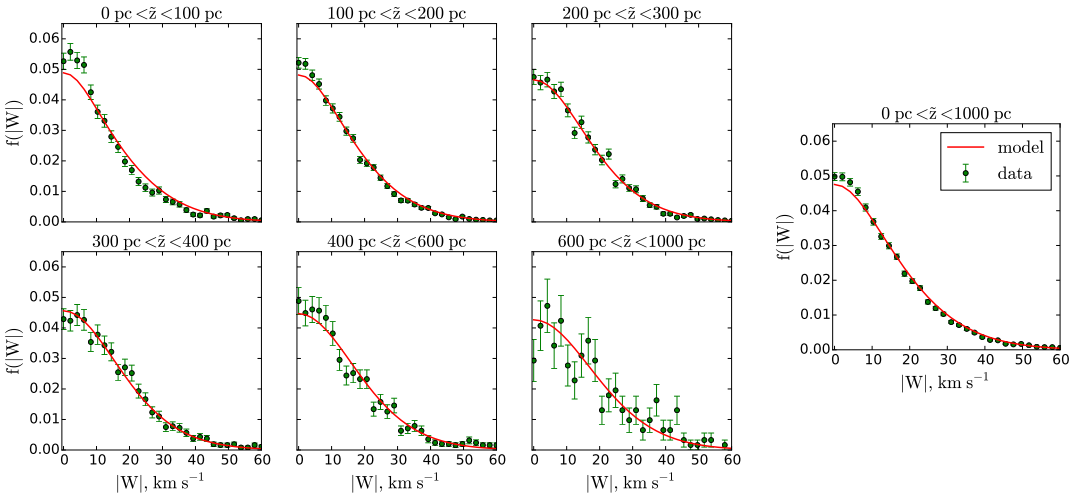

Figure 3.9: Normalised velocity distribution functions $f(|W|)$ for the six horizontal slices (3×2 plots on the left). The right graph shows $f(|W|)$ for the whole modelled cylinder.

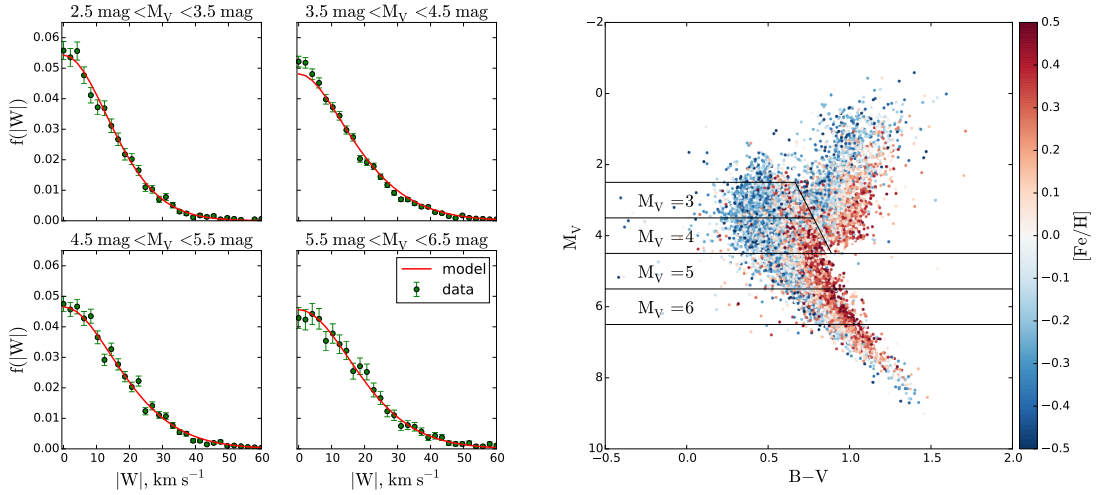

Figure 3.10: Normalised velocity distribution functions $f(|W|)$ for the different M_V cuts. The selection of the MS stars and separation into magnitude bins is shown on the right, where the CMD of the full TGAS×RAVE thin-disk sample is plotted with APASS photometry and the RAVE metallicity colour-coded.

diagrams in $(G-K_s, M_G)$ within the range of colours and absolute magnitudes of −0.5-3.5 mag and 9.5-1.5 mag, respectively, with corresponding steps of $\Delta(G-K_s) = 0.05$ mag and $\Delta M_G = 0.14$ mag. The typical uncertainty of the visual G-band magnitude is ~ 0.003 mag and for the colour $(G-K_s)$, it is larger by about a factor of ten, ~ 0.025 mag. Both values are well within our resolution on the Hess diagram axes, thus the choice of G and K_s photometry allows us to construct high-quality Hess diagrams without the need to complicate the simulations by adding photometric errors.

The calculation procedure in this case differs from the one described previously at the stage of accounting for the vertical distance error. For each modelled height z, we visualise the stellar content of this thin horizontal slice on the colour-absolute magnitude axes. The absolute magnitude is itself a logarithmic function of the distance related to z through $d(z)$ (Fig. 3.5). This additional distance dependence is the reason why we cannot model the resulting Hess diagram by appropriate weighting of the predictions calculated at the true heights in accordance to Eqs. 3.8 and 3.9, as we did for the other quantities. In order to account for the impact of the populations lying at some true height z_1 on the Hess diagram modelled for the height z_2, we take into account that the populations from z_1, when observed at z_2, has different absolute magnitudes shifted by $\Delta M = 5\log(z_1/z_2)$. Thus, the vertical error effect adds a spread on the vertical axis on the Hess diagram.

To approach the problem, we rewrite Eq. 3.7 in terms of the absolute magnitudes:

$$P(\tilde{M}|\sigma_M, M) = \frac{1}{C}\exp\left[-\frac{1}{2}\left(\frac{5}{\ln 10\sigma_M}\right)^2\left(10^{0.2(\tilde{M}-M)}-1\right)^2\right] \tag{3.10}$$
$$\text{with } C = \int_{-\infty}^{\infty} P(\tilde{M}|\sigma_M, M)d\tilde{M}.$$

Here $P(\tilde{M}|\sigma_M, M)$ gives the probability of a star with the true absolute magnitude M to be associated with another magnitude $\tilde{M}$ given a magnitude error σ_M. The error in the absolute magnitude is a function of distance, i.e., of the height above or below the midplane:

$$\sigma_M = \frac{5}{\ln 10 d(z)}\sigma_d(z) \tag{3.11}$$

Now, we can smooth the Hess diagrams predicted for the different true heights z by taking the corresponding magnitude errors $\sigma_M(z)$ from Eq. 3.11. We refer to the value in some row of the Hess diagram calculated for a given z as H_M. Then the smoothing procedure can be expressed as

$$\tilde{H}_M = \sum_{M=M_1}^{M=M_2} H_M P(\tilde{M}|\sigma_M, M). \tag{3.12}$$

The limits M_1 and M_2 are related to the range of the heights of interest $\tilde{z}_1 < \tilde{z} < \tilde{z}_2$:

$$M_1 = M + 5\log(d(z)/d(\tilde{z}_1)) \tag{3.13}$$
$$M_2 = M + 5\log(d(z)/d(\tilde{z}_2))$$

The Hess diagram $\tilde{H}$ smoothed in such a way shows where in the absolute magnitude-colour plane the populations from the height z will appear when the range of observed heights $|\tilde{z}_2 - \tilde{z}_1|$ is considered. The resulting Hess diagram for the given range of heights can be evaluated as a

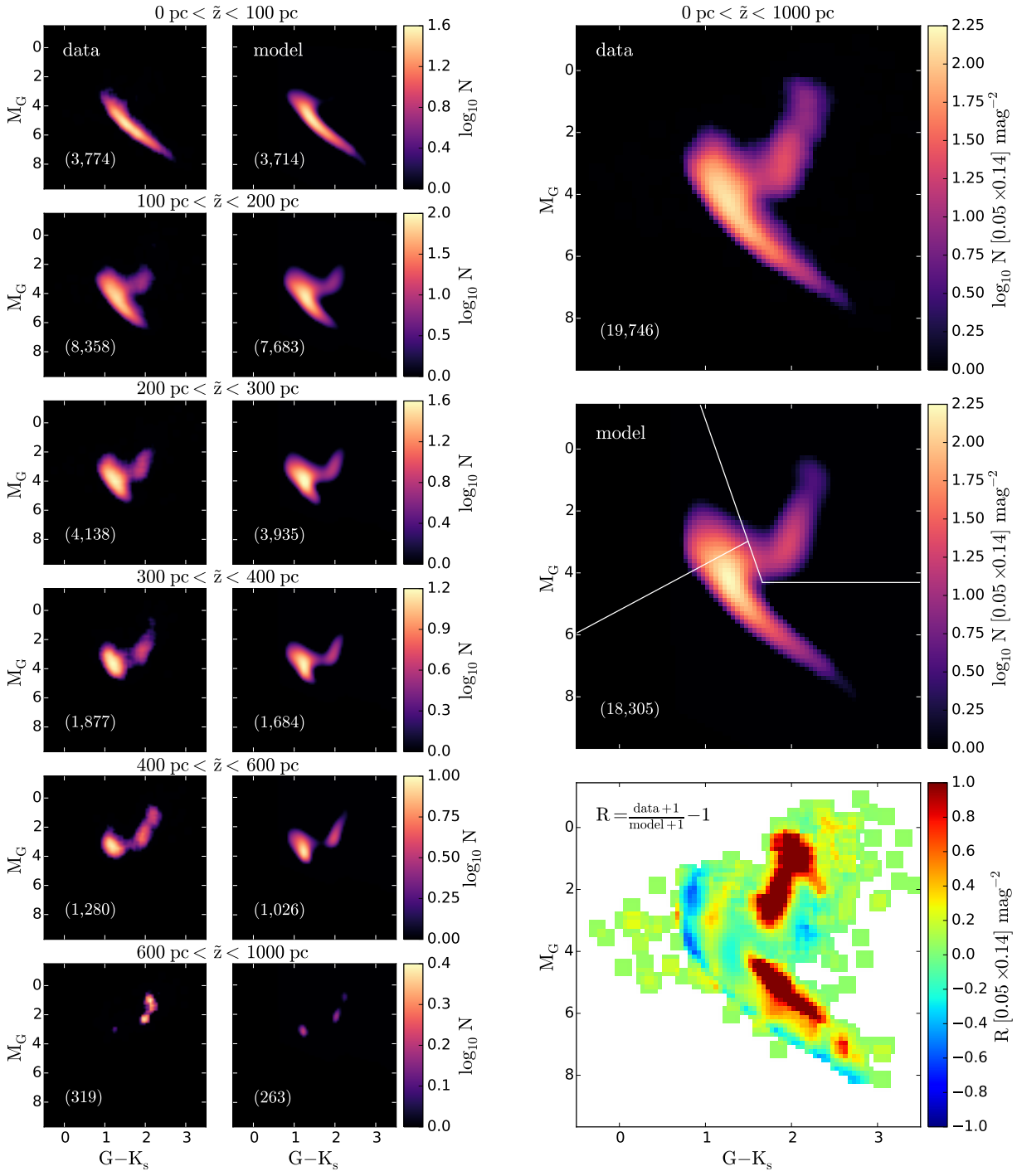

Figure 3.11: *Left.* Hess diagrams in $(M_G, G-K_s)$ as derived from the data and predicted by the model (left to right) shown for the different horizontal slices. The height increases from top to bottom. The numbers of stars are given in brackets. *Right.* Total Hess diagrams (top and middle) and their relative ratio (bottom). The white lines in the middle plot define the separation into the UMS, LMS, and RGB regions.

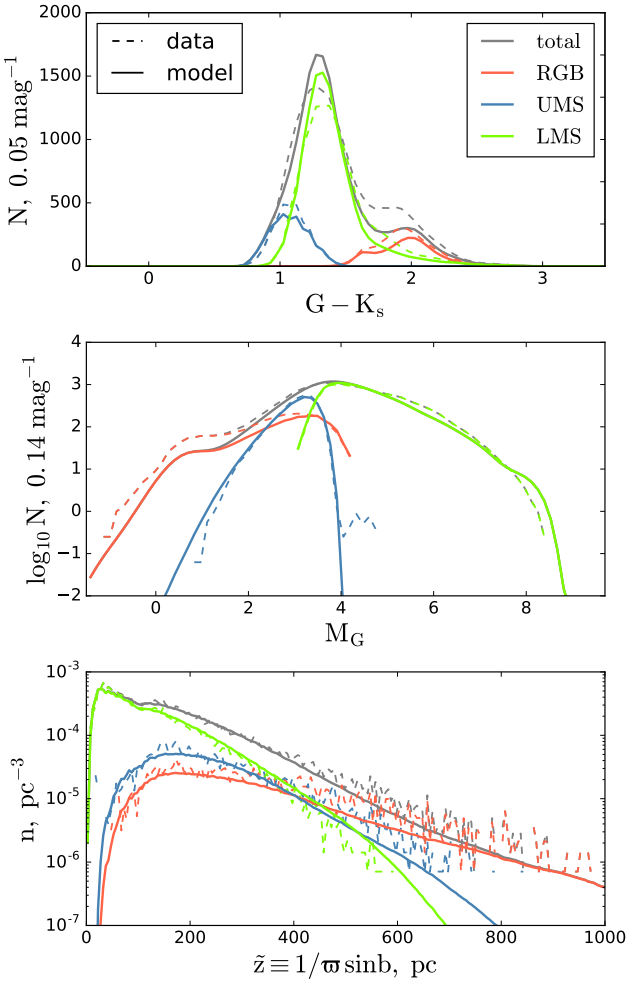

Figure 3.12: UMS, LMS, and RGB stars studied separately. *Top.* Colour distributions as observed and modelled for the whole local cylinder. *Middle.* Luminosity functions for the same three populations. *Bottom.* Stellar number densities as functions of observed height. The grey line corresponds to the red curve in Fig. 3.7.

sum over all $\tilde{H}$:

$$H_{\tilde{z}_1<\tilde{z}<\tilde{z}_2} = \sum_i S_Q(z_i)\tilde{H}_i. \tag{3.14}$$

We construct Hess diagrams for the same six vertical bins as were used in Section 3.4.2. Both observed and modelled Hess diagrams are additionally smoothed with a window 0.1×0.28 mag^2 (2×2 bins in $(G-K_s, M_G)$). The results are plotted in Fig. 3.11. The two left columns show the Hess diagrams as derived from the data and predicted by the model given for increasing $\tilde{z}$ (top to bottom). A pronounced vertical trend appears: close to the Galactic plane, the LMS stars dominate; at the middle heights, the contribution of the the UMS becomes important and RGB stars appear as well; and starting from $\tilde{z} \approx 400$ pc, the stellar populations in Hess diagrams are represented by UMS and RGB alone. All these changes are very confidently traced in the model. The right column in Fig. 3.11 shows three plots for the whole modelled cylinder (top to bottom) corresponding to the observed and predicted Hess diagrams, as well as their relative ratio calculated with the suppression of noise in the almost empty bins. The relative ratio plot demonstrates a general good agreement between data and model as it has already been inferred from investigating the vertical number density profiles, although a comparison in 2D space reveals the sources of model-to-data differences in more details. The typical model-to-data deviations over the Hess diagram are found to be ±20%, with the red

regions indicating the problematic areas (see Section 3.5).

We further investigate the UMS, LMS, and RGB populations separately defining them as shown with white lines in the middle plot of the right panel of Fig. 3.11. The border between the lower and upper parts of the MS approximately corresponds to the stellar masses of 1.5 $M_{\odot}$. We plot two projections of the total Hess diagrams onto the magnitude and colour axis. The resulting colour distributions and luminosity functions are shown in the top and middle panels of Fig. 3.12. In addition to the general difference in the number of stars, we see more clearly that the modelled LMS is more peaked than the observed one, while the UMS and RGB regions are less pronounced in the model. The same information can be obtained from the individual vertical density laws plotted for the three populations (Fig. 3.12, bottom panel). The LMS, UMS, and RGB regions are under-populated in the model by 3.6%, 6%, and 34.7%, respectively.

3.5 Discussion

In this section we discuss several potential problems of our modelling procedure.

When we analysed the Hess diagrams (Fig. 3.11), we found a few tenth of stars in the data that are clearly outliers (see the reddest and bluest $G-K_s$ values). These might be misidentified stars as well as contamination by the metal-poor thick-disk and halo stars and objects with unrealistic metallicities, magnitudes, or colours. One of the problematic red areas is associated with the LMS region: the observed MS is noticeably wider than the predicted one. This might be caused by the impact of binarity, which is ignored in our modelling. Additionally, metal-rich stars are present in the data sample ([Fe/H] > 0.2), and their number is underestimated with the model AMR (see parameter $[\mathrm{Fe/H}]_{\mathrm{p}}$ in Table 2.1 and also Fig.16 in Paper I, the metallicity prescribed to the youngest stellar population is +0.02 dex). Moreover, we predict an underestimated stellar density in the RGB region. This we attribute to the simplicity of accounting for the S_Q completeness factor, which is included in the modelling as a function of height above the plane (Fig. 3.2, left panel), although it also shows a variation with colour and absolute magnitude (Fig. 3.2, right panel). By ignoring this dependence of S_Q on magnitude and colour, we may over- or underestimate stellar numbers in the regions of the Hess diagram where the values of incompleteness at the right panel of Fig. 3.2 deviate considerably from the average. This effect can also be responsible for a blue region near the UMS at $G-K_s \approx 0.8$ mag (compare to the right panel of Fig. 3.2). On the other hand, when considered together with a blue region in the LMS (see colour range $1.8 \lesssim (G-K_s)/\mathrm{mag} \lesssim 2.8$ at the relative ratio plot in Fig. 3.11), it points to a small colour shift between the modelled and observed Hess diagrams of ~ 0.1 mag in $G-K_s$. There are several reasons that may be responsible for this: an underestimated reddening, a systematic shift of isochrones, or a lack of metal-poor thin-disk populations in the data due to an incorrect separation of the thin- and thick-disk stars; the interplay of all these factors is also possible. Taking into account the locality of our volume, however, it is improbable that this shift is related to the underestimated reddening. We return to this question in view of the new results obtained on the basis of Gaia DR2 (see below). Furthermore, we discuss the sensitivity of our results to the choice of dust map and stellar library.

A possible unreliability of the dust map can have a twofold impact on our results. First, the predicted Hess diagram may appear shifted in the colour-magnitude plane relative to the observed one. Second, as the data selection function strongly depends on apparent magni-

tude and colour and the predicted number of stars may change significantly over the colour-magnitude bins (this is particularly related to the UMS and RGB regions), under- or overestimation of extinction and reddening may add up to the uncertainty in star counts. The 3D dust map used in our simulations is mainly based on the high-angular resolution extinction model from Green et al. (2015) constructed by the statistical technique from photometric data of Pan-STARRS and 2MASS. The safe range of distances covered by this map lies approximately in a range from 300 pc to 4-5 kpc, although the values of the minimum and maximum reliable distance may significantly vary over the sky. In most of our modelled sky region, the minimum reliable distance is $\sim$ 200 pc and extends to 300 pc. This implies that reddening may not be modelled reliably in the regions of the cylinder that are in close vicinity to the Sun. However, we do not expect the roughness of the extinction map in the nearby areas to have a significant effect on the modelling process because with the cut of $|b| > 20°$, we avoid the most problematic near-plane regions. To quantify the impact of the extinction model on our results, we test an additional 3D reddening map from Capitanio et al. (2017)[23] when using Gaia DR2 data (see

[23] http://stilism.obspm.fr

Test	Data and selection	N_{obs}	N_{sim}	R, %
TGAS×RAVE	See Section 3.2.1	19, 746	18, 206	−7.8
Gaia×RAVE test#1	Gaia: astrometry, V_{los}, (G, $G_{BP} - G_{RP}$) RAVE: [Fe/H] Distances: BJ18 Geometry: solar cylinder (r, h) = (300 pc, 1 kpc), TGAS×RAVE sky area) $8 < G < 14$	63, 408	63, 842	+0.7
Gaia×RAVE test#2	Gaia: astrometry, V_{los}, (G, $G_{BP} - G_{RP}$) RAVE: [Fe/H] Distances: BJ18 Geometry: solar cylinder (r, h) = (100 pc, 1 kpc) $8 < G < 14$	29, 193	28, 834	+1.2
Gaia F stars	Gaia: astrometry, (G, $G_{BP} - G_{RP}$) Distances: BJ18 Geometry: solar cylinder (r, h) = (100 pc, 1 kpc) $0.4 < G_{BP} - G_{RP} < 0.7$, $7 < G < 14.5$, $M_G > 10$	19, 934	19, 326	−3
Gaia G-dwarfs	Gaia: astrometry, (G, $G_{BP} - G_{RP}$) Distances: BJ18 Geometry: solar cylinder (r, h) = (100 pc, 1 kpc) $0.8 < G_{BP} - G_{RP} < 1$, $8 < G < 16$, $M_G > 2(G_{BP} - G_{RP}) + 2.2$	64, 634	69, 862	+8.1
Gaia K-dwarfs	Gaia: astrometry, V_{los}, (G, $G_{BP} - G_{RP}$) Distances: inversed Gaia parallaxes Geometry: local sphere r = 50 pc $1.2 < G_{BP} - G_{RP} < 2$, $7 < G < 13$, $M_G > 10$	4 255	3 863	−9.2

Table 3.1: Additional tests of the local model against the Gaia DR2 data. BJ18 refers to Bailer-Jones et al. (2018)

below).

With the full stellar evolution now included in the modelling, our predictions are sensitive to the choice of the stellar evolution package. To quantify the corresponding uncertainty, we tested an alternative set of the PARSEC isochrones for the same range of metallicities and ages as described in Section 3.3.2. The total number of predicted stars increased by $\sim 10\%$, but no appreciable difference of the model behaviour was discovered apart from this.

As the Gaia DR2 astrometry and completeness are significantly improved with respect to TGAS (Lindegren et al., 2018; Arenou et al., 2018) and the Gaia radial velocities have an even better precision than those of RAVE (Katz et al., 2018), we perform a sanity check complementary to the local test using the Gaia DR2 astrometric parameters and radial velocities. To mimic the test presented in this paper, we use the Gaia×RAVE cross-match with the Gaia radial velocities (Soubiran et al., 2018) and select the local subset belonging to the same spatial volume and area on the sky as the TGAS×RAVE sample described in Section 3.2. We do not attempt to repeat the full forward-modelling described in Section 3.3.1 by accounting for parallax errors; instead, we use geometric distances from Bailer-Jones et al. (2018) derived in the framework of Bayesian approach on the basis of Gaia DR2 parallaxes. In this test we do not apply metallicity scatter to the AMR either, which allows us to reduce the number of

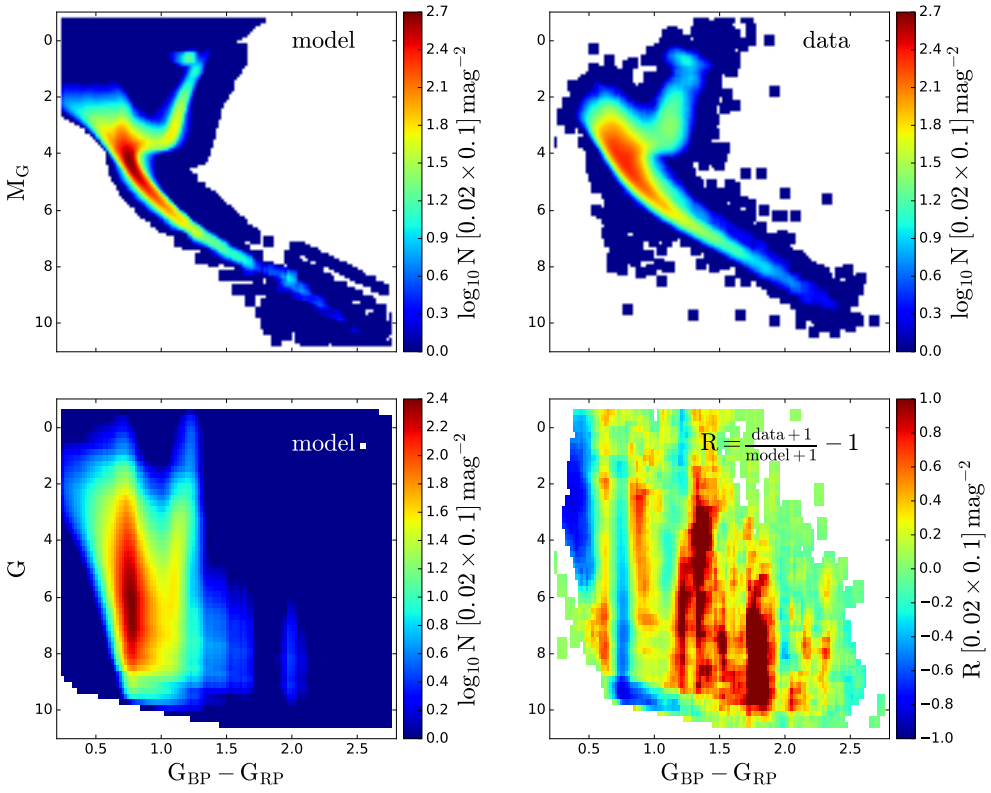

Figure 3.13: *Top.* Modelled (left) and observed (right) absolute Hess diagrams of the solar cylinder of 300 pc radius and 1 kpc height below the midplane with stars selected in the TGAS×RAVE sky area from Section 3.2. The thick disk is included into the modelling. Model and data are both smoothed with a window of 0.04×0.2 mag^2 (2×2 bins in $(G_{BP} - G_{RP}, G)$). *Bottom.* Modelled apparent Hess diagram of the same data sample (left) and the relative data-to-model ratio (right) similar to the bottom right plot in Fig. 3.11.

stellar assemblies and speed up the calculations. These simplifications do not influence the star counts much: (1) even if the distance errors reach $\sim 50\%$ for the individual stars at ~ 1 kpc, the overall stellar density at this heliocentric distance is quite low in our geometry, and the corresponding uncertainty introduced in the number of stars in the volume is not significant; and (2) the metallicity grid affects the modelled number of stars only indirectly through the sample selection function, which is sensitive to the apparent magnitudes and colours. In order to avoid additional incompleteness, no cuts on RAVE Fe or Mg abundances are used. Correspondingly, the thick disk is added to the model as a mono-age population of metallicity of -0.7 dex with a Gaussian dispersion of 0.2 dex. As some stars of the RAVE DR5 are missing in the Gaia× RAVE cross-match (because of unknown Gaia radial velocities or match problem; this makes up $\sim 11\%$ of the full RAVE DR5), we build a modified RAVE selection function that incorporates this additional incompleteness and use it for our test. The selected Gaia×RAVE local sample contains 63, 408 stars. We construct absolute and apparent Hess diagrams using the updated Gaia DR2 G-band and the new synthetic $G_{BP} - G_{RP}$ colour from PARSEC isochrones. As in the framework of our sanity check we do not account for the distance uncertainties and do not introduce scatter in the AMR function, we also do not expect a comparison in terms of the absolute Hess diagram being very instrumental. Indeed, both of the mentioned aspects contribute to the scattering of stars within the MS and RGB regions, such that in our case the predicted pattern on the absolute Hess diagram is much thinner and clearer than the observed one. The absolute and apparent Hess diagrams for our sanity check (Gaia×RAVE test#1 in Table 3.1) are shown in Fig. 3.13. The number of the UMS stars is somewhat overestimated in the model (blue stripe at the relative ratio plot). Also we identify a prominent mismatch of the stellar number density for the colour range of $1.7 < (G_{BP} - G_{RP})/\mathrm{mag} < 1.9$, which most probably points to the problem with isochrones than to any properties of our model as we do not apply any special colour cuts for this test and it is unlikely to be some additional selection effect. We also notice that the centers of the observed and predicted MS regions do not coincide perfectly, which implies a small colour shift of about ~ 0.05 mag in $G_{BP} - G_{RP}$ between the data and the model. Despite of these discrepancies, the overall star counts in the volume is now reproduced with $\sim 1\%$ accuracy. We compare the outcome of the sanity check star counts in case of using Bovy et al. (2016a) and Capitanio et al. (2017) dust maps and find only a difference between the two runs of $\sim 1\%$.

We also run several additional tests as listed in Table 3.1: Gaia×RAVE test#2 is a complementary to the sanity check and includes all common sky area between Gaia and RAVE; Gaia stars of F class and G-dwarfs are investigated separately in the solar cylinder of 100 pc radius; K-dwarfs in a 50 pc local sphere are also modelled. The results of all tests are in agreement with each other and also with our analysis performed on the basis of the TGAS×RAVE sample. The three last columns of Table 3.1 show the observed and predicted number of stars in the sample, and also the model-to-data deviations, whose absolute value lies in a range of $\sim$ 1-9%. Interestingly, we find a noticeable deviation between the predicted and observed vertical number density profiles of the G-dwarfs (Fig. 3.14, left panel) which is not observed for the other samples. This behaviour may point to the deviation of the simulated vertical gravitational potential from the real one because the difference in shapes is too significant and cannot be attributed to the effect of distance uncertainties. The underestimation of stars near the Galactic plane in our model may be related to a presence of open star clusters in the data: the JJ model predicts a smoothed distribution of stellar populations and does not account for the overdensity regions. In order to check whether the reported underestimation of dynamically cold stars may be also explained by the near-plane open clusters, we look at the K-dwarfs in the local 50 pc

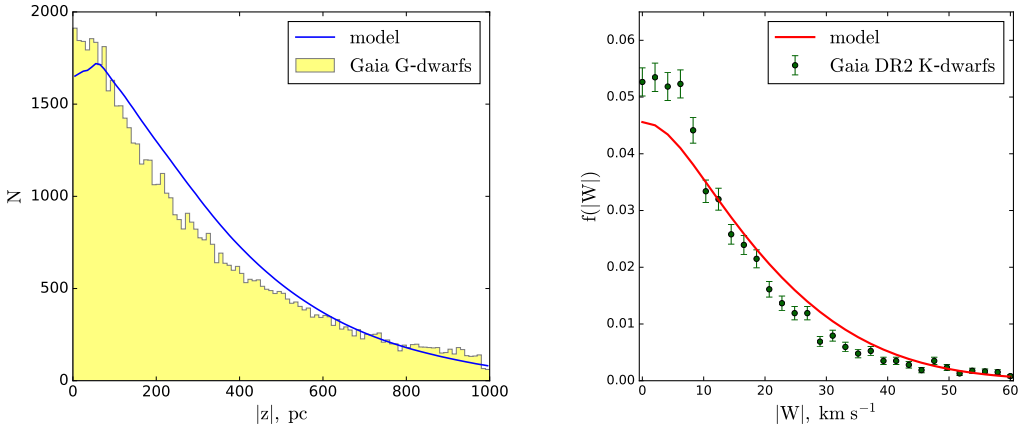

Figure 3.14: *Left.* Observed and predicted vertical number density profiles of the G-dwarfs in the solar cylinder of 100 pc radius and 1 kpc height. *Right.* Normalised $|W|$-velocity distribution function of the Gaia K-dwarfs in the 50 pc local sphere.

sphere. For this sample we also identify about 50 members of the Hyades open cluster and remove them from the data in order to ensure that they do not enhance a peak of the velocity distribution function at low $|W|$. The resulting velocity distribution function is shown in the right panel of Fig. 3.14, where the discrepancy between the model and data is clearly visible.

3.6 Conclusions

In this chapter we used the forward-modelling technique to test the semi-analytic JJ model. We selected a clean sample of thin-disk stars from the TGAS×RAVE cross-match providing precise astrometry as well as radial velocities and chemical abundances. We investigated the large local volume of the solar cylinder with radius of 300 pc extending to 1 kpc below the Galactic plane. The full stellar evolution in the form of MIST stellar isochrones was implemented in the model. For each modelled height z, we accounted for the parallax errors and reddening, and reproduced the incompleteness of the sample. The results were assigned with the additional weights to model the effect of the distance error in the vertical direction.

We found that the model predictions and data are in good agreement with each other. A deviation of $\sim 1\sigma$ is found between the modelled and observed velocity distribution functions $f(|W|)$ close to the Galactic plane, indicating that the role of the cold young stellar populations may be underestimated in our local disk model. When complemented with the velocity distribution functions for the different magnitude bins of the MS stars, this implies that the source of the discrepancy in vertical kinematics is related to the lower part of the UMS region. A complementary test based on the RAVE and new Gaia DR2 data confirm the results presented in Section 3.4, and the reported underestimation of dynamically cold populations is even more prominent when tested with Gaia DR2 astrometry and radial velocities.

With this realistic performance test we demonstrated the robustness of the local JJ model when compared to the data up to 1 kpc away from the Galactic plane. However, non-negligible deviations from the data are identified in case of the vertical kinematics of the disk, which suggests that the model should be adapted to match the Gaia DR2 data. The next step will include an extension of the model to other Galactocentric distances: the code Chempy will be

used to build the chemical evolution model of the disk, consistent with the adopted SFR and AVR varying with Galactic radius. For this purpose, Gaia DR2 and its next releases as well as high-resolution spectroscopic surveys such as APOGEE, Gaia-ESO, and GALAH will be of high benefit.

Chapter 4

Rotation curve of the extended solar neighbourhood[24]

4.1 Rotation curve: state of the art

The measurement of the Galactic rotation curve provides a powerful tool for constraining the mass distribution in the Milky Way and enters various branches of Galactic kinematics as an essential ingredient.

The measurement of the rotation curve inside the solar orbit at R_0 can be done without even knowing the distances to the tracers. Spectroscopic observations of HI regions and molecular clouds emitting in the radio range yield their line-of-sight velocities, which under the assumption of the circularity of orbits can be converted to the circular velocities purely geometrically. Though this technique known as the tangent point method (TPM, Binney and Tremaine, 2008) provides a quite accurate measurement of the inner rotation curve, it loses its applicability (1) at small Galactocentric distances $R < 5$ kpc, where the bar starts to dominate and therefore the orbits can significantly deviate from circular ones (Sofue et al., 2009) and (2) in the outer disk for $R > R_0$, where the distances to the tracers cannot be derived from a simple geometry. And even in the 'good' range of Galactocentric distances, $5\,\mathrm{kpc} < R < R_0$, the reliability of the TPM may be questionable as was shown by recent studies, which consider the spiral structure in galactic disks (Chemin et al., 2015, 2016). In order to probe the outer rotation curve, one is obligated to determine distances to the tracers. The distance uncertainties together with the decrease of tracers' density with increase of R explain why the outer rotation curve is known less confidently than its inner part. However, VLBI provides high-accuracy measurements of parallaxes and proper motions of young star-forming regions and covers a broad range of Galactocentric distances giving a strong constraint on the shape of the rotation curve (Reid et al., 2014). Still, due to the variety of techniques, difficulties in obtaining the accurate 6D dynamical information on coordinates and velocities, change in methodology at $R = R_0$ if one relies on the TPM inside the solar radius, the rotation curves determined by different authors are not in perfect agreement with each other (Bland-Hawthorn and Gerhard, 2016).

Sofue et al. (2009) presented a comprehensive analysis of previous measurements of the outer rotation curve, including data for HII regions and C stars, as well as points obtained by

[24]This chapter is based on the publication Sysoliatina et al. (2018a).

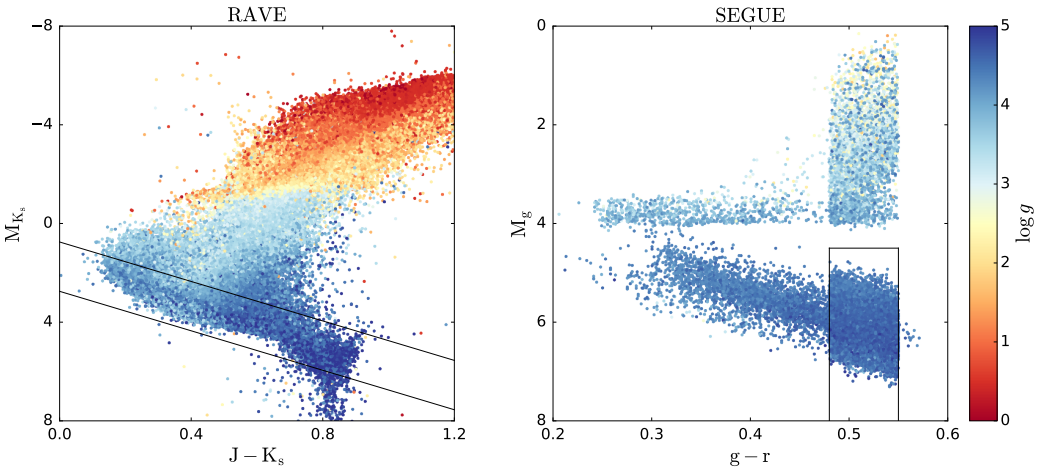

Figure 4.1: Colour-magnitude diagrams of the whole RAVE and SEGUE G-dwarf data from 2MASS and SDSS photometry, respectively. The applied cuts are shown in black lines.

the HI-disk thickness method and VLBI observations. The authors claimed a dip in the rotation curve between 7 and 11 kpc from the Galactic center, which they attribute to the presence of a ring of stellar overdensity in the Galactic disk influencing the gravitational potential. The dip is centered at 9 kpc, where the circular velocity drops by ~15 km s^{-1}. Huang et al. (2016) also found a similar depression in the rotation curve obtained from stars of the APOGEE and the LAMOST Spectroscopic Survey of the Galactic Anti-center (LSS-GAC, Liu et al., 2014). Kafle et al. (2012) used blue horizontal branch stars to construct a rotation curve, which also has a dip, although at bigger radii, about 11 kpc. In contrast to these results, López-Corredoira (2014), who studied proper motions of disk RC giants, obtained a flat rotation curve without any dip, although the errors still remain substantial. Having analysed a sample of APOGEE stars covering the range of Galactocentric distances 4-14 kpc, Bovy et al. (2012a) arrived at the same conclusion - the authors found that the rotation curve is approximately flat. Another flat rotation curve was obtained by Reid et al. (2014) by studying high-mass star-forming regions.

These apparently contradictory results show that a more detailed study of the local Galactic rotation curve is strongly warranted. Now, with the abundant data for distances and velocities of millions of stars from photometric and spectroscopic surveys of the last decade, the situation is more encouraging. However, as we show in this chapter, the solution of this task is not straightforward: while deriving the mean rotation velocity from the kinematic data, one has carefully account for the asymmetric drift correction, which itself requires some knowledge or plausible assumptions about the Galactic potential. Because of this inter-dependence between the input and output we have to approach the problem of the rotation curve reconstruction in an iterative and consistent way. And as we show in Section 4.3, inference from the JJ model can be quite useful for understanding the asymmetric drift and thus for constraining the overall Galactic potential through the reconstructed rotation curve.

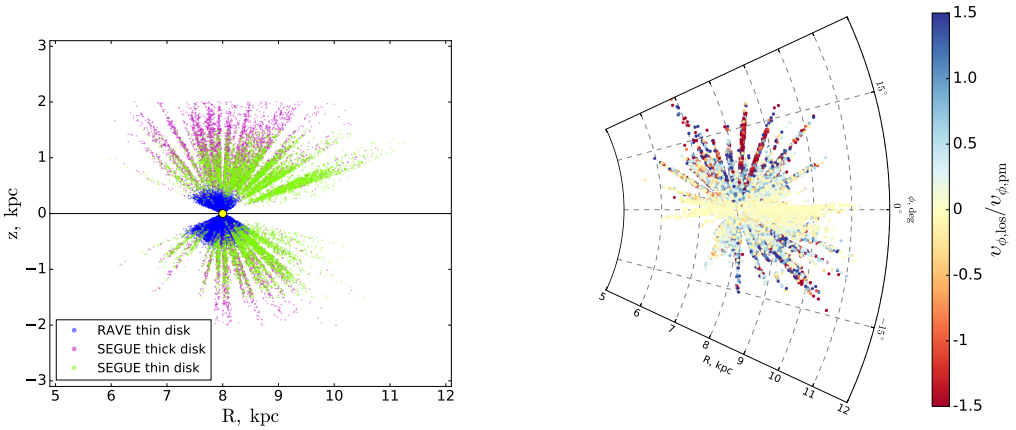

Figure 4.2: Spatial distribution of the RAVE and SEGUE samples. *Left.* Galactic cylindrical coordinates R and z of the final SEGUE (both thin- and thick-disk stars) and RAVE data samples (only thin-disk stars). The position of the Sun at Galactocentric distance $R_0 = 8$ kpc and height $z = 0$ kpc is marked with a yellow circle. *Right.* The whole SEGUE sample projected on the Galactic plane. The value of $\phi = 0°$ corresponds to the Sun-GC axis.

4.2 Data samples

Our analysis is performed in two steps. Firstly, we re-analyse the determination of the peculiar motion of the Sun and the radial scale lengths of the three thin-disk populations in the framework of the approach of Golubov et al. (2013), but based on the RAVE DR5 and a more careful treatment of the asymmetric drift correction (see Section 4.4). RAVE is a kinematically unbiased spectroscopic survey with medium resolution (R $\sim$ 7 500), which provides line-of-sight velocities, stellar parameters, and element abundances for more than 520, 000 stars. In RAVE DR5, improved stellar parameters and abundances were published and McMillan et al. (2018) derived new distances taking into account the TGAS parallaxes. Together with the proper motions from UCAC5 provided for most of the RAVE DR5 stars, this sample constitutes a reliable local kinematic dataset. From this sample we select stars at Galactic latitudes $|b| > 20°$ (to avoid the necessity to consider extinction), belonging to the stripe with $0.75 < K - 4(J - K_s) < 2.75$ on the colour-magnitude diagram (CMD) constructed with the 2MASS photometry (to select the main sequence and have a more uniform population of stars; Figure 4.1, left panel), with a signal-to-noise ratio $S/N \geq 30$, relative distance errors $\delta d/d < 0.5$, errors in proper motions $\delta\mu < 10$ mas yr^{-1} and line-of-sight velocities $\delta V_{los} < 3$ km s^{-1}. To select a cleaner thin-disk sample we also use RAVE abundances and take only stars with [Mg/Fe] < 0.2 (Wojno et al., 2016). Our final RAVE sample contains 23, 478 stars. Being very local (Figure 4.2, left panel), RAVE data cannot be directly employed for the reconstruction of the rotation curve, but rather are used for the purpose of investigating the solar peculiar motion.

In the second step we use a sample of G-dwarfs from SEGUE, a low-resolution (R $\sim$ 2 000) spectroscopic sub-survey of SDSS. The sample contains 40, 496 G-dwarfs with photometric parallaxes measured by Lee et al. (2011) with an accuracy better than 10% for individual stars. For our analysis we select stars with signal-to-noise ratio $S/N \geq 30$ (to ensure good accuracy of the spectroscopic data), colour index $0.48 \leq g - r \leq 0.55$ (to have a more uniform sample; most stars from the initial sample belong to this colour range anyway), and absolute

magnitude $M_g > 4.5$ mag (which when combined with the colour cut, neatly selects the main sequence; Figure 4.1, right panel). We separate the sample into the thin disk with $[\alpha/\mathrm{Fe}] < 0.25$, $|z| < 1.5$ kpc and the thick disk with $[\alpha/\mathrm{Fe}] > 0.25$, $|z| < 2$ kpc and $[\mathrm{Fe/H}] > -1.2$ (to decrease contamination by halo stars). After applying all the selection criteria, 10, 700 stars remain in the thin-disk, and 7 040 stars in the thick-disk samples. SEGUE data extend over the range of Galactocentric distances of 7-10 kpc (Figure 4.2), which makes them suitable for the local rotation curve analysis.

The tangential velocities v_ϕ of the SEGUE stars rely on measurements of line-of-sight velocities and proper motions with distances to individual stars. Radial velocities and proper motions are obtained by different observational techniques, so they have different accuracy (about 3 km s^{-1} for line-of-sight velocities and 3-4 mas yr^{-1} for proper motions, which at a distance of 2 kpc from the Sun converts to a $\sim$ 30-40 km s^{-1} error) and might have essentially different systematic errors. The relative contributions of line-of-sight velocity $v_{\phi,los}$ and proper motion $v_{\phi,pm}$ terms to the resulting tangential velocity v_ϕ change with Galactocentric longitude, so it is important to check that our data when binned in Galactocentric distance are not entirely dominated by one of the terms. The right panel of Figure 4.2 shows the SEGUE sample (both thin- and thick-disk stars selected with our criteria) projected on the Galactic plane. We calculate and compare the contributions $v_{\phi,los}$ and $v_{\phi,pm}$ measured relative to the solar Galactocentric velocity $v_\odot$. The contribution of the $v_{\phi,los}$ term is negligible on the axis Sun-GC, and in other regions values of the ratio reflect an interplay between the direction and the speed of stellar motions. Importantly, all longitudes are equally represented in our sample, so in the useful range of Galactocentric distances of 7-10 kpc we expect no bias in v_ϕ with respect to the observational techniques.

It is also important to note here that the RAVE data are expected to be kinematically unbiased by construction (see Wojno et al., 2017), so we do not need to worry about selection effects while working with them. As to the SEGUE G-dwarfs, simple selection criteria were used to construct this survey (Yanny et al., 2009), so we expect these data to be relatively free of kinematic bias and therefore we do not include a correction for the selection effects for SEGUE as well. As a measure of precaution, before using SEGUE data for the rotation curve reconstruction, we check our RAVE and SEGUE samples for consistency in terms of kinematics in order to justify our approach (see Section 4.4).

4.3 Jeans analysis

In this section we discuss the properties of the asymmetric drift, when applied to a large volume in Galactocentric distance R and height above the Galactic midplane z. The equation that we are going to formulate here is the basis of our work.

The asymmetric drift is defined as the lag in tangential speed of tracer populations with respect to the rotation curve, $V_a = v_c - \overline{v_\phi}$. The exact value of this quantity depends on stellar population properties and varies with the position in the Galaxy. This implies that in order to convert mean tangential velocities $\overline{v_\phi}$ to the rotation curve, we need to correct them for V_a. To quantify the asymmetric drift we use the same notation as in Golubov et al. (2013) and start with the radial Jeans equation for a stationary and axisymmetric system (in cylindrical

coordinates and with negligible mean radial and vertical motion):

$$v_c^2 - \overline{v_\phi}^2 = -R\left(\sigma_R^2 \frac{\partial \ln(\nu\sigma_R^2)}{\partial R} + \frac{\sigma_R^2 - \sigma_\phi^2}{R} + \sigma_{Rz}^2 \frac{\partial \ln(\nu\sigma_{Rz}^2)}{\partial z} + F(R,z)\right). \tag{4.1}$$

Here ν and $\sigma^2_{R,z,\phi,Rz}$ are the tracer density and velocity ellipsoid, $\overline{v_\phi}$ is the mean tangential speed of the population, v_c is its circular speed defined in the midplane and $F(R,z)$ measures the vertical variation of the radial force, i.e.,

$$F(R,z) \equiv \left.\frac{\partial\Phi}{\partial R}\right|_z - \left.\frac{\partial\Phi}{\partial R}\right|_0 \quad ; \quad v_c^2 = R\left.\frac{\partial\Phi}{\partial R}\right|_0, \tag{4.2}$$

where Φ is the total gravitational potential. The right-hand side of Eq. 4.1 is a measure of the asymmetric drift we are interested in. The last term vanishes at $z = 0$, but it should not be neglected at $z \neq 0$. Indeed, as with the increase of height above the midplane the radial gradient of the Galactic gravitational potential decreases, so does the measured tangential speed. This effect, if not taken into account, can result in two biases. Firstly, the derived circular velocity can be underestimated by a few kilometers per second, causing a shift of the rotation curve as a whole. Secondly, the typical distance of stars from the midplane varies at different Galactocentric radii due to the sample geometry (see SEGUE sample in Figure 4.2). This can cause a distortion of the rotation curve, which is unacceptable as the robust reconstruction of the shape of local rotation curve is the very aim of this work. The penultimate term is the well-known tilt term, which does not vanish in general even in the midplane (see Eqs. 4.8-4.10 below). Since these vertical correction terms lead to a systematic variation of the asymmetric drift increasing with $|z|$, we take them into account everywhere throughout this work, even for the relatively local RAVE sample with the range of useful distances limited to ± 0.5 kpc from the Sun (Figure 4.2, left panel).

The rotation curve, which we wish to determine, depends on the same Galactic potential. Therefore, we need to check carefully that we are not biasing the result implicitly by adopting a special model for the potential, entering Eq. 4.1 through the vertical gradients of tracer density and the radial force. We use a five-component model of the Galaxy with a spherical NFW DM halo with a local density $\rho_{h\odot}$ and power law slope $\gamma_h = -1$, a bulge component with mass M_b and three exponential disks for the gas, and the thin and thick disk with local surface densities Σ_i and radial and vertical scale lengths R_i and h_i (see Table 4.1 for the values of parameters). With this Galactic model we calculate the exact value of the vertical variation of the radial force using the *GalPot* code[25] (a stand-alone version of Walter Dehnen's GalaxyPotential C++ code, Dehnen and Binney, 1998a). In Section 4.3.2 we also derive an analytic approximation of this term.

The first term on the right-hand side of Eq. 4.1 can be characterised by the radial scale length R_E (which again may depend on R and z), and therefore reads

$$\sigma_R^2 \frac{\partial \ln(\nu\sigma_R^2)}{\partial R} = -\frac{\sigma_R^2}{R_E}. \tag{4.3}$$

At this point we remark that under the assumption of a constant disk thickness and a constant shape of the velocity ellipsoid σ_z^2/σ_R^2, which implies $\nu \propto \sigma_z^2 \propto \sigma_R^2$, we find R_E related to the radial

[25] Developed by P.McMillan and available at https://github.com/PaulMcMillan-Astro/GalPot

scale length of the tracer density ν through $R_\nu = 2\,R_E = const$. We will use this assumption later in order to convert the measured R_E into the radial scale lengths of the subpopulations (see Section 4.4).

As we show below in Sections 4.3.1 and 4.3.2, the third and the forth terms of Eq. 4.1 can be parametrised as well, so we can write the Jeans equation as

$$v_c^2 - \overline{v_\phi}^2 = \sigma_R^2\left(\frac{R}{R_E} - 1\right) + \sigma_\phi^2 - RF(R,z) - \eta\left(\sigma_R^2 - \sigma_z^2\right)\left(1 - \frac{z}{h_{\nu\sigma}}\right). \tag{4.4}$$

Here η gives the orientation of the velocity ellipsoid and $h_{\nu\sigma}$ is a characteristic scale height describing the vertical gradient of the tracer density and the velocity dispersion (see Section 4.3.1). This equation is still equivalent to Eq. 4.1. With a specification of the parameters and functions $F(R,z)$, η, $h_{\nu\sigma}$, R_E (e.g., R_E independent of R,z) we lose generality.

4.3.1 Tilt term

The third term in Eq. 4.1 describes the vertical density gradient and the change in the tilt of the velocity ellipsoid. The tilt angle of the velocity ellipsoid is defined as

$$\frac{1}{2}\tan(2\alpha_{tilt}) = \frac{\sigma_{Rz}^2}{\sigma_R^2 - \sigma_z^2}. \tag{4.5}$$

On the other side, the tilt angle can be parametrised with a parameter η, which describes the orientation of the velocity ellipsoid relative to the GC

$$\tan(\alpha_{tilt}) = \eta\frac{z}{R}. \tag{4.6}$$

Assuming that α_{tilt} is small, one then arrives at the following relation for σ_{Rz}^2:

$$\sigma_{Rz}^2 = \eta(\sigma_R^2 - \sigma_z^2)z/R. \tag{4.7}$$

The derivative of σ_{Rz}^2 is

$$\begin{aligned}\frac{\partial\sigma_{Rz}^2}{\partial z} &= \frac{\eta}{R}(\sigma_R^2 - \sigma_z^2) - \frac{z}{R}(\sigma_R^2 - \sigma_z^2)\frac{\partial\eta}{\partial z} \\ &+ \eta\frac{z}{R}\left(\frac{\partial\sigma_R^2}{\partial z} - \frac{\partial\sigma_z^2}{\partial z}\right) = \sigma_{Rz}^2\left[\frac{1}{z} + \frac{\partial\ln\eta}{\partial z} + \frac{\partial\ln(\sigma_R^2 - \sigma_z^2)}{\partial z}\right].\end{aligned} \tag{4.8}$$

Thus, the tilt term in Eq. 4.1 together with Eq. 4.8 gives

$$\sigma_{Rz}^2\left[\frac{1}{z} + \frac{\partial\ln(\eta\nu(\sigma_R^2 - \sigma_z^2))}{\partial z}\right]. \tag{4.9}$$

The second term in the brackets can be parametrised with some characteristic scale height $h_{\nu\sigma}$, so we arrive at

$$\sigma_{Rz}^2\frac{\partial\ln(\nu\sigma_{Rz}^2)}{\partial z} = \frac{\sigma_{Rz}^2}{z}\left[1 - \frac{z}{h_{\nu\sigma}}\right] = \eta\frac{\sigma_R^2 - \sigma_z^2}{R}\left[1 - \frac{z}{h_{\nu\sigma}}\right]. \tag{4.10}$$

We expect that the vertical variation of η and of $(\sigma_R^2 - \sigma_z^2)$ is small compared to the gradient of the tracer density ν. We can therefore relate the scale height $h_{\nu\sigma}$ to the characteristic scale height of the tracer density. For this purpose we use the half-thickness values of the mono-age subpopulations with ages of 4 Gyr, 6 Gyr, and 10 Gyr, taken from the local JJ model. The youngest subpopulation represents the bin with the highest metallicity. The adopted values of $h_{\nu\sigma}$ are 360 pc, 430 pc, and 530 pc, respectively.

4.3.2 Vertical gradient of the radial force

The last term on the right-hand side of Eq. 4.1 describes the vertical gradient of the radial force, and we have to specify the integral properties of the Galactic components in order to evaluate it. We assume a five-component model of the Galaxy, which consists of three disks and two spheroidal components. The parameters of the three exponential disks, a spherical DM halo with NFW profile and a point-mass bulge are given in Table 4.1. With the Galactic model assumed here, we find for the local ($R = R_0 = 8$ kpc) circular velocity and for the local slope of the rotation curve $v_0 = 241.1$ km s^{-1} and $\alpha = 0.01$, respectively, which is consistent with the values derived later in Sections 4.4 and 4.5. Throughout this chapter, we use this model to calculate the exact value of the vertical gradient of the radial force with the *GalPot* code. However, it might be also interesting and illustrative to express this term analytically in order to see explicitly its dependence on the model parameters.

We estimate $F(R,z)$ differently for spherical and for disk-like components:

$$F(R,z) = \sum_{i=h,b} F_i(R,z) + \sum_{j=d,t,g} F_j(R,z). \tag{4.11}$$

Here the indices i and j correspond to the spherical and disk terms, respectively.

For a spherical component like the DM halo and the bulge we can calculate the contribution directly in terms of their enclosed mass $M_r = M(<r)$ or their contributions β_i to the square of the rotation curve, $v_{c,i}^2 = \beta_i v_c^2$:

$$\begin{aligned} -RF_i(R,z) = -R\left[\frac{R}{r}\frac{\partial\Phi_i}{\partial r}\bigg|_{r=\sqrt{R^2+z^2}} - \frac{\partial\Phi_i}{\partial r}\bigg|_{r=R}\right] &= GR^2\left(\frac{M_R}{R^3} - \frac{M_r}{r^3}\right) \\ &= v_{c,i}^2(R) - \frac{R^2}{r^2}v_{c,i}^2(r) \end{aligned} \tag{4.12}$$

In case of a power law density profile of the DM halo and for the Kepler potential of the bulge, we can reformulate this in terms of the local power law index α_i of $v_{c,i}$:

$$-RF_i(R,z) \approx \frac{z^2}{R^2+z^2}\left(1 - \frac{d\ln v_{c,i}}{d\ln r}\bigg|_{r=R}\right) v_{c,i}^2(R) \approx (1-\alpha_i)\beta_i\frac{z^2}{R^2}v_c^2(R) \tag{4.13}$$

For the bulge, we have $\alpha_b = -0.5$ and for the DM halo $\alpha_h \approx 1 + \gamma_h/2$ (under the assumption of $a_h/R_0 \gg 1$), where $\gamma_h = -1$ is the power law index of the density profile. Deviations of the density profile in the inner Galaxy can be taken into account by adding the corresponding mass difference to the bulge mass.

For the disk components we derive the radial force variation by first integrating the verti-

cal force and then taking the radial derivative:

$$F_j(R,z) = \frac{\partial}{\partial R}\int_0^z dz_1 \frac{\partial \Phi_j(R,z_1)}{\partial z_1} \tag{4.14}$$

Expressing the derivative in the integral from Poisson's eq., we get:

$$F_j(R,z) = 4\pi G \frac{\partial}{\partial R}\int_0^z dz_1 \int_0^{z_1} dz_2 \rho_j(R,z_2) - \frac{\partial}{\partial R}\int_0^z dz_1 \int_0^{z_1} dz_2 \frac{1}{R}\frac{\partial}{\partial R}(R\frac{\partial \Phi_j}{\partial R}) \tag{4.15}$$

In the thin-disk approximation, the second term is usually neglected for the vertical force, but here we are interested in small vertical corrections of the radial force, so we need an estimate for it. In lowest order we can approximate this term (multiplied by $-R$) using $R\frac{\partial \Phi_j}{\partial R} \approx v_{c,j}^2$ at $z = 0$, which results in

$$R\frac{\partial}{\partial R}\int_0^z dz_1 \int_0^{z_1} dz_2 \frac{1}{R}\frac{\partial}{\partial R}(R\frac{\partial \Phi_j}{\partial R}) \approx R\frac{z^2}{2}\frac{\partial}{\partial R}\left(\frac{1}{R}\frac{\partial v_{c,j}^2}{\partial R}\right) \approx -2\alpha_j(1-\alpha_j)\frac{z^2}{R^2}v_{c,j}^2, \tag{4.16}$$

where a local power-law approximation for the disk rotation curve is used. We can combine this term with the contributions of the spherical components, because it has a similar structure.

For the calculation of the first term in Eq. 4.15, we need a detailed density model of the disk. The general form of the exponential density profiles of the three disk components for the gas, the thin and the thick disks is given by:

$$\rho_j(R,z) = \frac{\Sigma_j}{2h_j} \mathrm{e}^{-\frac{|z|}{h_j} - \frac{R-R_0}{R_j} - \frac{R_{cut,j}}{R}}, \tag{4.17}$$

where the inner cut $R_{cut,j}$ is zero for the thin and thick disks and is 4.0 kpc for the gas (see Table 4.1). Evaluating the first term of Eq. 4.15 we find:

$$4\pi G \frac{\partial}{\partial R}\int_0^z dz_1 \int_0^{z_1} dz_2 \rho_i(R,z_2) = -\frac{2\pi G \Sigma_j}{R_j} \mathrm{e}^{-\frac{R-R_0}{R_j} - \frac{R_{cut,j}}{R}} \left(|z| - h_j + h_j \mathrm{e}^{-\frac{|z|}{h_j}}\right). \tag{4.18}$$

Variable	Value	Source
$\rho_{h\odot}$ ($M_\odot$ pc^{-3})	0.014	Just and Jahreiß (2010)
a_h (kpc)	25	–
M_b ($M_\odot$)	1.1 10^{10}	–
Σ_d ($M_\odot$ pc^{-2})	30	Just and Jahreiß (2010)
h_d (pc)	300	Just and Jahreiß (2010)
R_d (kpc)	2.5	Golubov et al. (2013)
Σ_t ($M_\odot$ pc^{-2})	6	Just et al. (2011)
h_t (pc)	800	Just et al. (2011)
R_t (kpc)	1.8	Cheng et al. (2012)
Σ_g ($M_\odot$ pc^{-2})	10	Just and Jahreiß (2010)
h_g (pc)	100	Just and Jahreiß (2010)
R_g (kpc)	4.5	Robin et al. (2003)
$R_{cut,g}$ (kpc)	4.0	–

Table 4.1: Properties of the Galaxy used for calculations.

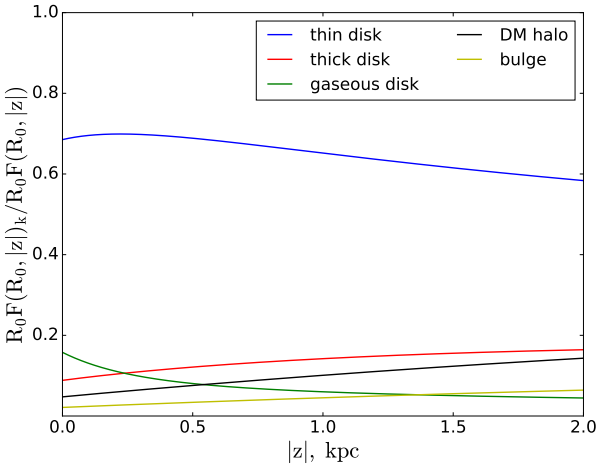

Figure 4.3: The vertical dependence of the relative contributions from the Galactic components to the vertical gradient of the radial force (Eq. 4.19). In the whole range of useful $|z|$, the contribution from the thin disk entirely dominates over all other components.

Combining all contributions from Eqs. 4.13, 4.16 and 4.18 we finally get:

$$\begin{aligned} -RF(R,z) &= \sum_{j=d,t,g} \frac{2\pi G\Sigma_j R}{R_j} \mathrm{e}^{-\frac{R-R_0}{R_j}-\frac{R_{cut,j}}{R}} \left(|z| - h_j + h_j \mathrm{e}^{-\frac{|z|}{h_j}}\right) \\ &\quad + \frac{z^2}{R^2} v_c^2(R) \left[\sum_{i=h,b} (1-\alpha_i)\beta_i - \sum_{j=d,t,g} 2\alpha_j(1-\alpha_j)\beta_j\right]. \end{aligned} \tag{4.19}$$

For consistency with the local rotation curve, there must be two constraints fulfilled. The relative contributions of all components $k = i, j$ to v_0^2 must add up to unity:

$$v_0^2 = \sum_k v_{c,k}^2 = \sum_k \beta_k v_0^2 \quad ; \quad \sum_k \beta_k = 1 \tag{4.20}$$

and the weighted local power law slopes for each component α_k must add up to the total power law slope α:

$$\begin{aligned} 2\alpha &= \frac{\mathrm{d}\ln v_c^2}{\mathrm{d}\ln R} = \sum_k \frac{\mathrm{d}\ln v_{c,k}^2}{\mathrm{d}\ln R} = \sum_k 2\alpha_k\beta_k \quad ; \\ \alpha &= \sum_k \alpha_k\beta_k. \end{aligned} \tag{4.21}$$

The local slopes α_k and contributions β_k of all components can be found from the shape of the input rotation curve defined by the parameters of the chosen Galactic model (Table 4.1). To find α_j and β_j we assume razor-thin exponential disks with a central mass deficit in case of the gas in order to simulate the inner hole. Ignoring the finite thickness of the disks leads to an error in $v_{c,j}$, but as we found from the comparison to the rotation curve calculated with *GalPot*, it is less than 3% at R_0. We also found that by recalibrating the R_d and Σ values of the disks it is possible to imitate the effects of thickness when taking $R_d^* = R_d/f$, $\Sigma^* = \Sigma f$ with $f = (v_{0,analytic}/v_{0,GalPot})^2 \approx 0.97$. The determined values of the slopes and relative contributions at $R = R_0$ are listed in Table 4.2. Although α_k and β_k are functions of R, within our accuracy we can treat them as constants for the usage at other Galactocentric distances.

Table 4.2: Local slopes and relative contributions of the individual Galactic components to the assumed rotation curve.

Component	α	β
Thin disk	-0.25	0.28
Thick disk	-0.47	0.1
Gaseous disk	0.91	0.01
Bulge	-0.5	0.1
DM	0.33	0.5

A test comparison of our analytic approximation of the $RF(R,z)$ term to its exact value given by the *GalPot* code shows that with our approximation we make a $\sim 7\%$ error at $z \approx 0$ kpc, which increases up to $\sim 30\%$ at 2 kpc. As we apply our correction to the mean height above the plane in the data bins, the actual error in $RF(R,z)$ is about $\sim 20\%$ or less. The slope of the rotation curve obtained from the SEGUE thin-disk sample when using Eq. 4.19 is $\alpha = 0.037 \pm 0.036$, which deviates by $0.12\,\sigma$ from the value found with the exact calculation of the vertical gradient of the radial force and is presented in Section 4.5. Thus, Eq. 4.19 might be a useful tool for understanding the vertical correction and parameter testing.

Using Eq. 4.19, we can estimate the importance of different terms in this vertical correction. Figure 4.3 shows the relative contributions of the five Galactic components to the vertical variation of the radial force term as follows from Eq. 4.19 applied to $R = R_0$. As it can be seen, the main contribution comes from the thin disk, which means that the resulting value of the correction is mostly sensitive to the thin-disk parameters. In particular, the R_d value is still under debates. In Golubov et al. (2013) it was estimated for three stellar subpopulations and the obtained values lie in a range between roughly 1.6 and 3 kpc. From this we cannot constrain the integral disk R_d more strictly as belonging to the interval $2\,\mathrm{kpc} < R_d < 3\,\mathrm{kpc}$, so for our correction calculation we use $R_d = 2.5$ kpc (see Tab. 4.1). Thus, this uncertainty in the value of the thin disk radial scale length is expected to cause the main uncertainty in our correction.

4.4 Solar motion and radial scale lengths

Before using the mean measured relative velocities of the tracer stars to find the mean tangential velocities $\overline{v_\phi}$ and correct them for the asymmetric drift, we need to correct for the peculiar motion of the Sun $(U,V,W)_\odot$, i.e., to convert the velocities to the local standard of rest. The determination of $U_\odot$ and $W_\odot$ from the stellar kinematics in the solar neighbourhood is not a matter of difficulty. For the radial and vertical components of the solar motion we adopt the values from Schönrich et al. (2010) $U_\odot = 11.1$ km s^{-1}, $W_\odot = 7.25$ km s^{-1}, which are also consistent with our data sets. In contrast, the determination of the tangential component $V_\odot$ is challenging. Due to the fact that the observed tangential motion of stellar populations is affected both by the solar peculiar velocity and the asymmetric drift, the task of disentangling them poses a problem. The classical value based on *Hipparcos* data is $V_\odot = 5.2$ km s^{-1} (Dehnen and Binney, 1998b). The more recent and widely used ones lie in a range of approximately 10-12 km s^{-1} (e.g., 12.24 ± 0.47 km s^{-1} in Schönrich et al., 2010). However, among recent estimates there are also values as high as ~ 24 km s^{-1} (Bovy et al., 2012a) indicating that the local stellar motions could be also influenced by non-axisymmetric Galactic features like spiral arms and bar. At the lower limit there is $V_\odot = 3.06 \pm 0.68$ km s^{-1} found by us previously in Golubov et al. (2013). Rather than taking an old value of $V_\odot$ together with the radial scale lengths for three metallicity populations, we re-determine them here in order to quantify the impact of our improved analysis in combination with the new distances and improved proper motions. To find the tan-

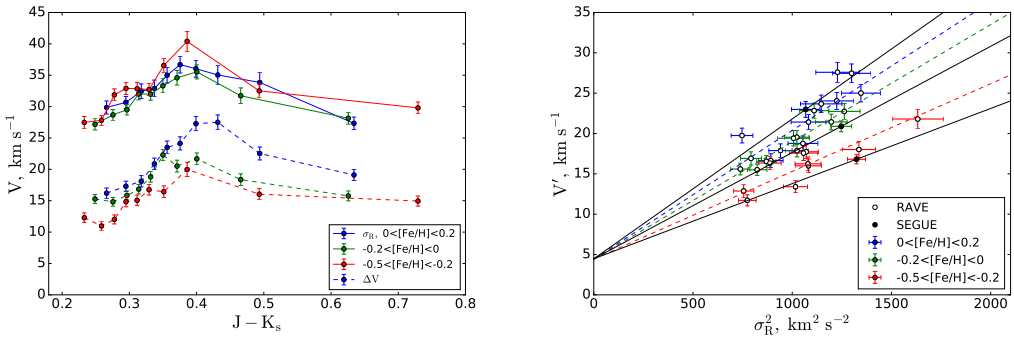

Figure 4.4: Recalculation and consistency check of the asymmetric drift correction for the RAVE and local SEGUE data samples. The RAVE data are recalculated using the improved distances from McMillan et al. (2018) and UCAC5 proper motions. *Left.* σ_R and ΔV as functions of $(J-K_s)$ 2MASS colour for different metallicity bins (compare to Figure 2 in Golubov et al., 2013). *Right.* V' as function of σ_R^2 in view of the new Strömberg relation (Eqs. 4.23 and 4.24) for each metallicity bin. The data points for the local G-dwarfs of SEGUE are added as full circles. The metallicity binning for RAVE and SEGUE data is identical and has the same colour coding. Only stars with 7.5 kpc $< R <$ 8.5 kpc and in the case of SEGUE with $|z| < 1.5$ kpc are selected for the plot. Dashed colour-coded lines are the linear least squares fit to the RAVE data. Black solid lines are added to read out the radial scale lengths corresponding to the positions of the SEGUE points and the value of $V_\odot$ determined from RAVE. Here and later on the error bars are calculated using the observational errors.

gential component $V_\odot$, we apply the new Strömberg relation as in Golubov et al. (2013), to the local RAVE data, but now including the vertical correction terms discussed in the two previous sections. We assume a Galactocentric distance of the Sun of $R_0 = 8$ kpc, which is consistent with Reid (1993) as well as with a more recent study by Gillessen et al. (2009). Then adopting the proper motion of Sgr A* from Reid and Brunthaler (2005) we get the solar Galactocentric velocity $v_\odot = 241.6 \pm 15$ km s^{-1}.

Applying Eq. 4.4 at $R = R_0$ and using $v_0 := v_c(R_0) = v_\odot - V_\odot$ and $\Delta V = v_\odot - \overline{v_\phi}$, we write for the left-hand side:

$$v_0^2 - \overline{v_\phi}^2 = (v_\odot - V_\odot)^2 - (v_\odot - \Delta V)^2 = -\Delta V^2 + 2v_\odot \Delta V - 2v_\odot V_\odot + V_\odot^2. \tag{4.22}$$

This leads to the new version of the Strömberg relation:

$$V' = V_\odot - \frac{V_\odot^2}{2v_\odot} + \frac{\sigma_R^2}{k'} \quad \text{with} \quad k' = \frac{2R_E}{R_0} v_\odot, \tag{4.23}$$

and the generalised version of V':

$$V' := \Delta V + \frac{\sigma_R^2 - \sigma_\phi^2 + R_0 F(R_0, z) + \eta(\sigma_R^2 - \sigma_z^2)\left[1 - \frac{z}{h_{v\sigma}}\right] - \Delta V^2}{2v_\odot}. \tag{4.24}$$

To make practical use of Eqs. 4.23 and 4.24, i.e., to determine values of $V_\odot$ and R_E, we need to bin our data sample into sub-bins with different kinematics. For this purpose we separate the RAVE sample in three subpopulations with different metallicities and then bin each subpopulation in $(J-K_s)$ colour. The left panel of Figure 4.4 shows such a binning of the measured velocity ΔV and squared radial velocity dispersion σ_R^2, which can be calculated

straightforwardly, without knowledge of $V_\odot$. One can clearly see that the kinematic properties change systematically with both metallicity and colour. Using the same binning, we plot V' versus σ_R^2 (Figure 4.4, right panel). For simplicity, we assume here that $\eta = const. = 0.8$ as derived in Binney et al. (2014) from the RAVE data. We also treat $h_{v\sigma}$ as independent of colour, though differing with metallicity and select appropriate values from the local JJ model (Section 4.3.1). The height above the midplane z in Eq. 4.24 is calculated for each metallicity-colour bin as a mean value of the absolute z for individual stars.

As in Golubov et al. (2013), we still see the systematic difference of $V'(\sigma_R^2)$ between metallicity bins, but the linear dependencies show a larger scatter. The assumption that R_E, similar to $h_{v\sigma}$, is approximately the same for all colours inside a given metallicity bin, but differs with metallicity, allows us to derive R_E values for the three metallicity subpopulations as well as $V_\odot$. To do so, we perform a simultaneous linear fit of the metallicity-colour sequences (shown with colour-coded dashed lines in Figure 4.4, right panel). The inverse slopes of the fitting lines k_i' can be directly converted to $R_{E,i}$, which under the assumption of constancy of the disk thickness and the shape of velocity ellipsoid (see Section 4.3) gives us the radial scale lengths for the selected populations. The solar peculiar motion can be read out from the V' extrapolated to zero radial velocity dispersion:

$$R_{d,i} = \frac{R_0 k_i'}{v_\odot}; \qquad V_\odot = v_\odot - \sqrt{v_\odot^2 - 2 v_\odot \, V'|_{\sigma_R^2=0}}\,. \tag{4.25}$$

The updated value of the tangential component of the solar peculiar motion is found to be $V_\odot = 4.47 \pm 0.8$ km s^{-1}, which translates to the local circular velocity $v_0 \approx 237 \pm 16$ km s^{-1}. The radial scale lengths for the metallicity bins are R_d(0<[Fe/H]<0.2) = 2.07 ± 0.2 kpc, R_d(-0.2<[Fe/H]<0) = 2.28 ± 0.26 kpc and R_d(-0.5<[Fe/H]<-0.2) = 3.05 ± 0.43 kpc, which together with $V_\odot$ is in agreement with our old values from Golubov et al. (2013).

Now we must check whether SEGUE stars also follow the same trend. For this purpose we split the thin-disk SEGUE sample into the same metallicity bins and consider only stars with Galactocentric distances $7.5 < R < 8.5$ kpc. The subdivision in colours is not possible for this data set because of its narrow colour range. Another characteristic of this sample is that G-dwarfs are distributed over a significantly larger range of $|z|$ (Figure 4.2, left). And though we do not reconstruct here the shape and orientation of the velocity ellipsoid as a function of R and z, we may roughly account for the vertical gradients of σ_R^2 and σ_z^2. To do so, we apply Eq. 4.24 for the calculation of V', not to the whole metallicity bin, but separately in vertical sub-bins ($|z|$ = 0-1.5 kpc with a step of 0.5 kpc) and calculate the resulting V' by taking a weighted mean of the values obtained for different $|z|$.

The SEGUE points (filled circles in Figure 4.4, right panel) demonstrate good consistency with the RAVE data, which means that for further analysis of SEGUE thin-disk sample we can securely use the values of scale lengths derived from RAVE. This is an important result, accounting for all uncertainties of the metallicity calibration in RAVE and possible velocity biases for SEGUE. To be even more precise, we can inverse the problem and read out scale lengths for individual points adopting the solar peculiar velocity derived with the RAVE data. The values of R_d calculated for the SEGUE data in such a way (see the three solid black lines in Figure 4.4, right panel) are: R_d(0<[Fe/H]<0.2) = 1.91 ± 0.23 kpc, R_d(-0.2<[Fe/H]<0) = 2.51 ± 0.25 kpc and R_d(-0.5<[Fe/H]<-0.2) = 3.55 ± 0.42 kpc. We use these new values and $V_\odot = 4.47 \pm 0.8$ km s^{-1} in our further analysis.

The linearity of the asymmetric drift correction, i.e., constancy of R_d versus σ_R^2, is still under debate. Nevertheless, even if the asymmetric drift dependence on σ_R^2 in fact turns out to be nonlinear for small σ_R^2 (as assumed by Schönrich et al., 2010), it will correspond to some shift in the measured circular velocity. We do not, however, expect this shift to change drastically at different Galactocentric radii. To the first approximation this would produce only a parallel displacement of the measured rotation curve. Being interested in the general shape of the rotation curve, not in the exact value of the rotation velocity, we apply the solar velocity and the radial scale lengths derived by Eq. 4.23 at all Galactocentric radii.

4.5 Asymmetric drift and rotation curve

Now, with updated values for the solar peculiar velocity and the radial scale lengths for three populations of the selected metallicities, we proceed to the determination of the rotation curve in the extended solar neighbourhood. We go back to the Jeans equation formulated for arbitrary (R,z) (see Eq. 4.4) and apply it to the thin-disk SEGUE stars. In principle, Eq. 4.4 can be directly used for the determination of the rotation velocity as all terms on the right-hand side are now known and the mean tangential speed can be expressed as $\overline{v_\phi} = v_\odot - \Delta V$, where $v_\odot$ is the tangential speed of the Sun and $(-\Delta V)$ is the mean observed tangential velocity with respect to the Sun. However, we would prefer to formulate the expression of the rotation velocity in terms of the asymmetric drift V_a, so we recall its definition:

$$V_a = v_c - \overline{v_\phi} = v_c(R) - v_\odot + \Delta V. \tag{4.26}$$

Inserting $\overline{v_\phi} = v_c - V_a$ into the left-hand side of Eq. 4.4, we arrive at the quadratic equation for the asymmetric drift:

$$V_a^2 - 2v_c V_a - R\left(F(R,z) + \eta\frac{\sigma_R^2-\sigma_z^2}{R}\left[1-\frac{z}{h_{\nu\sigma}}\right] - \frac{\sigma_R^2}{R_E} + \frac{\sigma_R^2-\sigma_\phi^2}{R}\right) = 0. \tag{4.27}$$

We solve Eq. 4.27 with respect to V_a and get:

$$V_a = v_c(R) - \left\{v_c^2(R) + R\left(F(R,z) + \eta\frac{\sigma_R^2-\sigma_z^2}{R}\left[1-\frac{z}{h_{\nu\sigma}}\right] - \frac{\sigma_R^2}{R_E} + \frac{\sigma_R^2-\sigma_\phi^2}{R}\right)\right\}^{1/2} \approx \frac{-RF(R,z) - \eta(\sigma_R^2-\sigma_z^2)\left[1-\frac{z}{h_{\nu\sigma}}\right] + \sigma_R^2\frac{R}{R_E} - (\sigma_R^2-\sigma_\phi^2)}{2v_c(R)}, \tag{4.28}$$

where the last line corresponds to the linear approximation ignoring the V_a^2 term. The difference of the non-linear and linear values for V_a is of the order of 5% or 1 km s^{-1}.

The final formula for calculating the rotation velocity at radius R for each bin (R,z) is from Eq. 4.26:

$$v_c(R) = \overline{v_\phi} + V_a = v_\odot - \Delta V + V_a, \tag{4.29}$$

with the asymmetric drift correction V_a given by Eq. 4.28. As V_a is itself a function of $v_c(R)$, the determination of the rotation velocity is an iterative procedure, during which we assume $v_c \propto R^\alpha$ and start with some small α as initial value. At each step of the iteration, the reconstructed rotation curve is fitted and the new value of α is derived to be plugged back into Eq. 4.28 via

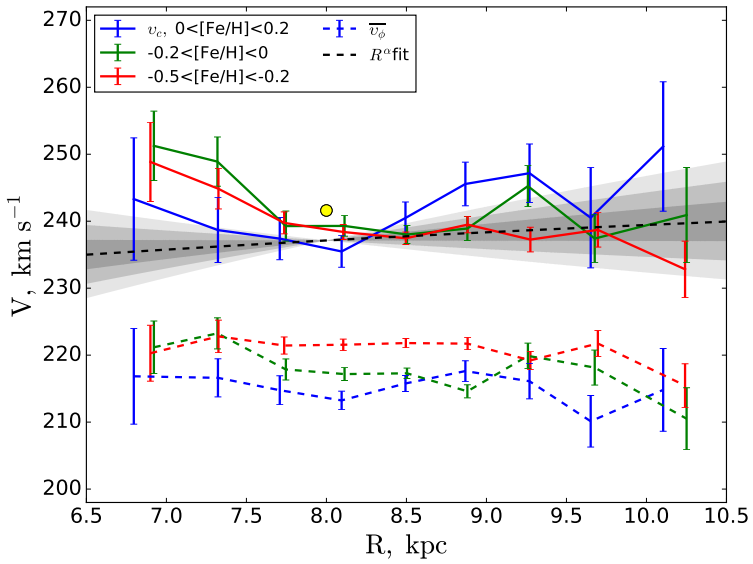

Figure 4.5: Rotation curve in the extended solar neighbourhood traced via SEGUE stars. The thin-disk stars are split into the same three metallicity bins as before. For each distance bin the mean rotation velocity $\overline{v_\phi} = v_\odot - \Delta V$ is measured (dashed curves, additional binning in $|z|$ applied in the range of $7\,\mathrm{kpc} < R < 9\,\mathrm{kpc}$ is not shown here). The circular velocity (solid curves) is calculated for the three metallicity bins. The best power-law fit of the form $v_c = v_0(R/R_0)^\alpha$ is shown with a black dashed line. The areas of the 1, 2 and 3σ-deviation are shown with increasingly lighter shades of grey. The solar tangential velocity $v_\odot$ is marked with a yellow circle.

$v_c(R)$. The iteration procedure converges very quickly, after two or three cycles.

We bin thin-disk SEGUE stars, again separated in three metallicities as before, in Galactocentric distances with equal step of 0.4 kpc. The further data analysis is not the same for all distance bins. As we mentioned above, the SEGUE stars are in general distributed over a large range in $|z|$, so we would like to take into account the vertical gradients in σ_R^2 and σ_z^2 by applying our equations separately at different heights for each distance. As one can see from the left panel of Figure 4.2, such $|z|$-binning for the thin disk sample is justified only close to R_0, approximately for $7\,\mathrm{kpc} < R < 9\,\mathrm{kpc}$, because at larger Galactocentric distances the majority of stars is located at approximately the same height, such that low-$|z|$ bins would be essentially empty and suffering from high Poisson noise. For this reason we do not bin in $|z|$ outside this distance range. Taking this into account, at $R < 7$ kpc and $R > 9$ kpc for each R-bin we find the mean tangential velocity $\overline{v_\phi}$ (dashed colour-coded lines in Figure 4.5), as well as three velocity dispersions and mean values of R and $|z|$. Then we apply the correction for the asymmetric drift from Eq. 4.28, which is typically ~ 20 km s^{-1}. For $7\,\mathrm{kpc} < R < 9\,\mathrm{kpc}$ we do the same, but separately for three vertical bins (as before, $|z|$ = 0-1.5 kpc with a step of 0.5 kpc), and then calculate the weighted mean v_c at each R. The obtained rotation curves representing different metallicity bins are shown as solid lines in Figure 4.5 and are broadly consistent with each other within the error bars.

Between 8 and 10 kpc the rotation curve is flat to an accuracy of a few kilometres per second, and definitely does not show the 10 km s^{-1} dip described by Sofue et al. (2009, 2010). On the other hand, the inner part of our rotation curve demonstrates a metallicity-dependent

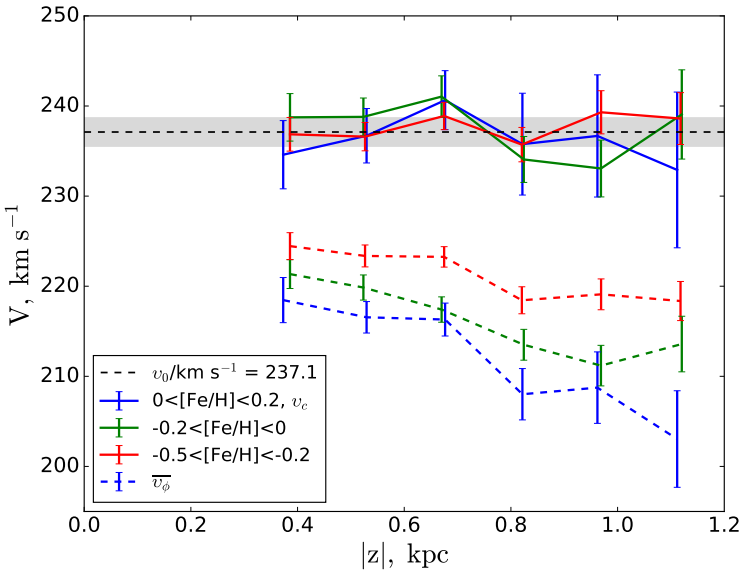

Figure 4.6: At this figure we plot Galactic rotation as a function of height. The vertical behaviour of the mean tangential velocity $\overline{v_\phi} = v_\odot - \Delta V$ (dashed lines) is compared to the circular speed $v_c = \overline{v_\phi} + V_a$ (solid lines) as derived from the tracer stars in a given $|z|$-bin. Colour coding represents the same metallicity ranges as before. Only stars with 7.5 kpc $< R <$ 8.5 kpc are considered. There is a clear negative trend with $|z|$ in $\overline{v_\phi}$, but in the circular speed, which is the tangential velocity corrected for the asymmetric drift including the vertical effects, it is not present any more. The least squares fit to the three v_c curves is shown as a dashed line and the 1-σ area is in grey, the corresponding circular velocity at the solar radius is $v_0 \approx 237$ km s^{-1}.

rise with the amplitude up to 10 km s^{-1}, similar to the one attested by Sofue et al. (2009, 2010).

We perform a power-law fit $V_c \propto R^\alpha$ simultaneously to all three rotation curves and find a small power law index $\alpha = 0.033 \pm 0.034$ (fit is shown in Figure 4.5 with a dashed line). This transforms into the local slope of the rotation curve $dV_c/dR = 0.98 \pm 1$ km s^{-1} kpc^{-1}. However, the existing measurements of the Oort constants point at a moderately negative slope: the classical value from Binney and Tremaine (2008) is $dV_c/dR = -2.4 \pm 1$ km s^{-1} kpc^{-1}, while the more recent study by Bovy (2017b) from TGAS data suggests an even steeper slope of -3.4 ± 0.6 km s^{-1} kpc^{-1}. Still, we must keep in mind that the Oort constants measure only a very local slope of the rotation curve, which may be strongly perturbed by the local spiral arm structure, while our analysis goes all the way to 1-2 kpc away from the Sun.

Figure 4.6 shows the total impact of the asymmetric drift correction on the mean tangential velocities at different $|z|$. The SEGUE thin-disk stars for 7.5 kpc $< R <$ 8.5 kpc were binned in height, and for each vertical bin the mean rotational velocity $\overline{v_\phi}$ and the circular speed v_c (circular speed in the plane as derived from the motion of stars at a given $|z|$) were calculated. The dashed curves representing $\overline{v_\phi}$ show a clear decrease in velocity with height. In contrast to this, the derived value for the rotation velocity does not show any trend with respect to $|z|$, as this quantity is already corrected for the asymmetric drift, which includes the vertical effects given by the tilt term and the vertical gradient of the radial force discussed before. The independence of the reconstructed v_c on the height $|z|$ of the tracer stars is a good justification of our method: regardless of the typical distances from the midplane of the different thin-disk

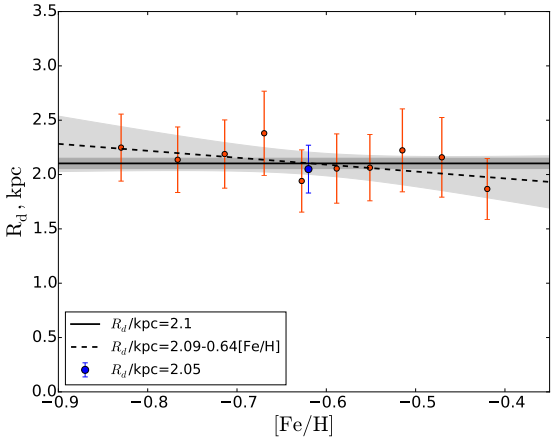

Figure 4.7: Radial scale length R_d of the thick disk versus metallicity. Considered are SEGUE thick-disk stars with 7.5 kpc < R < 8.5 kpc, 4 195 in total. Red points show the radial scale lengths calculated for each metallicity bin with the 'effective' quantities in Eq. 4.24. The points are fitted with a constant and also with R_d linearly dependent on [Fe/H] (solid and dashed lines). One-sigma areas are shown in grey. The blue point corresponds to the value of scale length derived in case of binning the same sample in 4 $|z|$-bins.

populations, their kinematics, when properly corrected for the asymmetric drift, must point to the same rotation velocity.

The thick-disk SEGUE stars are not very instrumental in reconstructing the rotation curve, as the radial scale length of the thick disk is poorly constrained. We can solve the inverse problem: use the data to reconstruct the radial scale length of the thick disk assuming the rotation curve already known. We express R_d from Eq. 4.23 and calculate it for ten metallicity bins of the thick disk. For the parameter $h_{v\sigma}$ of the thick disk we use a value of 800 pc, similar to its scale height (Just et al., 2011). Furthermore, we take only the local thick-disk sample with 7.5 kpc < R < 8.5 kpc in order to avoid regions, where our results can be biased by the uncertainty in the vertical correction term (this effect is not so important for the thin-disk sample, as its stars are in general located at smaller $|z|$ than those of the thick disk). The resulting R_d is shown in Figure 4.7 with red points. Though the data points show some small variation of R_d with [Fe/H], the constant value of the scale length 2.1 ± 0.05 kpc is more robust (see the darker one-sigma area in Figure 4.7). In other words, the chemically defined thick disk behaves as a single kinematically homogeneous population. The value of the thick disk scale length found here is consistent with simulations by Minchev et al. (2015) and with the data analysis by Bovy et al. (2012c, 2016b) and Kordopatis et al. (2017). When binning the local SEGUE thick-disk sample in metallicity, we calculate R_d for the 'effective' quantities in the bin: velocity dispersions determined for all stars and also mean $|z|$ and R. Such 'effective' values are quite representative in case of R and velocity dispersions, because our data are very local in terms of Galactocentric distances and expected to be kinematically homogeneous, so the velocity dispersions should not have a strong gradient in vertical direction. On the other hand, the mean value of $|z|$ might be misleading as the vertical distribution of stars is quite inhomogeneous. The vertical correction and the tilt term in V' (Eq. 4.24) are quite sensitive to z, so to cross-check our results we apply Eq. 4.23 for 4 $|z|$-bins (0-2 kpc with a 0.5 kpc step) with no binning in metallicity as the data are not abundant enough to allow a simultaneous separation in both $|z|$ and [Fe/H]. The resulting scale length, which is calculated again as a weighted mean of the values found for different $|z|$, deviates only slightly from the value found at the previous step: $R_d = 2.05 \pm 0.22$ kpc. We overplot it in Figure 4.7 with a blue dot for the mean metallicity of the local thick-disk sample. A good agreement between the values of scale length calculated via the different binning of our sample in the parameter space ensures us of the robustness of the derived result.

4.6 Discussion and conclusions

We performed the revision and improvement of the methods developed previously in Golubov et al. (2013). Starting from the classical Jeans analysis, we arrived at the new Strömberg relation for the asymmetric drift and applied it locally to the most recent RAVE data. This enabled us to update the value of the solar peculiar motion to $V_\odot = 4.47 \pm 0.8$ km s^{-1}. This is lower than the typical values reported by other authors, which are around 10-12 km s^{-1}. However, in the study of Sharma et al. (2014) also based on the RAVE data, though in the framework of a different Galaxy model, the solar peculiar velocity is smaller as well: $V_\odot = 7.62^{+0.13}_{-0.16}$ km s^{-1}. We also found radial scale lengths for the three metallicity populations, which are R_d(0<[Fe/H]<0.2) = 2.07 ± 0.2 kpc, R_d(-0.2<[Fe/H]<0) = 2.28 ± 0.26 kpc and R_d(-0.5<[Fe/H]<-0.2) = 3.05 ± 0.43 kpc. Our analysis demonstrates good consistency of the SEGUE and the RAVE data in terms of kinematics. With the peculiar velocity of the Sun derived from the RAVE sample, the SEGUE data give similar values for the scale lengths (see Table 4.3).

Subsequently, we used the SEGUE sample of the thin-disk G-dwarfs to reconstruct the rotation curve of the Milky Way, ranging from 7 to 10 kpc in Galactocentric radius. We took into account the asymmetric drift correction (Eq. 4.28) and showed that the resulting rotation curve is essentially flat (Figure 4.5). Thus, the existence of any features in the rotation curve just outside the solar radius is discarded in the framework of our analysis. The formal power-law fit to the rotation curve implies a positive slope $\alpha = 0.033 \pm 0.034$ consistent with a flat rotation curve, although we see that its local value is probably smaller. The corresponding radial gradient of the circular speed is $dV_c/dR = 0.98 \pm 1$ km s^{-1} kpc^{-1}, which is in agreement with the findings of Sharma et al. (2014), who derived a similar value from the RAVE data: $dV_c/dR = 0.67^{+0.25}_{-0.26}$ km s^{-1} kpc^{-1}.

Using SEGUE data and relying on the determined slope of the rotation curve, we also calculated the radial scale length of the thick disk. It is 2.05 ± 0.22 kpc, and no strong dependence on metallicity was observed. Values of the quantities derived in this chapter are summarised in Table 4.3.

Finally, we have to discuss the dependence of our results on the assumed constants and parameters. The pair $(R_0, v_\odot)$, on the one hand, influences the derived stellar spatial distribution and velocities from the observables. On the other hand, it enters the equation for the asymmetric drift correction (see Eq. 4.28). For the recommended values from Bland-Hawthorn and Gerhard (2016) $(R_0, v_\odot) = (8.2\text{kpc}, 248\text{kms}^{-1})$ the change in the re-calculated solar peculiar velocity and scale heights for the three metallicity bins lie well within one sigma, and the changes in the rotation curve can be mostly described in terms of a vertical shift to higher velocities and horizontal translation to larger Galactocentric distances; a slope of $\alpha = 0.024 \pm 0.031$ is found, which is again consistent with a flat rotation curve.

What is the impact of the solar peculiar motion? Changes of $(dU, dV, dW)_\odot$ add quadratically to the corresponding velocity dispersions. The vertical velocity has no other impact on the result, but we should check that the vertical component of the mean measured relative velocity of the stars in the sample is approximately $-W_\odot$, which is indeed the case. $U_\odot$ enters the velocity transformations to cylindrical coordinates, so every time we change $V_\odot$, R_0 or $v_\odot$, we have to adapt it to have $\overline{v_R} \approx 0$ as we assumed in Section 4.3. However, this correction is small and we can neglect it as it is surely beyond the accuracy we can hope to achieve in the framework of our approach. $V_\odot$ has a larger impact on the results as the asymmetric drift correction depends on it, mainly via v_c and the scale lengths (see Eq. 4.28). We test two values of $V_\odot$,

Quantity	from RAVE	from SEGUE
$V_\odot$ (km s^{-1})	4.47 ± 0.8	
$R_d^{\rm thin}$(0<[Fe/H]<0.2) (kpc)	2.07 ± 0.2	1.91 ± 0.23
$R_d^{\rm thin}$(-0.2<[Fe/H]<0) (kpc)	2.28 ± 0.26	2.51 ± 0.25
$R_d^{\rm thin}$(-0.5<[Fe/H]<-0.2) (kpc)	3.05 ± 0.43	3.55 ± 0.42
α		0.033 ± 0.034
$R_d^{\rm thick}$ (kpc)		2.05 ± 0.22

Table 4.3: The summary of the results.

~ 3 km s^{-1} (Golubov et al., 2013) and ~ 7.6 km s^{-1} (Sharma et al., 2014). The rotation curve slope is then $\alpha = 0.039 \pm 0.034$ and $\alpha = 0.014 \pm 0.028$, respectively. We also test the sensitivity of our results to the vertical scale heights $h_{v\sigma}$ as they are not tightly constrained. Changing $h_{v\sigma}$ by $\pm 20\%$ leads to the slopes of $\alpha = 0.022 \pm 0.03$ and $\alpha = 0.049 \pm 0.038$, which deviate from our standard value by less than 0.5σ.

To quantify the vertical gradient of the radial force term we assume a Galaxy model, i.e., use some form of the potential as an input. However, we believe that the rotation curve obtained in Section 4.5 is not strongly predefined by this choice. The $RF(R,z)$ term is not a dominating one in the asymmetric drift correction, so with respect to the rotation velocity it is a first-order correction. The modification of the potential will enter v_c as a second-order correction only, and this already meets the limit of our accuracy. As we have shown in Section 4.3, the main contribution to the vertical correction of the radial force comes from the thin disk, thus its scale length and scale height are the main sources of uncertainty in this term. Taking a R_d value of 2 kpc or 3 kpc we arrive at a rotation curve, which is correspondingly slightly steeper ($\alpha = 0.041 \pm 0.041$) or flatter ($\alpha = 0.027 \pm 0.029$) than the one we presented in Figure 4.5.Testing h_z of 200 pc and 400 pc results in similar changes: $\alpha = 0.041 \pm 0.036$ and $\alpha = 0.026 \pm 0.03$. The impact of varying R_d and h_z of the other disks is negligible.

None of these deviations from our main result produce essential changes in the derived rotation curve shape. So we can conclude that in the framework of the developed analysis our outcome is robust with respect to the small changes of our constants and the pre-choice of the Galactic potential. Our analysis of the local rotation curve does not support the existence of any special features in its shape like a significant dip at R = 9 kpc.

5 Summary

In this work we performed a simple generalisation of the Just-Jahreriß model focusing on the Milky Way thin disk (Just and Jahreiß, 2010; Just et al., 2011): we predict the spatial structure and kinematics of the disk in the range of Galactocentric distances of 4-12 kpc with a step of 1 kpc. We used exponential radial profiles for the gas, thin, and thick disks and added the dark matter (DM) halo as an isothermal sphere in the thin-disk approximation. To simulate the inside-out growth of the thin disk, we assumed the star formation rate (SFR) with a peak shifting towards older ages with decrease of Galactocentric distance and a universal four-slope broken power-law initial mass function (IMF, Rybizki and Just, 2015; Rybizki, 2018). Under the assumption of a constant thickness of the disk, we determined the age-velocity dispersion relation (AVR) self-consistently at each radius. Basing on the predicted age distributions of the thin disk populations for Galactocentric distances of 6-12 kpc, we determined the age-metallicity relation (AMR) constrained by the metallicity distributions of stars from the Apache Point Observatory Galactic Evolution Experiment (APOGEE, Eisenstein et al., 2011) red clump (RC) catalogue (Bovy et al., 2014). We test two sets of the SFR parameters corresponding to the different disk formation scenarios and explore the sensitivity of the model predictions to the assumed SFR. We find that the inside-out growth and the constant disk thickness are sufficient assumptions to produce flaring of the mono-age populations increasing with the stellar age. The radial surface density profiles of the mono-abundance populations (MAPs) show less prominent flaring and are characterised by non-monotonic surface density profiles with a peak at Galactocentric distance R_{peak} and decline at the both sides from the peak. The position of R_{peak} shifts to the outer disk with decrease of metallicity. The structural properties of the disk as predicted in a framework of the generalised, though not yet calibrated, JJ model demonstrate a good agreement with other studies, both numerical and observational ones (Minchev et al., 2015, 2017; Bovy et al., 2016b).

At the next step we validated our fiducial local model with the high-quality samples of the first and second Gaia data releases (DR1 and DR2, Gaia Collaboration et al., 2016a, 2018). By applying a forward modelling, we compared the mock stellar populations, as generated with the full stellar evolution included from the MESA Isochrones and Stellar Tracks (MIST, Choi et al., 2016), to the thin-disk sample in the local solar cylinder of 300 pc radius and 1 kpc height below the Galactic plane. We used the data from the Tycho-Gaia Astrometric Solution (TGAS, Michalik et al., 2015; Lindegren et al., 2016) catalogue of the Gaia DR1 cross-matched with the fifth release of the Radial Velocity Experiment (RAVE DR5, Kunder et al., 2017). The vertical density profiles predicted for the upper- and lower main sequence (UMS and LMS, respectively), as well as for the red giant branch (RGB) stars, showed a good agreement with the data. The overall underestimation of the number of stars in the sample is 7.8%, the corresponding stellar deficit in the model identified for the UMS, LMS, and RGB stars are 3.6%,

6%, and 34.7%, respectively. We also found a 10%-uncertainty related to the choice of stellar isochrones. The vertical velocity distribution function f($|W|$) simulated for the whole cylinder is within 1σ agreement with the data for almost all $|W|$. The marginal agreement between the data and model is identified for the near-plane dynamically cold populations, $|z| < 100$ pc. We also found that the model gives a fully realistic representation of the vertical gradient in stellar populations when studied with Hess diagrams for different horizontal slices. Several additional tests performed with the Gaia×RAVE data, and also with the Gaia DR2 F stars, G and K dwarfs, confirm our results obtained from analysis of Gaia DR1. The near-plane discrepancy in the velocity distribution function f($|W|$) and the model deviations from the observed vertical number density profile of the G-dwarfs indicate that the shape of the vertical gravitational potential needs to be adapted to match the new astrometric data. Taking into account that the the overall inconsistency in the stellar number in Gaia DR2 tests is of the order of a few percents only, the task of the model recalibration is a nontrivial one.

Additionally, we investigated the shape of the rotation curve in the extended solar neighbourhood at R = 7-10 kpc in order to check for a presence of any peculiarities in the Galactic rotation just outside the solar radius as has been reported in Sofue et al. (2009). For this we used the G-dwarf stars from the Sloan Extension for Galactic Understanding and Exploration (SEGUE, Yanny et al., 2009). Following the formalism from Golubov et al. (2013), we developed a modified Strömberg relation as a tool for the robust treatment of the asymmetric drift and applied it to the three different metallicity populations of the local sample from the RAVE DR5. This allowed us to determine simultaneously the V-component of the solar peculiar velocity and the radial scale lengths for the three kinemaically different populations representing the Galactic thin disk. The tangential component of the solar peculiar velocity is found to be $V_\odot = 4.47 \pm 0.8$ km s^{-1} and the corresponding scale lengths determined with the SEGUE data are R_d(0<[Fe/H]<0.2) = 1.91 ± 0.23 kpc, R_d(-0.2<[Fe/H]<0) = 2.51 ± 0.25 kpc and R_d(-0.5<[Fe/H]<-0.2) = 3.55 ± 0.42 kpc. Then applying our asymmetric drift correction separately to the different metallicity bins of the SEGUE G-dwarf sample, we reconstructed the rotation curve in the extended solar neighbourhood. We approached this problem in a framework of classical Jeans analysis and derived the circular velocity by correcting the mean tangential velocity for the asymmetric drift in each distance bin. We found that in the range of assumed Galactocentric distances the shape of the rotation curve is essentially flat, which is consistent with the accurate measurements of parallaxes and proper motions of ~ 100 masers with a very long baseline interferometry (VLBI) (Reid et al., 2014). The inferred power law index of the rotation curve is 0.033 ± 0.034, which corresponds to a local slope of $dV_c/dR = 0.98 \pm 1$ km s^{-1} kpc^{-1}. In this respect, the local kinematics of the thin disk rotation as determined in the framework of our new careful analysis does not favour the presence of a massive overdensity ring just outside the solar radius. With SEGUE data we also calculated the radial scale length of the thick disk taking as known the derived peculiar motion of the Sun and the slope of the rotation curve. The obtained value is 2.05 kpc with no essential dependence on metallicity.

6 Perspectives

We can outline several directions of the future work which can be considered as a natural continuation of the research presented in this thesis. Generally, the future work will be aimed on the further improvement and sophistication of the chemo-dynamical Just-Jahreiß model of the Milky Way disk (JJ model, Just and Jahreiß, 2010; Just et al., 2011).

As we demonstrated in Chapter 3, the model parameters require adaptation in order to match the newest astrometric and spectroscopic observations from the second Gaia data release (DR2, Gaia Collaboration et al., 2018). Thus, one of the next steps will include the model calibration against the Gaia data. At the same time, there are several potential drawbacks of the present-day version of the model which we briefly mentioned throughout this work. One of them is a simplified treatment of the thick disk which is now believed to be a composite Galactic component, similar to the thin disk though in general older and more dynamically heated, rather than a mono-age population born in a single burst of star formation. The chemical evolution code Chempy, taking the star formation rate (SFR) and initial mass function (IMF) as input functions, can reconstruct the gas infall history and enrichment in different elements using the observational chemical abundances as a constrain. By combing the predictions of Chempy with our radially dependent SFR and the data from the extensive and high-resolution spectroscopic surveys such as GALactic Archaeology with HERMES (GALAH, Martell et al., 2017), we will be able to test different sets of model parameters; the detailed investigation of the chemical abundance plane will be also possible, which will help us to improve the thick disk definition.

Another issue is related to a lack of stellar radial migration in our model. The importance of the radial migration still remains hotly debated, such that quite different and sometimes contradictory statements can be found in the literature. As estimated from the N-body simulations of the Milky Way-like galaxies, the effect of radial migration can significantly change the vertical structure of migrated stars (Vera-Ciro et al., 2016). The authors of Halle et al. (2015) point out that the main contribution to the radial migration comes from the blurring of orbits, and some models assume a simple parametrisation for the radial migration mechanisms (Kubryk et al., 2015); a similar treatment can be also added to our model in the future.

Finally, the recipes for the radial and tangential stellar velocity components should be added to the JJ model, such that it will be able to predict the full three-dimensional (3D) kinematics of stars. Our treatment of the asymmetric drift developed in Chapter 4 is highly useful for this task and can be used as a starting point for the future work aimed on extension of the model to the full 3D velocity space.

List of publications

Referenced:

1. Y. Shkuratov, V. Kaydash, X. Sysolyatina, A. Razim, and G. Videen. Lunar surface traces of engine jets of Soviet sample return probes: The enigma of the Luna-23 and Luna-24 landing sites. *Planet. Space Sci.*, 75:28–36, January 2013. doi:10.1016/j.pss.2012.10.016.
2. A. Just, K. Sysoliatina, and I. Koutsouridou. The evolution history of the extended solar neighbourhood. In A. Recio-Blanco, P. de Laverny, A. G. A.Brown, and T. Prusti, editors, *IAU Symposium*, volume 330 of *IAU Symposium*, pages 168–171, April 2018. doi: 10.1017/S1743921317006299.
3. K. Sysoliatina, A. Just, O. Golubov, Q. A. Parker, E. K. Grebel, G. Kordopatis, T. Zwitter, J. Bland-Hawthorn, B. K. Gibson, A. Kunder, U. Munari, J. Navarro, W. Reid, G. Seabroke, M. Steinmetz, and F. Watson. The local rotation curve of the Milky Way based on SEGUE and RAVE data. *A&A*, 614: A63, June 2018. doi: 10.1051/0004-6361/201731143.
4. K. Sysoliatina, A. Just, I. Koutsouridou, E. K. Grebel, G. Kordopatis, M. Steinmetz, O. Bienaymé, B. K. Gibson, J. Navarro, W. Reid, and G. Seabroke. Local disc model in view of Gaia DR1 and RAVE data. 2018, ArXiv e-prints, `[arXiv:1810.00814]`. Accepted for publication in *A&A*.

Non-referenced:

1. K. Sysoliatina, A. Razim, V. Kaydash, Y. Shkuratov, G. Videen, Lunar opposition effect as inferred from high resolution LRO camera data , The 45th Lunar and Planetary Science Conference (2014), Abstract No. 1757.
2. Sysoliatina K.V., Lunar surface opposition effect as inferred from LRO spacecraft data, IX Regional Scientific Astronomical Conference for pupils and students Thesis, 2014 (in Russian).
3. Sysoliatina K.V., Lunar surface opposition effect as inferred from LRO spacecraft data, Student Scientific Conference “Physics and Technological Development” Thesis, 2014 (in Russian).

Bibliography

M. G. Abadi, J. F. Navarro, M. Steinmetz, and V. R. Eke. Simulations of Galaxy Formation in a Λ Cold Dark Matter Universe. I. Dynamical and Photometric Properties of a Simulated Disk Galaxy. *ApJ*, 591:499–514, July 2003. doi: 10.1086/375512.

D. S. Aguado, J. I. González Hernández, C. Allende Prieto, and R. Rebolo. J0815+4729: A Chemically Primitive Dwarf Star in the Galactic Halo Observed with Gran Telescopio Canarias. *ApJ*, 852:L20, January 2018. doi: 10.3847/2041-8213/aaa23a.

F. Arenou, X. Luri, C. Babusiaux, et al. Gaia Data Release 2. Catalogue validation. *A&A*, 616: A17, August 2018. doi: 10.1051/0004-6361/201833234.

D. Argast, M. Samland, O. E. Gerhard, and F.-K. Thielemann. Metal-poor halo stars as tracers of ISM mixing processes during halo formation. *A&A*, 356:873–887, April 2000.

T. L. Astraatmadja and C. A. L. Bailer-Jones. Estimating Distances from Parallaxes. III. Distances of Two Million Stars in the Gaia DR1 Catalogue. *ApJ*, 833:119, December 2016. doi: 10.3847/1538-4357/833/1/119.

R. Bacon, M. Accardo, L. Adjali, et al. The MUSE second-generation VLT instrument. In *Ground-based and Airborne Instrumentation for Astronomy III*, volume 7735 of *Proc. SPIE*, page 773508, July 2010. doi: 10.1117/12.856027.

J. N. Bahcall. Self-consistent determinations of the total amount of matter near the sun. *ApJ*, 276:169–181, January 1984a. doi: 10.1086/161601.

J. N. Bahcall. The distribution of stars perpendicular to galactic disk. *ApJ*, 276:156–168, January 1984b. doi: 10.1086/161600.

C. A. L. Bailer-Jones. Estimating Distances from Parallaxes. *PASP*, 127:994, October 2015. doi: 10.1086/683116.

C. A. L. Bailer-Jones, J. Rybizki, M. Fouesneau, G. Mantelet, and R. Andrae. Estimating Distance from Parallaxes. IV. Distances to 1.33 Billion Stars in Gaia Data Release 2. *AJ*, 156:58, August 2018. doi: 10.3847/1538-3881/aacb21.

D. P. Bennett, C. Alcock, R. A. Allsman, et al. Recent developments in gravitational microlensing and the latest MACHO results: Microlensing towards the galactic bulge. In S. S. Holt and C. L. Bennett, editors, *Dark Matter*, volume 336 of *American Institute of Physics Conference Series*, pages 77–90, July 1995. doi: 10.1063/1.48390.

T. Bensby, A. Alves-Brito, M. S. Oey, D. Yong, and J. Meléndez. A First Constraint on the

Thick Disk Scale Length: Differential Radial Abundances in K Giants at Galactocentric Radii 4, 8, and 12 kpc. *ApJ*, 735:L46, July 2011. doi: 10.1088/2041-8205/735/2/L46.

T. Bensby, S. Feltzing, A. Gould, et al. Chemical evolution of the Galactic bulge as traced by microlensed dwarf and subgiant stars. VI. Age and abundance structure of the stellar populations in the central sub-kpc of the Milky Way. *A&A*, 605:A89, September 2017. doi: 10.1051/0004-6361/201730560.

R. Berendzen and M. Hoskin. Hubble's Announcement of Cepheids in Spiral Nebulae. *Leaflet of the Astronomical Society of the Pacific*, 10:425–440, June 1971.

R. Bien, T. Brandt, and A. Just. Simulating sinking satellites with superbox-10. *MNRAS*, 428: 1631–1642, January 2013. doi: 10.1093/mnras/sts141.

J. Binney. More dynamical models of our Galaxy. *MNRAS*, 426:1328–1337, October 2012. doi: 10.1111/j.1365-2966.2012.21692.x.

J. Binney and T. Piffl. The distribution function of the Galaxy's dark halo. *MNRAS*, 454: 3653–3663, December 2015. doi: 10.1093/mnras/stv2225.

J. Binney and S. Tremaine. *Galactic Dynamics*. Princeton Univ. Press, 2008.

J. Binney, B. Burnett, G. Kordopatis, et al. Galactic kinematics and dynamics from Radial Velocity Experiment stars. *MNRAS*, 439:1231–1244, April 2014. doi: 10.1093/mnras/stt2367.

J. C. Bird, S. Kazantzidis, D. H. Weinberg, et al. Inside out and Upside down: Tracing the Assembly of a Simulated Disk Galaxy Using Mono-age Stellar Populations. *ApJ*, 773:43, August 2013. doi: 10.1088/0004-637X/773/1/43.

D. Bizyaev and S. Mitronova. Photometric parameters of edge-on galaxies from 2MASS observations. *A&A*, 389:795–801, July 2002. doi: 10.1051/0004-6361:20020633.

J. Bland-Hawthorn and O. Gerhard. The Galaxy in Context: Structural, Kinematic, and Integrated Properties. *ARA&A*, 54:529–596, September 2016. doi: 10.1146/annurev-astro-081915-023441.

I. A. Bond, F. Abe, R. J. Dodd, et al. Real-time difference imaging analysis of MOA Galactic bulge observations during 2000. *MNRAS*, 327:868–880, November 2001. doi: 10.1046/j.1365-8711.2001.04776.x.

F. Bournaud, B. G. Elmegreen, and M. Martig. The Thick Disks of Spiral Galaxies as Relics from Gas-rich, Turbulent, Clumpy Disks at High Redshift. *ApJ*, 707:L1–L5, December 2009. doi: 10.1088/0004-637X/707/1/L1.

J. Bovy. Stellar inventory of the solar neighbourhood using Gaia DR1. *MNRAS*, 470:1360–1387, September 2017a. doi: 10.1093/mnras/stx1277.

J. Bovy. Galactic rotation in Gaia DR1. *MNRAS*, 468:L63–L67, June 2017b. doi: 10.1093/mnrasl/slx027.

J. Bovy, C. Allende Prieto, T. C. Beers, et al. The Milky Way's Circular-velocity Curve between 4 and 14 kpc from APOGEE data. *ApJ*, 759:131, November 2012a. doi: 10.1088/0004-637X/759/2/131.

J. Bovy, H.-W. Rix, and D. W. Hogg. The Milky Way Has No Distinct Thick Disk. *ApJ*, 751: 131, June 2012b. doi: 10.1088/0004-637X/751/2/131.

J. Bovy, H.-W. Rix, C. Liu, et al. The Spatial Structure of Mono-abundance Sub-populations of the Milky Way Disk. *ApJ*, 753:148, July 2012c. doi: 10.1088/0004-637X/753/2/148.

J. Bovy, D. L. Nidever, H.-W. Rix, et al. The APOGEE Red-clump Catalog: Precise Distances, Velocities, and High-resolution Elemental Abundances over a Large Area of the Milky Way's Disk. *ApJ*, 790:127, August 2014. doi: 10.1088/0004-637X/790/2/127.

J. Bovy, H.-W. Rix, G. M. Green, E. F. Schlafly, and D. P. Finkbeiner. On Galactic Density Modeling in the Presence of Dust Extinction. *ApJ*, 818:130, February 2016a. doi: 10.3847/0004-637X/818/2/130.

J. Bovy, H.-W. Rix, E. F. Schlafly, et al. The Stellar Population Structure of the Galactic Disk. *ApJ*, 823:30, May 2016b. doi: 10.3847/0004-637X/823/1/30.

A. Bressan, P. Marigo, L. Girardi, et al. PARSEC: stellar tracks and isochrones with the PAdova and TRieste Stellar Evolution Code. *MNRAS*, 427:127–145, November 2012. doi: 10.1111/j.1365-2966.2012.21948.x.

B. C. Bromley, S. J. Kenyon, M. J. Geller, and W. R. Brown. Binary Disruption by Massive Black Holes: Hypervelocity Stars, S Stars, and Tidal Disruption Events. *ApJ*, 749:L42, April 2012. doi: 10.1088/2041-8205/749/2/L42.

C. B. Brook, D. Kawata, B. K. Gibson, and K. C. Freeman. The Emergence of the Thick Disk in a Cold Dark Matter Universe. *ApJ*, 612:894–899, September 2004. doi: 10.1086/422709.

D. Burstein. Structure and origin of S0 galaxies. III - The luminosity distribution perpendicular to the plane of the disks in S0's. *ApJ*, 234:829–836, December 1979. doi: 10.1086/157563.

L. Capitanio, R. Lallement, J. L. Vergely, M. Elyajouri, and A. Monreal-Ibero. Three-dimensional mapping of the local interstellar medium with composite data. *A&A*, 606:A65, October 2017. doi: 10.1051/0004-6361/201730831.

J. M. Carrasco, D. W. Evans, P. Montegriffo, et al. Gaia Data Release 1. Principles of the photometric calibration of the G band. *A&A*, 595:A7, November 2016. doi: 10.1051/0004-6361/201629235.

L. Casagrande, R. Schönrich, M. Asplund, et al. New constraints on the chemical evolution of the solar neighbourhood and Galactic disc(s). Improved astrophysical parameters for the Geneva-Copenhagen Survey. *A&A*, 530:A138, June 2011. doi: 10.1051/0004-6361/201016276.

L. Chemin, F. Renaud, and C. Soubiran. Incorrect rotation curve of the Milky Way. *A&A*, 578: A14, June 2015. doi: 10.1051/0004-6361/201526040.

L. Chemin, J.-M. Huré, C. Soubiran, et al. Asymmetric mass models of disk galaxies. I. Messier 99. *A&A*, 588:A48, April 2016. doi: 10.1051/0004-6361/201527730.

B. Chen, X. Liu, M. Xiang, et al. The LAMOST Spectroscopic Survey of Star Clusters in M31. II. Metallicities, Ages, and Masses. *AJ*, 152:45, August 2016. doi: 10.3847/0004-6256/152/2/45.

J. Y. Cheng, C. M. Rockosi, H. L. Morrison, et al. Abundance Trends in the Milky Way Disk as Observed by SEGUE. In W. Aoki, M. Ishigaki, T. Suda, T. Tsujimoto, and N. Arimoto, editors, *Galactic Archaeology: Near-Field Cosmology and the Formation of the Milky Way*, volume 458 of *Astronomical Society of the Pacific Conference Series*, page 105, August 2012.

J. Choi, A. Dotter, C. Conroy, et al. Mesa Isochrones and Stellar Tracks (MIST). I. Solar-scaled Models. *ApJ*, 823:102, June 2016. doi: 10.3847/0004-637X/823/2/102.

E. Churchwell, B. L. Babler, M. R. Meade, et al. The Spitzer/GLIMPSE Surveys: A New View of the Milky Way. *PASP*, 121:213, March 2009. doi: 10.1086/597811.

D. R. Cole and J. Binney. A centrally heated dark halo for our Galaxy. *MNRAS*, 465:798–810, February 2017. doi: 10.1093/mnras/stw2775.

F. Combes and R. H. Sanders. Formation and properties of persisting stellar bars. *A&A*, 96: 164–173, March 1981.

M. A. Czekaj, A. C. Robin, F. Figueras, X. Luri, and M. Haywood. The Besançon Galaxy model renewed. I. Constraints on the local star formation history from Tycho data. *A&A*, 564:A102, April 2014. doi: 10.1051/0004-6361/201322139.

T. M. Dame and P. Thaddeus. A Large Extension of the CfA Galactic CO Survey. In D. Clemens, R. Shah, and T. Brainerd, editors, *Milky Way Surveys: The Structure and Evolution of our Galaxy*, volume 317 of *Astronomical Society of the Pacific Conference Series*, page 66, December 2004.

T. M. Dame, D. Hartmann, and P. Thaddeus. The Milky Way in Molecular Clouds: A New Complete CO Survey. *ApJ*, 547:792–813, February 2001. doi: 10.1086/318388.

G. de Vaucouleurs. Classification and Morphology of External Galaxies. *Handbuch der Physik*, 53:275, 1959.

A. J. Deason, V. Belokurov, and N. W. Evans. The Milky Way stellar halo out to 40 kpc: squashed, broken but smooth. *MNRAS*, 416:2903–2915, October 2011. doi: 10.1111/j.1365-2966.2011.19237.x.

W. Dehnen. The Effect of the Outer Lindblad Resonance of the Galactic Bar on the Local Stellar Velocity Distribution. *AJ*, 119:800–812, February 2000. doi: 10.1086/301226.

W. Dehnen and J. Binney. Mass models of the Milky Way. *MNRAS*, 294:429, March 1998a. doi: 10.1046/j.1365-8711.1998.01282.x.

W. Dehnen and J. J. Binney. Local stellar kinematics from HIPPARCOS data. *MNRAS*, 298: 387–394, August 1998b. doi: 10.1046/j.1365-8711.1998.01600.x.

P. Di Matteo, M. Haywood, A. Gómez, et al. Mapping a stellar disk into a boxy bulge: The outside-in part of the Milky Way bulge formation. *A&A*, 567:A122, July 2014. doi: 10.1051/0004-6361/201322958.

R. H. Dicke, P. J. E. Peebles, P. G. Roll, and D. T. Wilkinson. Cosmic Black-Body Radiation. *ApJ*, 142:414–419, July 1965. doi: 10.1086/148306.

C. Dobbs and J. Baba. Dawes Review 4: Spiral Structures in Disc Galaxies. *PASA*, 31:e035, September 2014. doi: 10.1017/pasa.2014.31.

A. Dotter. MESA Isochrones and Stellar Tracks (MIST) 0: Methods for the Construction of Stellar Isochrones. *APJS*, 222:8, January 2016. doi: 10.3847/0067-0049/222/1/8.

R. Drimmel and D. N. Spergel. Three-dimensional Structure of the Milky Way Disk: The Distribution of Stars and Dust beyond 0.35 R_{solar}. *ApJ*, 556:181–202, July 2001. doi: 10.1086/321556.

R. Drimmel, A. Cabrera-Lavers, and M. López-Corredoira. A three-dimensional Galactic extinction model. *A&A*, 409:205–215, October 2003. doi: 10.1051/0004-6361:20031070.

E. Dwek, R. G. Arendt, M. G. Hauser, et al. Morphology, near-infrared luminosity, and mass of the Galactic bulge from COBE DIRBE observations. *ApJ*, 445:716–730, June 1995. doi: 10.1086/175734.

D. J. Eisenstein, D. H. Weinberg, E. Agol, et al. SDSS-III: Massive Spectroscopic Surveys of the Distant Universe, the Milky Way, and Extra-Solar Planetary Systems. *AJ*, 142:72, September 2011. doi: 10.1088/0004-6256/142/3/72.

B. G. Elmegreen, F. Bournaud, and D. M. Elmegreen. Bulge Formation by the Coalescence of Giant Clumps in Primordial Disk Galaxies. *ApJ*, 688:67–77, November 2008. doi: 10.1086/592190.

B. Famaey, G. Monari, and A. Siebert. The Milky Way disk non-axisymmetries and galactoseismology. *Astronomische Nachrichten*, 337:949, September 2016. doi: 10.1002/asna.201612405.

K. C. Freeman. The Galactic spheroid and old disk. *ARA&A*, 25:603–632, 1987. doi: 10.1146/annurev.aa.25.090187.003131.

Gaia Collaboration, A. G. A. Brown, A. Vallenari, et al. Gaia Data Release 1. Summary of the astrometric, photometric, and survey properties. *A&A*, 595:A2, November 2016a. doi: 10.1051/0004-6361/201629512.

Gaia Collaboration, T. Prusti, J. H. J. de Bruijne, et al. The Gaia mission. *A&A*, 595:A1, November 2016b. doi: 10.1051/0004-6361/201629272.

Gaia Collaboration, A. G. A. Brown, A. Vallenari, et al. Gaia Data Release 2. Summary of the contents and survey properties. *A&A*, 616:A1, August 2018. doi: 10.1051/0004-6361/201833051.

G. Gamov. Concerning the Origin of Chemical Elements. *J. Wash. Acad. Sci.*, 32:353, December 1942.

G. Gamov. Expanding Universe and the Origin of Elements. *Phys. Rev.*, 70:572, September 1946.

S. Gao, A. Just, and E. K. Grebel. Detailed comparison of Milky Way models based on stellar population synthesis and SDSS star counts at the north Galactic pole. *A&A*, 549:A20, January 2013. doi: 10.1051/0004-6361/201118243.

B. Garilli, L. Guzzo, M. Scodeggio, et al. The VIMOS Public Extragalactic Survey (VIPERS). First Data Release of 57 204 spectroscopic measurements. *A&A*, 562:A23, February 2014. doi: 10.1051/0004-6361/201322790.

B.K. Gier. Chemical Evolution of the Solar Neighborhood in the Framework of a Dynamical Disk Model. Master's thesis, The University of Heidelberg, Germany, 2016.

S. Gillessen, F. Eisenhauer, T. K. Fritz, et al. The Orbit of the Star S2 Around SGR A* from Very Large Telescope and Keck Data. *ApJ*, 707:L114–L117, December 2009. doi: 10.1088/0004-637X/707/2/L114.

S. Gillessen, P. M. Plewa, F. Eisenhauer, et al. An Update on Monitoring Stellar Orbits in the Galactic Center. *ApJ*, 837:30, March 2017. doi: 10.3847/1538-4357/aa5c41.

G. Gilmore and N. Reid. New light on faint stars. III - Galactic structure towards the South Pole and the Galactic thick disc. *MNRAS*, 202:1025–1047, March 1983. doi: 10.1093/mnras/202.4.1025.

G. Gilmore, S. Randich, M. Asplund, et al. The Gaia-ESO Public Spectroscopic Survey. *The Messenger*, 147:25–31, March 2012.

L. Girardi. Milky Way populations with TRILEGAL. *Astronomische Nachrichten*, 337:871, September 2016. doi: 10.1002/asna.201612388.

L. Girardi, M. A. T. Groenewegen, E. Hatziminaoglou, and L. da Costa. Star counts in the Galaxy. Simulating from very deep to very shallow photometric surveys with the TRILEGAL code. *A&A*, 436:895–915, June 2005. doi: 10.1051/0004-6361:20042352.

S. N. Goderya and S. M. Lolling. Morphological Classification of Galaxies using Computer Vision and Artificial Neural Networks: A Computational Scheme. *Ap&SS*, 279:377–387, 2002. doi: 10.1023/A:1015193432240.

O. Golubov, A. Just, O. Bienaymé, et al. The asymmetric drift, the local standard of rest, and implications from RAVE data. *A&A*, 557:A92, September 2013. doi: 10.1051/0004-6361/201321559.

R. J. Gould and E. E. Salpeter. The Interstellar Abundance of the Hydrogen Molecule. I. Basic Processes. *ApJ*, 138:393, August 1963. doi: 10.1086/147654.

G. M. Green, E. F. Schlafly, D. P. Finkbeiner, et al. A Three-dimensional Map of Milky Way Dust. *ApJ*, 810:25, September 2015. doi: 10.1088/0004-637X/810/1/25.

G. M. Green, E. F. Schlafly, D. Finkbeiner, et al. Galactic reddening in 3D from stellar photometry - an improved map. *MNRAS*, 478:651–666, July 2018. doi: 10.1093/mnras/sty1008.

V. Grisoni, E. Spitoni, F. Matteucci, et al. The AMBRE project: chemical evolution models for the Milky Way thick and thin discs. *MNRAS*, 472:3637–3647, December 2017. doi: 10.1093/mnras/stx2201.

V. Grisoni, E. Spitoni, and F. Matteucci. Abundance gradients along the Galactic disc from chemical evolution models. *MNRAS*, September 2018. doi: 10.1093/mnras/sty2444.

A. Halle, P. Di Matteo, M. Haywood, and F. Combes. Quantifying stellar radial migration in an N-body simulation: blurring, churning, and the outer regions of galaxy discs. *A&A*, 578: A58, June 2015. doi: 10.1051/0004-6361/201525612.

M. R. Hayden, A. Recio-Blanco, P. de Laverny, S. Mikolaitis, and C. C. Worley. The AMBRE project: The thick thin disk and thin thick disk of the Milky Way. *A&A*, 608:L1, November 2017. doi: 10.1051/0004-6361/201731494.

M. Haywood, P. Di Matteo, M. D. Lehnert, D. Katz, and A. Gómez. The age structure of stellar populations in the solar vicinity. Clues of a two-phase formation history of the Milky Way disk. *A&A*, 560:A109, December 2013. doi: 10.1051/0004-6361/201321397.

A. A. Henden, D. L. Welch, D. Terrell, and S. E. Levine. The AAVSO Photometric All-Sky Survey (APASS). In *American Astronomical Society Meeting Abstracts #214*, volume 214 of *American Astronomical Society Meeting Abstracts*, page 669, May 2009.

M. Heyer and T. M. Dame. Molecular Clouds in the Milky Way. *ARA&A*, 53:583–629, August 2015. doi: 10.1146/annurev-astro-082214-122324.

J. G. Hills. Hyper-velocity and tidal stars from binaries disrupted by a massive Galactic black hole. *Nature*, 331:687–689, February 1988. doi: 10.1038/331687a0.

A. Hocking, J. E. Geach, Y. Sun, and N. Davey. An automatic taxonomy of galaxy morphology using unsupervised machine learning. *MNRAS*, 473:1108–1129, January 2018. doi: 10.1093/mnras/stx2351.

E. Høg, C. Fabricius, V. V. Makarov, et al. The Tycho-2 catalogue of the 2.5 million brightest stars. *A&A*, 355:L27–L30, March 2000.

D. Hollenbach and E. E. Salpeter. Surface Recombination of Hydrogen Molecules. *ApJ*, 163: 155, January 1971. doi: 10.1086/150754.

J. Holmberg and C. Flynn. The local density of matter mapped by Hipparcos. *MNRAS*, 313: 209–216, April 2000. doi: 10.1046/j.1365-8711.2000.02905.x.

L. G. Hou and J. L. Han. Offset between stellar spiral arms and gas arms of the Milky Way. *MNRAS*, 454:626–636, November 2015. doi: 10.1093/mnras/stv1904.

C. D. Howard, R. M. Rich, W. Clarkson, et al. Kinematics at the Edge of the Galactic Bulge: Evidence for Cylindrical Rotation. *ApJ*, 702:L153–L157, September 2009. doi: 10.1088/0004-637X/702/2/L153.

P.-Y. Hsieh, P. M. Koch, P. T. P. Ho, et al. Molecular Gas Feeding the Circumnuclear Disk of the Galactic Center. *ApJ*, 847:3, September 2017. doi: 10.3847/1538-4357/aa8329.

Y. Huang, X.-W. Liu, H.-B. Yuan, et al. The Milky Way's rotation curve out to 100 kpc and its constraint on the Galactic mass distribution. *MNRAS*, 463:2623–2639, December 2016. doi: 10.1093/mnras/stw2096.

H. Jahreiß and R Wielen. In *Battrick B., Perryman M. A. C., Bernacca P. L., eds, ESA SP-402: HIPPARCOS '97. Presentation of the Hipparcos and Tycho Catalogues and the First Astrophysical Results of the Hipparcos Space Astrometry Mission. ESA*, page p. 675, Noordwijk, November 1997.

C. Jordi, M. Gebran, J. M. Carrasco, et al. Gaia broad band photometry. *A&A*, 523:A48, November 2010. doi: 10.1051/0004-6361/201015441.

M. Jurić, Ž. Ivezić, A. Brooks, et al. The Milky Way Tomography with SDSS. I. Stellar Number Density Distribution. *ApJ*, 673:864–914, February 2008. doi: 10.1086/523619.

A. Just and H. Jahreiß. Towards a fully consistent Milky Way disc model - I. The local model based on kinematic and photometric data. *MNRAS*, 402:461–478, February 2010. doi: 10.1111/j.1365-2966.2009.15893.x.

A. Just and J. Rybizki. Dynamical and chemical evolution of the thin disc. *Astronomische Nachrichten*, 337:880, September 2016. doi: 10.1002/asna.201612390.

A. Just, S. Gao, and S. Vidrih. Towards a fully consistent Milky Way disc model - II. The local disc model and SDSS data of the NGP region. *MNRAS*, 411:2586–2595, March 2011. doi: 10.1111/j.1365-2966.2010.17866.x.

A. Just, K. Sysoliatina, and I. Koutsouridou. The evolution history of the extended solar neighbourhood. In A. Recio-Blanco, P. de Laverny, A. G. A. Brown, and T. Prusti, editors, *IAU Symposium*, volume 330 of *IAU Symposium*, pages 168–171, April 2018. doi: 10.1017/S1743921317006299.

P. R. Kafle, S. Sharma, G. F. Lewis, and J. Bland-Hawthorn. Kinematics of the Stellar Halo and the Mass Distribution of the Milky Way Using Blue Horizontal Branch Stars. *ApJ*, 761: 98, December 2012. doi: 10.1088/0004-637X/761/2/98.

A. I. Karakas. Updated stellar yields from asymptotic giant branch models. *MNRAS*, 403: 1413–1425, April 2010. doi: 10.1111/j.1365-2966.2009.16198.x.

D. Katz, P. Sartoretti, M. Cropper, et al. Gaia Data Release 2: Properties and validation of the radial velocities. *ArXiv e-prints:[1804.09372]*, April 2018.

G. Kordopatis, G. Gilmore, M. Steinmetz, et al. The Radial Velocity Experiment (RAVE): Fourth Data Release. *AJ*, 146:134, November 2013. doi: 10.1088/0004-6256/146/5/134.

G. Kordopatis, R. F. G. Wyse, C. Chiappini, et al. Cardinal kinematics - I. Rotation fields of the APOGEE survey. *MNRAS*, 467:469–489, May 2017. doi: 10.1093/mnras/stx096.

J. Kormendy and R. C. Kennicutt, Jr. Secular Evolution and the Formation of Pseudobulges in Disk Galaxies. *ARA&A*, 42:603–683, September 2004. doi: 10.1146/annurev.astro.42.053102.134024.

I. Koutsouridou. A Chemodynamical Model of the Milky Way Disk for Galactocentric Radii of 4 to 12 kpc. Master's thesis, The University of Heidelberg, Germany, 2017.

M. R. Krumholz. The big problems in star formation: The star formation rate, stellar clustering, and the initial mass function. *Phys. Rep.*, 539:49–134, June 2014. doi: 10.1016/j.physrep.2014.02.001.

M. Kubryk, N. Prantzos, and E. Athanassoula. Evolution of the Milky Way with radial motions of stars and gas. I. The solar neighbourhood and the thin and thick disks. *A&A*, 580:A126, August 2015. doi: 10.1051/0004-6361/201424171.

A. Kunder, G. Kordopatis, M. Steinmetz, et al. The Radial Velocity Experiment (RAVE): Fifth Data Release. *AJ*, 153:75, February 2017. doi: 10.3847/1538-3881/153/2/75.

T. L. Landecker. The Role of Magnetic Fields in the Interstellar Medium of the Milky Way. Evidence from the Diffuse Polarized Radio Emission. *Space Sci. Rev.*, 166:263–280, May 2012. doi: 10.1007/s11214-011-9796-6.

R. Launhardt, R. Zylka, and P. G. Mezger. The nuclear bulge of the Galaxy. III. Large-scale physical characteristics of stars and interstellar matter. *A&A*, 384:112–139, March 2002. doi: 10.1051/0004-6361:20020017.

Y. S. Lee, T. C. Beers, D. An, et al. Formation and Evolution of the Disk System of the Milky Way: [α/Fe] Ratios and Kinematics of the SEGUE G-dwarf Sample. *ApJ*, 738:187, September 2011. doi: 10.1088/0004-637X/738/2/187.

G. Lemaître. The Beginning of the World from the Point of View of Quantum Theory. *Nature*, 127:706, May 1931.

E. S. Levine, L. Blitz, and C. Heiles. The Spiral Structure of the Outer Milky Way in Hydrogen. *Science*, 312:1773–1777, June 2006a. doi: 10.1126/science.1128455.

E. S. Levine, L. Blitz, and C. Heiles. The Vertical Structure of the Outer Milky Way H I Disk. *ApJ*, 643:881–896, June 2006b. doi: 10.1086/503091.

S. J. Lilly, V. Le Brun, C. Maier, et al. The zCOSMOS 10k-Bright Spectroscopic Sample. *APJS*, 184:218–229, October 2009. doi: 10.1088/0067-0049/184/2/218.

L. Lindegren, U. Lammers, U. Bastian, et al. Gaia Data Release 1. Astrometry: one billion positions, two million proper motions and parallaxes. *A&A*, 595:A4, November 2016. doi: 10.1051/0004-6361/201628714.

L. Lindegren, J. Hernández, A. Bombrun, et al. Gaia Data Release 2. The astrometric solution. *A&A*, 616:A2, August 2018. doi: 10.1051/0004-6361/201832727.

X.-W. Liu, H.-B. Yuan, Z.-Y. Huo, et al. LSS-GAC - A LAMOST Spectroscopic Survey of the Galactic Anti-center. In S. Feltzing, G. Zhao, N. A. Walton, and P. Whitelock, editors, *Setting the scene for Gaia and LAMOST*, volume 298 of *IAU Symposium*, pages 310–321, January 2014. doi: 10.1017/S1743921313006510.

M. López-Corredoira. Milky Way rotation curve from proper motions of red clump giants. *A&A*, 563:A128, March 2014. doi: 10.1051/0004-6361/201423505.

M. López-Corredoira, C. Allende Prieto, F. Garzón, et al. Disk stars in the Milky Way detected beyond 25 kpc from its center. *A&A*, 612:L8, May 2018. doi: 10.1051/0004-6361/201832880.

A.-L. Luo, Y.-H. Zhao, G. Zhao, et al. The first data release (DR1) of the LAMOST regular survey. *Research in Astronomy and Astrophysics*, 15:1095, August 2015. doi: 10.1088/1674-4527/15/8/002.

J. T. Mackereth, J. Bovy, R. P. Schiavon, et al. The age-metallicity structure of the Milky Way disc using APOGEE. *MNRAS*, 471:3057–3078, November 2017. doi: 10.1093/mnras/stx1774.

P. Madau and M. Dickinson. Cosmic Star-Formation History. *ARA&A*, 52:415–486, August 2014. doi: 10.1146/annurev-astro-081811-125615.

A.-M. Madigan, O. Pfuhl, Y. Levin, et al. On the Origin of the B-stars in the Galactic Center. *ApJ*, 784:23, March 2014. doi: 10.1088/0004-637X/784/1/23.

D. Maoz, K. Sharon, and A. Gal-Yam. The Supernova Delay Time Distribution in Galaxy Clusters and Implications for Type-Ia Progenitors and Metal Enrichment. *ApJ*, 722:1879–1894, October 2010. doi: 10.1088/0004-637X/722/2/1879.

P. Marigo, L. Girardi, A. Bressan, et al. A New Generation of PARSEC-COLIBRI Stellar

Isochrones Including the TP-AGB Phase. *ApJ*, 835:77, January 2017. doi: 10.3847/1538-4357/835/1/77.

D. J. Marshall, A. C. Robin, C. Reylé, M. Schultheis, and S. Picaud. Modelling the Galactic interstellar extinction distribution in three dimensions. *A&A*, 453:635–651, July 2006. doi: 10.1051/0004-6361:20053842.

S. L. Martell, S. Sharma, S. Buder, et al. The GALAH survey: observational overview and Gaia DR1 companion. *MNRAS*, 465:3203–3219, March 2017. doi: 10.1093/mnras/stw2835.

S. Martín, J. Martín-Pintado, M. Montero-Castaño, P. T. P. Ho, and R. Blundell. Surviving the hole. I. Spatially resolved chemistry around Sagittarius A*. *A&A*, 539:A29, March 2012. doi: 10.1051/0004-6361/201117268.

Paul J. McMillan, Georges Kordopatis, Andrea Kunder, et al. Improved distances and ages for stars common to TGAS and RAVE. *MNRAS*, 477:5279–5300, July 2018. doi: 10.1093/mnras/sty990.

P. G. Mezger, W. J. Duschl, and R. Zylka. The Galactic Center: a laboratory for AGN? *A&A Rev.*, 7:289–388, 1996. doi: 10.1007/s001590050007.

D. Michalik, L. Lindegren, and D. Hobbs. The Tycho-Gaia astrometric solution . How to get 2.5 million parallaxes with less than one year of Gaia data. *A&A*, 574:A115, February 2015. doi: 10.1051/0004-6361/201425310.

I. Minchev, M. Martig, D. Streich, et al. On the Formation of Galactic Thick Disks. *ApJ*, 804: L9, May 2015. doi: 10.1088/2041-8205/804/1/L9.

I. Minchev, M. Steinmetz, C. Chiappini, et al. The Relationship between Mono-abundance and Mono-age Stellar Populations in the Milky Way Disk. *ApJ*, 834:27, January 2017. doi: 10.3847/1538-4357/834/1/27.

D. Minniti, P. W. Lucas, J. P. Emerson, et al. VISTA Variables in the Via Lactea (VVV): The public ESO near-IR variability survey of the Milky Way. *New A*, 15:433–443, July 2010. doi: 10.1016/j.newast.2009.12.002.

U. Munari, A. Henden, A. Frigo, et al. APASS Landolt-Sloan BVgri Photometry of RAVE Stars. I. Data, Effective Temperatures, and Reddenings. *AJ*, 148:81, November 2014. doi: 10.1088/0004-6256/148/5/81.

J. F. Navarro, C. S. Frenk, and S. D. M. White. Simulations of X-ray clusters. *MNRAS*, 275: 720–740, August 1995. doi: 10.1093/mnras/275.3.720.

M. Ness, K. Freeman, E. Athanassoula, et al. ARGOS - III. Stellar populations in the Galactic bulge of the Milky Way. *MNRAS*, 430:836–857, April 2013. doi: 10.1093/mnras/sts629.

J. A. Newman, M. C. Cooper, M. Davis, et al. The DEEP2 Galaxy Redshift Survey: Design, Observations, Data Reduction, and Redshifts. *APJS*, 208:5, September 2013. doi: 10.1088/0067-0049/208/1/5.

D. L. Nidever, J. Bovy, J. C. Bird, et al. Tracing Chemical Evolution over the Extent of the Milky Way's Disk with APOGEE Red Clump Stars. *ApJ*, 796:38, November 2014. doi: 10.1088/0004-637X/796/1/38.

K. Nomoto, C. Kobayashi, and N. Tominaga. Nucleosynthesis in Stars and the Chemical Enrichment of Galaxies. *ARA&A*, 51:457–509, August 2013. doi: 10.1146/annurev-astro-082812-140956.

B. Nordström, M. Mayor, J. Andersen, et al. The Geneva-Copenhagen survey of the Solar neighbourhood. Ages, metallicities, and kinematic properties of 14 000 F and G dwarfs. *A&A*, 418:989–1019, May 2004. doi: 10.1051/0004-6361:20035959.

P. A. Oesch, G. Brammer, P. G. van Dokkum, et al. A Remarkably Luminous Galaxy at z=11.1 Measured with Hubble Space Telescope Grism Spectroscopy. *ApJ*, 819:129, March 2016. doi: 10.3847/0004-637X/819/2/129.

S. S. R. Offner, P. C. Clark, P. Hennebelle, et al. The Origin and Universality of the Stellar Initial Mass Function. *Protostars and Planets VI*, pages 53–75, 2014. doi: 10.2458/azu_uapress_9780816531240-ch003.

T. Oka, M. Nagai, K. Kamegai, and K. Tanaka. A New Look at the Galactic Circumnuclear Disk. *ApJ*, 732:120, May 2011. doi: 10.1088/0004-637X/732/2/120.

T. Panamarev, A. Just, R. Spurzem, et al. Direct N-body simulation of the Galactic centre. *ArXiv e-prints:[1805.02153]*, May 2018.

D. Parkinson, S. Riemer-Sørensen, C. Blake, et al. The WiggleZ Dark Energy Survey: Final data release and cosmological results. *Phys. Rev. D*, 86(10):103518, November 2012. doi: 10.1103/PhysRevD.86.103518.

L. Pasquini, P. Bonifacio, S. Randich, D. Galli, and R. G. Gratton. Beryllium in turnoff stars of NGC 6397: Early Galaxy spallation, cosmochronology and cluster formation. *A&A*, 426: 651–657, November 2004. doi: 10.1051/0004-6361:20041254.

B. Paxton, L. Bildsten, A. Dotter, et al. Modules for Experiments in Stellar Astrophysics (MESA). *APJS*, 192:3, January 2011. doi: 10.1088/0067-0049/192/1/3.

B. Paxton, M. Cantiello, P. Arras, et al. Modules for Experiments in Stellar Astrophysics (MESA): Planets, Oscillations, Rotation, and Massive Stars. *APJS*, 208:4, September 2013. doi: 10.1088/0067-0049/208/1/4.

B. Paxton, P. Marchant, J. Schwab, et al. Modules for Experiments in Stellar Astrophysics (MESA): Binaries, Pulsations, and Explosions. *APJS*, 220:15, September 2015. doi: 10.1088/0067-0049/220/1/15.

P. J. E. Peebles. Origin of the Angular Momentum of Galaxies. *ApJ*, 155:393, February 1969. doi: 10.1086/149876.

A. A. Penzias and R. W. Wilson. A Measurement of Excess Antenna Temperature at 4080 Mc/s. *ApJ*, 142:419–421, July 1965. doi: 10.1086/148307.

B. Pila-Díez, J. T. A. de Jong, K. Kuijken, R. F. J. van der Burg, and H. Hoekstra. A skewer survey of the Galactic halo from deep CFHT and INT images. *A&A*, 579:A38, July 2015. doi: 10.1051/0004-6361/201425457.

Planck Collaboration, N. Aghanim, Y. Akrami, et al. Planck 2018 results. VI. Cosmological parameters. *ArXiv e-prints:[1807.06209]*, July 2018.

M. Portail, O. Gerhard, C. Wegg, and M. Ness. Dynamical modelling of the galactic bulge and bar: the Milky Way's pattern speed, stellar and dark matter mass distribution. *MNRAS*, 465: 1621–1644, February 2017. doi: 10.1093/mnras/stw2819.

A. C. Quillen and D. R. Garnett. The saturation of disk heating in the solar neighborhood and evidence for a merger 9 Gyrs ago. *ArXiv Astrophysics e-prints*, April 2000.

M. J. Reid. The distance to the center of the Galaxy. *ARA&A*, 31:345–372, 1993. doi: 10.1146/annurev.aa.31.090193.002021.

M. J. Reid and A. Brunthaler. The Proper Motion of Sgr A*. In J. Romney and M. Reid, editors, *Future Directions in High Resolution Astronomy*, volume 340 of *Astronomical Society of the Pacific Conference Series*, page 253, December 2005.

M. J. Reid, K. M. Menten, A. Brunthaler, et al. Trigonometric Parallaxes of High Mass Star Forming Regions: The Structure and Kinematics of the Milky Way. *ApJ*, 783:130, March 2014. doi: 10.1088/0004-637X/783/2/130.

C. Reylé, D. J. Marshall, A. C. Robin, and M. Schultheis. The Milky Way's external disc constrained by 2MASS star counts. *A&A*, 495:819–826, March 2009. doi: 10.1051/0004-6361/200811341.

R. M. Rich, D. B. Reitzel, C. D. Howard, and H. Zhao. The Bulge Radial Velocity Assay: Techniques and a Rotation Curve. *ApJ*, 658:L29–L32, March 2007. doi: 10.1086/513509.

W. W. Roberts. Large-Scale Shock Formation in Spiral Galaxies and its Implications on Star Formation. *ApJ*, 158:123, October 1969. doi: 10.1086/150177.

A. C. Robin, C. Reylé, S. Derrière, and S. Picaud. A synthetic view on structure and evolution of the Milky Way. *A&A*, 409:523–540, October 2003. doi: 10.1051/0004-6361:20031117.

A. C. Robin, C. Reylé, D. J. Marshall, and M. Schultheis. The Besançon Model of Stellar Population Synthesis of the Galaxy. *Astrophysics and Space Science Proceedings*, 26:171, 2012. doi: 10.1007/978-3-642-18418-5_18.

A. C. Robin, O. Bienaymé, J. G. Fernández-Trincado, and C. Reylé. Kinematics of the local disk from the RAVE survey and the Gaia first data release. *A&A*, 605:A1, August 2017. doi: 10.1051/0004-6361/201630217.

S. Röser, E. Schilbach, H. Schwan, et al. PPM-Extended (PPMX) - a catalogue of positions and proper motions. *A&A*, 488:401–408, September 2008. doi: 10.1051/0004-6361:200809775.

J. Rybizki. Inference from modelling the chemodynamical evolution of the Milky Way disc. *ArXiv e-prints:[1802.08432]*, February 2018.

J. Rybizki and A. Just. Towards a fully consistent Milky Way disc model - III. Constraining the initial mass function. *MNRAS*, 447:3880–3891, March 2015. doi: 10.1093/mnras/stu2734.

J. Rybizki, A. Just, and H.-W. Rix. Chempy: A flexible chemical evolution model for abundance fitting. Do the Sun's abundances alone constrain chemical evolution models? *A&A*, 605:A59, September 2017. doi: 10.1051/0004-6361/201730522.

L. V. Sales, A. Helmi, M. G. Abadi, et al. Orbital eccentricity as a probe of thick disc formation scenarios. *MNRAS*, 400:L61–L65, November 2009. doi: 10.1111/j.1745-3933.2009.00763.x.

R. H. Sanders. The circumnuclear material in the Galactic Centre - A clue to the accretion process. *MNRAS*, 294:35, February 1998. doi: 10.1046/j.1365-8711.1998.01127.x.

C. Scannapieco, S. D. M. White, V. Springel, and P. B. Tissera. The formation and survival of discs in a ΛCDM universe. *MNRAS*, 396:696–708, June 2009. doi: 10.1111/j.1365-2966.2009.14764.x.

J. Schaye, R. A. Crain, R. G. Bower, et al. The EAGLE project: simulating the evolution and assembly of galaxies and their environments. *MNRAS*, 446:521–554, January 2015. doi: 10.1093/mnras/stu2058.

D. J. Schlegel, D. P. Finkbeiner, and M. Davis. Maps of Dust Infrared Emission for Use in Estimation of Reddening and Cosmic Microwave Background Radiation Foregrounds. *ApJ*, 500:525–553, June 1998. doi: 10.1086/305772.

R. Schönrich and J. Binney. Chemical evolution with radial mixing. *MNRAS*, 396:203–222, June 2009a. doi: 10.1111/j.1365-2966.2009.14750.x.

R. Schönrich and J. Binney. Origin and structure of the Galactic disc(s). *MNRAS*, 399:1145–1156, November 2009b. doi: 10.1111/j.1365-2966.2009.15365.x.

R. Schönrich and W. Dehnen. Warp, waves, and wrinkles in the Milky Way. *MNRAS*, 478:3809–3824, August 2018. doi: 10.1093/mnras/sty1256.

R. Schönrich, J. Binney, and W. Dehnen. Local kinematics and the local standard of rest. *MNRAS*, 403:1829–1833, April 2010. doi: 10.1111/j.1365-2966.2010.16253.x.

I. R. Seitenzahl, F. Ciaraldi-Schoolmann, F. K. Röpke, et al. Three-dimensional delayed-detonation models with nucleosynthesis for Type Ia supernovae. *MNRAS*, 429:1156–1172, February 2013. doi: 10.1093/mnras/sts402.

S. Sharma, J. Bland-Hawthorn, K. V. Johnston, and J. Binney. Galaxia: A Code to Generate a Synthetic Survey of the Milky Way. Astrophysics Source Code Library, January 2011.

S. Sharma, J. Bland-Hawthorn, J. Binney, et al. Kinematic Modeling of the Milky Way Using the RAVE and GCS Stellar Surveys. *ApJ*, 793:51, September 2014. doi: 10.1088/0004-637X/793/1/51.

J. Shen, R. M. Rich, J. Kormendy, et al. Our Milky Way as a Pure-disk Galaxy – A Challenge for Galaxy Formation. *ApJ*, 720:L72–L76, September 2010. doi: 10.1088/2041-8205/720/1/L72.

D. Sijacki, M. Vogelsberger, S. Genel, et al. The Illustris simulation: the evolving population of black holes across cosmic time. *MNRAS*, 452:575–596, September 2015. doi: 10.1093/mnras/stv1340.

M. F. Skrutskie, R. M. Cutri, R. Stiening, et al. The Two Micron All Sky Survey (2MASS). *AJ*, 131:1163–1183, February 2006. doi: 10.1086/498708.

Y. Sofue, M. Honma, and T. Omodaka. Unified Rotation Curve of the Galaxy – Decomposition into de Vaucouleurs Bulge, Disk, Dark Halo, and the 9-kpc Rotation Dip –. *PASJ*, 61:227–236, February 2009. doi: 10.1093/pasj/61.2.227.

Y. Sofue, M. Honma, and T. Omodaka. Errata: Unified Rotation Curve of the Galaxy – Decomposition into de Vaucouleurs Bulge, Disk, Dark Halo, and the 9-kpc Rotation Dip. *PASJ*, 62:1367–1367, October 2010. doi: 10.1093/pasj/62.5.1367.

C. Soubiran, G. Jasniewicz, L. Chemin, et al. Gaia Data Release 2. The catalogue of radial velocity standard stars. *A&A*, 616:A7, August 2018. doi: 10.1051/0004-6361/201832795.

V. Springel. The cosmological simulation code GADGET-2. *MNRAS*, 364:1105–1134, December 2005. doi: 10.1111/j.1365-2966.2005.09655.x.

V. Springel. E pur si muove: Galilean-invariant cosmological hydrodynamical simulations on a moving mesh. *MNRAS*, 401:791–851, January 2010. doi: 10.1111/j.1365-2966.2009.15715.x.

V. Springel, N. Yoshida, and S. D. M. White. GADGET: a code for collisionless and gasdynamical cosmological simulations. *New A*, 6:79–117, April 2001. doi: 10.1016/S1384-1076(01)00042-2.

V. Springel, S. D. M. White, A. Jenkins, et al. Simulations of the formation, evolution and clustering of galaxies and quasars. *Nature*, 435:629–636, June 2005. doi: 10.1038/nature03597.

V. Springel, J. Wang, M. Vogelsberger, et al. The Aquarius Project: the subhaloes of galactic haloes. *MNRAS*, 391:1685–1711, December 2008. doi: 10.1111/j.1365-2966.2008.14066.x.

M. Steinmetz, T. Zwitter, A. Siebert, et al. The Radial Velocity Experiment (RAVE): First Data Release. *AJ*, 132:1645–1668, October 2006. doi: 10.1086/506564.

K. Sysoliatina, A. Just, O. Golubov, et al. The local rotation curve of the Milky Way based on SEGUE and RAVE data. *A&A*, 614:A63, June 2018a. doi: 10.1051/0004-6361/201731143.

K. Sysoliatina, A. Just, I. Koutsouridou, et al. Local disc model in view of Gaia DR1 and RAVE data. *ArXiv e-prints*, October 2018b.

V. Tsikoudi. Photometry and structure of lenticular galaxies. I - NGC 3115. *ApJ*, 234:842–853, December 1979. doi: 10.1086/157565.

Masato Tsuboi, Yoshimi Kitamura, Kenta Uehara, et al. ALMA view of the circumnuclear disk of the Galactic Center: tidally disrupted molecular clouds falling to the Galactic Center. *Publications of the Astronomical Society of Japan*, page 90, July 2018. doi: 10.1093/pasj/psy080.

A. Udalski, M. K. Szymański, and G. Szymański. OGLE-IV: Fourth Phase of the Optical Gravitational Lensing Experiment. *Acta Astron.*, 65:1–38, March 2015.

J. P. Vallée. Catalog of Observed Tangents to the Spiral Arms in the Milky Way Galaxy. *APJS*, 215:1, November 2014. doi: 10.1088/0067-0049/215/1/1.

J. P. Vallée. A guided map to the spiral arms in the galactic disk of the Milky Way. *The Astronomical Review*, 13:113–146, October 2017. doi: 10.1080/21672857.2017.1379459.

P. C. van der Kruit and L. Searle. Surface photometry of edge-on spiral galaxies. I - A model for the three-dimensional distribution of light in galactic disks. *A&A*, 95:105–115, February 1981.

F. van Leeuwen, editor. *Hipparcos, the New Reduction of the Raw Data*, volume 350 of *Astrophysics and Space Science Library*, 2007. doi: 10.1007/978-1-4020-6342-8.

F. van Leeuwen, D. W. Evans, F. De Angeli, et al. Gaia Data Release 1. The photometric data. *A&A*, 599:A32, March 2017. doi: 10.1051/0004-6361/201630064.

C. Vera-Ciro and A. Helmi. Constraints on the Shape of the Milky Way Dark Matter Halo from the Sagittarius Stream. *ApJ*, 773:L4, August 2013. doi: 10.1088/2041-8205/773/1/L4.

C. Vera-Ciro, E. D'Onghia, and J. F. Navarro. The Imprint of Radial Migration on the Vertical Structure of Galaxy Disks. *ApJ*, 833:42, December 2016. doi: 10.3847/1538-4357/833/1/42.

J.-L. Vergely, R. F. Ferrero, D. Egret, and J. Koeppen. The interstellar extinction in the solar neighbourhood. I. Statistical approach. *A&A*, 340:543–555, December 1998.

Á. Villalobos and A. Helmi. Simulations of minor mergers - II. The phase-space structure of thick discs. *MNRAS*, 399:166–176, October 2009. doi: 10.1111/j.1365-2966.2009.15085.x.

M. Vogelsberger, S. Genel, V. Springel, et al. Introducing the Illustris Project: simulating the coevolution of dark and visible matter in the Universe. *MNRAS*, 444:1518–1547, October 2014. doi: 10.1093/mnras/stu1536.

R. Wagner-Kaiser, D. Mackey, A. Sarajedini, et al. Exploring the nature and synchronicity of early cluster formation in the Large Magellanic Cloud - II. Relative ages and distances for six ancient globular clusters. *MNRAS*, 471:3347–3358, November 2017. doi: 10.1093/mnras/stx1702.

R. V. Wagoner, W. A. Fowler, and F. Hoyle. On the Synthesis of Elements at Very High Temperatures. *ApJ*, 148:3, April 1967. doi: 10.1086/149126.

L. Wang, R. Spurzem, S. Aarseth, et al. NBODY6++GPU: ready for the gravitational million-body problem. *MNRAS*, 450:4070–4080, July 2015. doi: 10.1093/mnras/stv817.

C. Wegg, O. Gerhard, and M. Portail. The structure of the Milky Way's bar outside the bulge. *MNRAS*, 450:4050–4069, July 2015. doi: 10.1093/mnras/stv745.

Charles A. Whitney. *The discovery of our Galaxy*. Iowa State University Press, 1988.

J. Wojno, G. Kordopatis, M. Steinmetz, et al. Chemical separation of disc components using RAVE. *MNRAS*, 461:4246–4255, October 2016. doi: 10.1093/mnras/stw1633.

J. Wojno, G. Kordopatis, T. Piffl, et al. The selection function of the RAVE survey. *MNRAS*, 468:3368–3380, July 2017. doi: 10.1093/mnras/stx606.

B. Yanny, C. Rockosi, H. J. Newberg, et al. SEGUE: A Spectroscopic Survey of 240,000 Stars with g = 14-20. *AJ*, 137:4377-4399, May 2009. doi: 10.1088/0004-6256/137/5/4377.

P. Yoachim and J. J. Dalcanton. Structural Parameters of Thin and Thick Disks in Edge-on Disk Galaxies. *AJ*, 131:226–249, January 2006. doi: 10.1086/497970.

J. Yu and C. Liu. The age-velocity dispersion relation of the Galactic discs from LAMOST-Gaia data. *MNRAS*, 475:1093–1103, March 2018. doi: 10.1093/mnras/stx3204.

N. Zacharias, C. Finch, and J. Frouard. UCAC5: New Proper Motions Using Gaia DR1. *AJ*, 153:166, April 2017. doi: 10.3847/1538-3881/aa6196.

T. Zwitter, G. Matijevič, M. A. Breddels, et al. Distance determination for RAVE stars using stellar models . II. Most likely values assuming a standard stellar evolution scenario. *A&A*, 522:A54, November 2010. doi: 10.1051/0004-6361/201014922.

Colophon

This thesis was typeset in LaTeX using the integrated LaTeX editing environment `Kile`. The graphics was prepared with the Python plotting library `Matplotlib` and with the `OpenOffice Impress` instrumentary. The bibliography was generated with `biblatex`.